



**FACULTY OF ELECTRICAL ENGINEERING  
UNIVERSITY OF BANJA LUKA**

# **ELECTRONICS**

# FACULTY OF ELECTRICAL ENGINEERING UNIVERSITY OF BANJA LUKA

Address: Patre 5, 78000 Banja Luka, Bosnia and Herzegovina

Phone: +387 51 211824

Fax: +387 51 211408

Web: [www.etfbl.net](http://www.etfbl.net)

## ELECTRONICS

Web: [www.electronics.etfbl.net](http://www.electronics.etfbl.net)

E-mail: [electronics@etfbl.net](mailto:electronics@etfbl.net)

### *Editor-in-Chief:*

Branko L. Dokić, Ph. D.

Faculty of Electrical Engineering, University of Banja Luka, Bosnia and Herzegovina

E-mail: [branko.dokic@etfbl.net](mailto:branko.dokic@etfbl.net)

### *Co Editor-In-Chief:*

Prof. Tatjana Pešić-Brdanin, University of Banja Luka, Bosnia and Herzegovina

E-mail: [tatjanapb@etfbl.net](mailto:tatjanapb@etfbl.net)

### *International Editorial Board:*

- Prof. Goce Arsov, St. Cyril and Methodius University, Macedonia
- Prof. Zdenka Babić, University of Banja Luka, Bosnia and Herzegovina
- Prof. Petar Biljanović, University of Zagreb, Croatia
- Prof. Milorad Božić, University of Banja Luka, Bosnia and Herzegovina
- Prof. Octavio Nieto-Taladriz Garcia, Polytechnic University of Madrid, Spain
- Dr Zoran Jakšić, IHTM, Serbia
- Prof. Vladimir Katić, University of Novi Sad, Serbia
- Prof. Tom J. Kazmierski, University of Southampton, United Kingdom
- Prof. Vančo Litovski, University of Niš, Serbia
- Dr Duško Lukač, University of Applied Sciences, Germany
- Prof. Danilo Mandić, Imperial College, London, United Kingdom
- Prof. Bratislav Milovanović, University of Niš, Serbia
- Prof. Vojin Oklobdžija, University of Texas at Austin, USA
- Prof. Predrag Pejović, University of Belgrade, Serbia
- Prof. Ninoslav Stojadinović, University of Niš, Serbia
- Prof. Robert Šobot, Western University, Canada
- Prof. Slobodan Vukosavić, University of Belgrade, Serbia
- Prof. Volker Zerbe, University of Applied Sciences of Erfurt, Germany

### *Secretary:*

Mladen Knežić, M.Sc.

Željko Ivanović, Ph.D.

Jovica Bulović

### *Publisher:*

Faculty of Electrical Engineering, University of Banja Luka, Bosnia and Herzegovina

Number of printed copies: 100

# Guest Editorial

**M**ICROELECTROMECHANICAL(MEMS) technologies represent a versatile set of tools for the fabrication of microelectronic devices and microsystems. They basically represent an extension of the conventional planar microelectronic technologies into the third dimension. Also known as non-planar, microsystem or microfabrication technologies, MEMS technologies use various techniques like surface and bulk micromachining to fabricate complex shapes integrating different functionalities into a single chip. With the development of nanotechnologies, the appearance of novel nanostructured materials and the overall refinement of the available fabrication tools and techniques, a new class of related devices emerged, NEMS – the nanoelectromechanical systems. Technologies used for MEMS and NEMS production are very similar, the main difference being in their accuracy and resolution. Together MEMS and NEMS brought to a wide variety of functionalities, including those not met in nature, and resulted in a plethora of novel applications and devices. A majority of these devices are either actuators of some kind or sensors.

With the advent of intelligent systems and their overall refinement and spreading to all facets of society, the need for different kinds of sophisticated sensors is constantly increasing. The most advanced state-of-the-art devices are those fabricated using MEMS and NEMS technologies. Their applications are very wide and include mechanical (e.g position, displacement, pressure, fluid flow, liquid level, acceleration, etc.), thermal, electromagnetic including optical (UV, visible and infrared detectors), magnetic, electrical, chemical and biological sensing. The performance obtained by such devices offers unprecedented sensitivities and selectivities. For instance, nanoantenna-based plasmonic sensors ensure sensitivities on the level of a single molecule.

The aim of this special issue is to show the wide variety of topics that represent different facets of the MEMS and NEMS sensing. They range from the underlying physical phenomena, across analytical and numerical considerations, device and

system design, experimental works related with fabrication and characterization, include novel solutions for practical applications and finally systems based on MEMS/NEMS devices and blocks.

The papers chosen for this issue cover quantum phenomena in complex nanostructures for MEMS and NEMS devices and handle fundamental adsorption-desorption phenomena in MEMS resonators for chemical and biological sensing. The issue of fluctuations is crucial in all sensing devices, since noise phenomena are those that define the ultimate device performance, thus a part of the material is dedicated to noise sources in MEMS sensors. Different building blocks for MEMS/NEMS are considered, including the mentioned resonator structures, but also elements for optical MEMS, the novel high refractive index contrast gratings with asymmetric unit cells.

The papers dedicated to concrete sensors cover different fields, including design, analytical and numerical modeling/simulation, experimental fabrication and characterization. Various devices are considered, including multipurpose thermopile-based MEMS sensors and high-precision interferometric systems for position measurement. A very interesting application included in this special issue combines both sensing and actuation into one application and is dedicated to a single degree of freedom motion stage for rheological sensing.

Finally industrial measurement systems based on MEMS devices are analyzed, the example being a multichannel acquisition system for industrial pressure transmitters based on piezoresistive MEMS chips.

If at least a part of the wide applicability and variety of MEMS and NEMS devices is conveyed to the readers, this editor will consider that the goals of this special issue are attained.

Zoran Jakšić  
Guest Editor

# Zoran Jakšić

## Biography

Zoran Jakšić is a full research professor and the science director at the University of Belgrade, Institute of Chemistry, Technology and Metallurgy, Center of Microelectronic Technologies. He received his Dipl.-Ing., Mag. Sci. and Ph.D. degrees in electrical engineering (engineering physics), all from the School of Electrical Engineering, University of Belgrade, Serbia.

His fields of interest include chemical and biological sensors based on electromagnetic optics of mesoscopic and subwavelength structures (nanooptics and nanophotonics), plasmonics and metamaterials, photonic crystals, micro and nanoelectromechanical systems (MEMS and NEMS), infrared semiconductor detectors and narrow-gap semiconductors. He opened several new research fields, including metamaterial-based chemical sensors, optical noise in refractometric sensors, inorganic biomimetic nanomembranes and plasmonic enhancement of infrared photodetectors. He is the founder of the first Serbian group for plasmonics and metamaterials.

At the University of Belgrade, School of Electrical Engineering he introduced courses "Microelectromechanical Systems (MEMS)", "Elements of Nanooptics and Nanophotonics" and "Photonic Crystals and Optical Metamaterials". He chaired a number of national and international conferences and edited numerous conference proceedings. In 2005 he established a series of annual workshops on nanosciences and nanotechnologies

nanoETRAN. He is the program chair of the ETRAN Society, the oldest and the most prestigious Serbian expert society, and the president elect of the Optical Society of Serbia.

He authored 314 peer-reviewed publications, including an international monograph (Z. Jakšić, "Micro and Nanophotonics for Semiconductor Infrared Detectors," Springer, 2014, ISBN 978-3-319-09673-5), a monograph study (Z. Jakšić, "Optical metamaterials as the platform for a novel generation of ultrasensitive chemical or biological sensors," Nova Science, 2010, ISBN 978-1-61668-958-2), 76 international journal papers and five book chapters. He has been a reviewer for Nature, Elsevier Books, Optics Express, Optics Communications, Optics Letters, Journal of Optics A, Journal of Physics C, Journal of Nanophotonics, IEEE Sensors, Journal of Physics D, Semiconductor Science and Technology, New Journal of Physics, Infrared Physics & Technology, Physica Scripta, etc. He is a member of editorial boards of journals Electronics, Biomimetics and Facta Universitatis – Series EE.

Zoran Jakšić is a Senior Member of the IEEE (The Institute of Electrical and Electronics Engineers), a member of the OSA (Optical Society of America), a founding member of the OSS (Optical Society of Serbia), a Committee member of the National Society for Microwave Technique and Technologies of Serbia and a honorary member of the ETRAN Society.

# Nonparabolic effects in multiple quantum well structures and influence of external magnetic field on dipole matrix elements

Aleksandar Demić, Jelena Radovanović and Vitomir Milanović

**Abstract**—We present a method of modeling of nonparabolic effects (NPE) in quantum nanostructures by using second order perturbation theory. We apply this model on multiple quantum well structures and consider the influence of external magnetic field on dipole matrix element which is usually considered constant. The dipole matrix element directly influences the optical gain, and our model can provide a better insight to how NPE and magnetic field influence the gain of quantum nanostructures.

**Index Terms**—Nonparabolicity effects; Quantum cascade lasers; Perturbation theory.

Original Research Paper  
DOI: 10.7251/ELSI519039D

## I. INTRODUCTION

NONPARABOLIC effects (NPE) in the conduction band (CB) of a semiconductor quantum well (QW) material take an essential role in modeling the electronic structure of multiple QW structures such as quantum cascade laser (QCL). By using 14-band **kp** calculation presented in [1] Ekenberg in [2] determined the coefficients in the expansion of the dispersion relation up to the fourth order in wavevector. This results in a fourth order differential equation with boundary conditions obtained by double integration which fulfills the requirement for probability current conservation [3]. In [4] the authors presented the model from [2, 3] and its application on QCL structures by using the transfer matrix method (TMM).

QCL structures are powerful light sources emitting from mid-infrared (MIR) to THz frequencies, that turned out to be efficient and reliable in free-space communications, medical diagnostics, and chemical sensing [5-9].

Manuscript received 08 November 2015. Received in revised form 15 December 2015.

This work was supported by the Ministry of Education, Science and Technological development (Republic of Serbia), (Project III45010) and SFP Grant, ref. no. 984068.

Aleksandar Demić is with the School of Electrical Engineering, University of Belgrade, 73 Bulevar kralja Aleksandra, 11020 Belgrade, Serbia (e-mail: alexandardemic@yahoo.com).

Jelena Radovanović is with the School of Electrical Engineering, University of Belgrade, 73 Bulevar kralja Aleksandra, 11020 Belgrade, Serbia (e-mail: radovanovic@etf.bg.ac.rs).

Vitomir Milanović is with the School of Electrical Engineering, University of Belgrade, 73 Bulevar kralja Aleksandra, 11020 Belgrade, Serbia (e-mail: milanovic@etf.bg.ac.rs).

By engineering the active region, it is possible to obtain a wide range of operating wavelengths from 3  $\mu\text{m}$  up to 250  $\mu\text{m}$ . The lasing wavelength is defined by the separation of the laser energy state, and for THz frequencies the energy difference is very small (around 10meV) and thus any shift in energy can make modeling of these structures more demanding.

We will use the model from [2-4] and apply a second order perturbation theory in order to model energy corrections more accurately. We will also consider a first order correction for the wavefunction and this will allow us to study the effect of magnetic field on dipole matrix element, or in another sense the dependence of the gain of QCL. Nonparabolic effects are more pronounced in materials with smaller energy gaps due to a stronger mixing of the bands, thus we will also apply our model on structures with such properties.

## II. THEORETICAL CONSIDERATION

The Hamiltonian presented in [2] in presence of magnetic field can be written as  $\hat{H} = \hat{H}_{NP0} + \hat{H}_{NP}$ , where  $\hat{H}_{NP0}$  represents the part of the Hamiltonian  $\hat{H}_{NP0} = \hat{H}(\hat{k}_{||} = 0)$  and it can be represented as the sum of the unperturbed Hamiltonian  $\hat{H}_0 = \hat{k}_z^2 \alpha_0(z) \hat{k}_z^2 + \frac{\hbar^2}{2} \hat{k}_z \frac{1}{m^*(z)} \hat{k}_z + V(z)$  and the perturbed Hamiltonian  $\hat{H}' = \left(j_n + \frac{1}{2}\right) \frac{eB\hbar}{M(z)}$ .  $\hat{H}_{NP}$  can be treated with the second order perturbation theory (first correction vanishes) and this was done in [2].  $\hat{H}_{NP}$  has the form  $(2\alpha_0(z) + \beta_0 z^2 + \gamma_0 z^4) \hat{k}_x \hat{k}_y + \alpha_0 z^2 \hat{k}_x^2 + \gamma_0 z^4 \hat{k}_y^2$ . The coefficients  $\alpha_0$ ,  $\beta_0$  are nonparabolic parameters,  $B$  is the magnetic induction of external magnetic field,  $V(z)$  is the potential of the structure,  $\hat{k}_x, \hat{k}_y, \hat{k}_z$  are the wavevector components operators,  $m^*(z)$  is the effective mass at the bottom of conduction band and  $j_n$  is the Landau level index.

In this paper we focus on  $\hat{H}_{NP0}$ , and apply the second order perturbation theory. The Hamiltonian  $\hat{H}$  operates on the envelope wavefunction  $\eta_n(z)$ . We treat  $\hat{H}_{NP0}$  and  $\hat{H}_{NP}$  separately. For  $\hat{H}_{NP0}$  we first solve the eigenvalue problem with non perturbed Hamiltonian  $\hat{H}_0 \eta_{n0}(z) = E_n^{(0)} \eta_{n0}(z)$  (index 0 depicts zeroth correction (unperturbed value), and indices  $n=1,2, \dots$  depict the bound state energy index) and use wavefunctions  $\eta_{n0}(z)$  as the basis for perturbation theory with the perturbed Hamiltonian  $\hat{H}'$ .  $\hat{H}_{NP}$  is treated with second

order perturbation theory in [2], first correction for energy  $\Delta E_n^{(1)}$  is also determined in [2]. Corrections for energy are:

$$\begin{aligned}\Delta E_n^{(1)} &= \left(j_n + \frac{1}{2}\right) \frac{eB\hbar}{m^*_{\parallel}} \\ \Delta E_n^{(2)} &= \left[\left(j_n + \frac{1}{2}\right) eB\hbar\right]^2 \sum_{k \neq n} \frac{|M_{nk}|^2}{E_n^{(0)} - E_k^{(0)}} \\ \Delta E_{NP}^{(2)} &= [(8j_n^2 + 8j_n + 5) \langle \alpha_0 \rangle + \\ &\quad (j_n^2 + j_n + 1) \langle \beta_0 \rangle] \frac{e^2 B^2}{2\hbar^2}\end{aligned}\quad (1)$$

where  $\frac{1}{m^*_{\parallel}} = \int_{-\infty}^{\infty} \eta_{n0}^* \frac{1}{\bar{M}(z)} \eta_{n0} dz$  is parallel mass,  $M_{nk} = \int_{-\infty}^{\infty} \eta_{n0}^* \frac{1}{\bar{M}(z)} \eta_{k0} dz$ ,  $n \neq k$  are matrix elements of perturbed Hamiltonian and  $\langle \alpha_0 \rangle$  and  $\langle \beta_0 \rangle$  are the expected values of nonparabolic parameters.

The first order correction for envelope wavefunction is

$$\Delta \eta_n^{(1)} = e\hbar B \left(j_n + \frac{1}{2}\right) \sum_{k \neq n} \frac{M_{nk}}{E_n^{(0)} - E_k^{(0)}} \eta_{k0}, \quad n \neq k. \quad (2)$$

Overall energy and envelope wavefunctions are given with  $E = E_n^{(0)} + \Delta E_n^{(1)} + \Delta E_n^{(2)} + \Delta E_{NP}^{(2)}$  and  $\eta_n = \eta_{n0} + \eta_n^{(1)}$ .

The presence of external electric field introduces a linear  $z$  term in the potential  $V(z)$  of unperturbed Hamiltonian which results in continuous energy spectrum. In the case of moderate external electric fields, the energy states that were previously bound evolve into the so-called quasi-bound states after the application of bias, and they can then still be treated as bound under the additional assumption that the potential is constant far enough from the well [10]. These quasi-bound states can be determined by numerical solving of the  $\hat{H}_0$  eigen value problem and then energy and wavefunction corrections can be calculated.

The application of the perturbation theory is limited by the condition  $|H'_{nk}| \ll E_n^{(0)} - E_k^{(0)}$ . The perturbed Hamiltonian depends on magnetic induction and Landau level index and this condition imposes constraints on the values of these parameters. The second condition which limits our model emerges from the dispersion relation in bulk material, as presented in [4]. By solving the quantum well structure we can easily determine dispersion relation in the form  $E(k) = \alpha_0 k^4 + \frac{\hbar^2}{2m^*} k^2$  which has a maximum value of  $E_{max} = (16m^{*2}/\hbar^4 |\alpha_0|)^{-1} \approx 3.63 |\alpha_0|^{-1} m'^{-2}$  [eV] where  $m^* = m' m_0$  and  $\alpha_0$  is inserted in [eVÅ<sup>4</sup>]. The authors in [4] noted that the model is applicable up to the turning point of the dispersion relation, but we claim its applicability up to  $E_{max}$ . The conditions for the application of our model are:

$$\begin{aligned}B \left(j + \frac{1}{2}\right) &\ll P_t, & P_t &= \min \left( \frac{|E_n^{(0)} - E_k^{(0)}|}{e\hbar |M_{nk}|} \right), \\ & & n &\neq k \\ E < E_{max}, & & E_{max} &\approx \frac{3.63}{|\alpha_0| m'^2} \text{ [eV]}.\end{aligned}\quad (3)$$

We will consider the first condition in (3) satisfied for  $B \left(j + \frac{1}{2}\right) \leq 0.1 P_t$ . The parameter  $P_t$  mostly depends on the energy separations and we expect that it will cause rigorous constraint for magnetic fields in terahertz QCL structures. The second condition benefits from low effective masses in III-V semiconductors, but deteriorates for large values of the nonparabolic parameter  $\alpha_0$ . In most cases of interest  $E_{max}$  will be lower than the conduction band offset and it will not be possible to consider all states in the structure. Our greatest interest is usually in the lower states of considered QW or QCL, hence if  $E_{max}$  is greater than all the states of interest, we will continue with the application of the model. This approximation is possible due to the fact that in perturbation theory higher states have lesser effect on the lower states when calculating corrections in (1) and (2).

Equations (1)-(3) represent a complete model of the second order perturbation theory of NPE in semiconductor nanostructures.

Since we included first order correction for wavefunction we can discuss its effect on the dipole transition element. The dipole transition matrix element is defined as  $d_{if} = \int_{-\infty}^{\infty} \eta_i^* z \eta_f dz$  where index  $i$  refers to an initial state, and  $f$  to a final state of the optical transition. The envelope wavefunctions  $\eta_i$ ,  $\eta_f$  are usually chosen as unperturbed wavefunctions, but by including correction we will be able to analyze the influence of magnetic field on the properties of our structure. Inserting (2) in  $d_{if}$  yields:

$$\begin{aligned}d_{if} &= d_{if}(0) \\ &+ B \left(j + \frac{1}{2}\right) \left[ \int_{-\infty}^{\infty} (\eta_i^{(1)*} z \eta_{f0} + \eta_{i0}^* z \eta_f^{(1)}) dz \right] \\ &+ B^2 \left(j + \frac{1}{2}\right)^2 \int_{-\infty}^{\infty} \eta_i^{(1)*} z \eta_f^{(1)} dz\end{aligned}\quad (4)$$

where  $d_{if}(0) = \int_{-\infty}^{\infty} \eta_{i0}^* z \eta_{f0} dz$ . The third term in (4) is very small and we can assume that the behavior of  $d_{if}$  is linear with magnetic field in most cases. Note that first order corrections for the envelope wavefunctions are linearly proportional to the non-parabolic parameters  $\alpha_0$  and  $\beta_0$  (because of the matrix elements of perturbed Hamiltonian  $M_{nk}$  in eq. (1)), hence we expect greater rates of change in materials with great nonparabolicity but on the other hand the conditions in (3) will also become more rigorous. Modeling of these parameters and their determination in III-V semiconductor and alloys of interest are given in [11].

The importance of the dipole matrix element lies in the fact that gain and absorption values of optical transitions depend on  $|d_{if}|^2$ . Let us consider a 3-states QCL structure  $E_1 < E_2 <$

$E_3$  with two transitions of interest:  $E_3 \rightarrow E_2$  (lasing transition) and  $E_2 \rightarrow E_1$  (transition for depopulation of the second state). Most models of QCL structures calculate the dipole matrix element in (4) with unperturbed wavefunctions (only first term in (4)), thus the effect of external magnetic field cannot be seen. In this paper we will illustrate the dependence of the dipole matrix element on  $B$  for different Landau levels by using wavefunctions with first order correction.. Also (3) gives us the values of magnetic field  $B_j$  which limit the application of the perturbation theory. As mentioned in [12], in the presence of external magnetic field the optical gain which corresponds to transitions  $(3,j) \rightarrow (2,j)$  depends on  $E_{3,j} - E_{2,j}$ . The authors in [12] included first order corrections for the energy, the model presented in this paper includes higher correction. The optical gain of this transition now has the form:

$$g_{3 \rightarrow 2}(B) = \frac{2e^2\pi}{\bar{n}\epsilon_0\lambda} \sum_j |d_{3,2,j}(B)|^2 \times \delta(E_{3,j}(B) - E_{2,j}(B) - \hbar\omega) (N_{3,j}(B) - N_{2,j}(B))$$

$$E_{3,j} - E_{2,j} = E_3^{(0)} - E_2^{(0)} + e\hbar B \left( j + \frac{1}{2} \right) \left( \frac{1}{m_{||3}} - \frac{1}{m_{||2}} \right) + \left( \left( j + \frac{1}{2} \right) e\hbar B \right)^2 \times$$

$$\left( \sum_{k \neq 3} \frac{|M_{3k}|^2}{E_3^{(0)} - E_k^{(0)}} - \sum_{k \neq 2} \frac{|M_{2k}|^2}{E_2^{(0)} - E_k^{(0)}} \right) + [(8j^2 + 8j + 5)\Delta\langle \alpha_0 \rangle + (j^2 + j + 1)\Delta\langle \beta_0 \rangle] \frac{e^2 B^2}{2\hbar^2}$$

where  $\bar{n}$  is the material refractive index,  $\lambda$  and  $\omega$  denote the wavelength and the frequency of the emitted light,  $N_{3,j} - N_{2,j}$  represents the degree of population inversion, while  $\Delta\langle \alpha_0 \rangle$  and  $\Delta\langle \beta_0 \rangle$  represent differences of expectation values when wavefunctions of third and second states are used. The greatest addition to the gain in (5) arrives from the states with lower values of Landau level index. In numerical approach Dirac delta function can be substituted with suitable Lorentzian as explained in [12].

### III. NUMERICAL RESULTS

Applying our model to structures in presence of electric field demands numerical solving of equations (1)-(4). We assume that moderate electric field is applied and that we can approximate the potential at the structure ends to be constant [10]. We use TMM method to determine energies and wavefunctions of Hamiltonian  $\hat{H}_0$ . These quasi-bound states are then used in perturbation theory.

We will apply our model on three QCL structures which will illustrate behavior of dipole matrix elements. Firstly we focus on the structure presented in [12] which is optimized for  $\lambda = 10 \mu\text{m}$  and has the following layer widths 25, **30**, 59, **12**, 59 Å (bold are  $\text{Al}_{0.4}\text{Ga}_{0.6}\text{As}$  barriers and in normal text are

GaAs wells) with a barrier height of 330 meV. The applied electric field is  $K = 35.81 \text{ kVcm}^{-1}$ . The potential of the structure and the corresponding envelope wavefunctions are presented in Fig. 1.

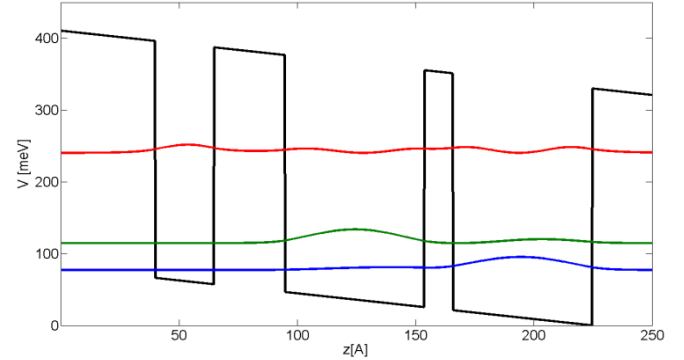


Fig. 1. The active region of QCL [12] under an electric field of  $K = 35.81 \text{ kVcm}^{-1}$  and magnetic field of induction  $B = 0 \text{ T}$ . Relevant energies and the moduli squared of non-perturbed wavefunctions are also displayed.

Energy levels in Fig. 1 are  $E_j = 77.1 \text{ meV}$ ,  $E_2 = 114.5 \text{ meV}$  and  $E_3 = 240.3 \text{ meV}$  which corresponds to a lasing wavelength of  $\lambda \approx 9.85 \mu\text{m}$ , which is in good correspondence with [12]. Under the influence of an external magnetic field we can calculate corrections for energy and wavelength by using our model. The conditions in (3) give  $E_{max} = 384 \text{ meV}$  for GaAs and limiting magnetic fields are  $B_0 = 234.7 \text{ T}$ ,  $B_1 = 78.2 \text{ T}$ ,  $B_2 = 46.9 \text{ T}$ ,  $B_3 = 33.5 \text{ T}$ ,  $B_4 = 23 \text{ T}$ ,  $B_5 = 21.3 \text{ T}$ , due to physical relevance we are interested in results below 60 T. In (5), optical gain depends on  $E_{3,j} - E_{2,j}$  and  $|d_{3,2,j}(B)|^2$ , authors in [12] considered first order corrections for energy, difference  $E_{3,j} - E_{2,j}$  with second order corrections is presented in Fig. 2 and  $|d_{3,2,j}(B)|^2$  is presented in Fig 3.

Figure 2 shows how lasing energy difference depends on magnetic field. We can see that for constant magnetic field this difference decreases when higher Landau levels are considered. The lasing wavelength is defined by  $E_{3,0} - E_{2,0}$  and in Fig 2. we can see that this value slightly varies with magnetic field which opens possibilities of tuning.

Figure 3 shows how square moduli of the dipole matrix element depends on magnetic field for lasing transition. For higher Landau levels we have more a pronounced decrease of  $|d_{3,2}|^2$  than for lower ones. Lower Landau levels give the greatest contribution to the gain in (5), the authors in [12] estimated that the highest gain is achievable around 45-50 T without taking into account variation of  $|d_{3,2}|^2$  with magnetic field. The results in Fig. 3 show that optical gain would be lower approximately 1-5 % (assuming that  $j = 0,1$  are the dominant terms in (5) and that second order corrections for the energy in  $E_{3,j} - E_{2,j}$  do not contribute significantly).

We can also calculate  $|d_{2,1}|^2$  which is responsible for depopulation of the second state. Note that for  $|d_{2,1}|^2$  Landau levels of both states can be arbitrary, thus we will separately present radiative transitions  $j_1 = j_2 = j$  (Figure 4) and non-radiative transitions  $j_1 \neq j_2$  (Figure 5).

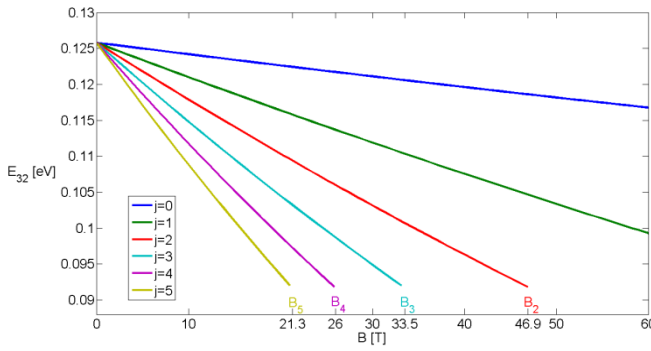


Fig. 2. Lasing energy difference for structure from [12] depending on magnetic induction for different Landau levels.

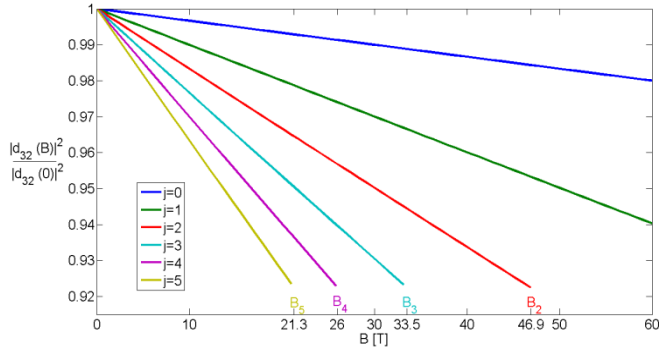


Fig. 3. Dipole matrix element  $|d_{32}|^2$  for structure from [12] depending on magnetic induction for different Landau levels and  $|d_{32}(0)| = 21.2 \text{ \AA}$ .

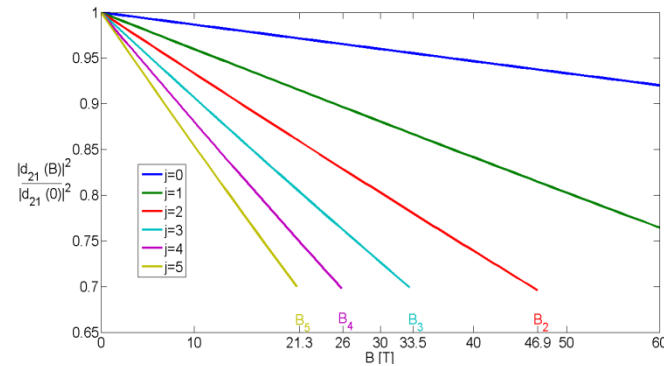


Fig. 4. Dipole matrix element  $|d_{21}|^2$  for structure from [12] depending on magnetic induction for different Landau levels (and  $j_1 = j_2 = j$ ) and  $|d_{21}(0)| = 27.4 \text{ \AA}$ .

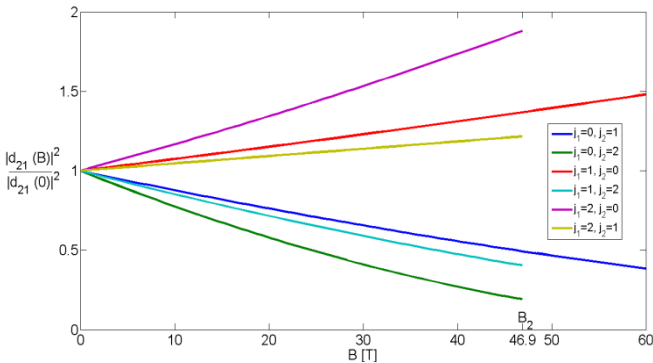


Fig. 5. Dipole matrix element  $|d_{21}|^2$  for structure from [12] depending on magnetic induction for different Landau levels (and  $j_1 \neq j_2$ ).

Figure 4 shows how square moduli of dipole matrix element depends on magnetic field for optical transition  $2 \rightarrow 1$  when both states have same value of Landau level. The effect

is more pronounced than the transition  $3 \rightarrow 2$  (fig. 3) and we have an extensive decrease of dipole matrix element.

Figure 5 shows  $|d_{21}|^2$  when Landau levels for particular states do not match. We can see that for  $j_1 < j_2$  we have a decrease of the dipole matrix element while for  $j_1 > j_2$  this does not occur. The effect is even more extensive than in previous transitions and for certain values of magnetic field and Landau level indices we nearly have a minimal value.

In this example we see that the dipole matrix element mostly decrease with magnetic field, and that the decrease is stronger for higher Landau levels.

Next we consider the structure realized in [13] for emission at  $\lambda \approx 68 \mu\text{m}$  (and designed for  $66 \mu\text{m}$ ). The active region layer widths are 82, **17**, 68, **40**, 164, **34**, 90  $\text{\AA}$  (GaAs wells are in normal text,  $\text{Al}_{0.15}\text{Ga}_{0.85}\text{As}$  are in bold text) with a barrier height of  $125.5 \text{ meV}$ . Applied electric field is  $10.2 \text{ kV cm}^{-1}$ . The potential of the structure and the unperturbed wavefunctions are shown in Fig 6.

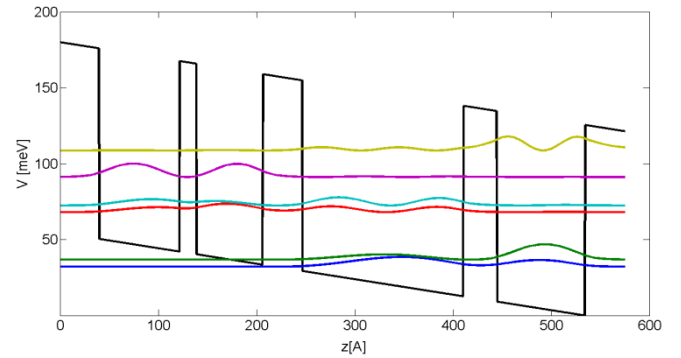


Fig. 6. The active region of QCL [13] under an electric field of  $K = 10.2 \text{ kV cm}^{-1}$  and magnetic field induction  $B = 0 \text{ T}$ . Relevant energies and the moduli squared of non-perturbed wavefunctions are also displayed.

The states of interest in Fig. 6 are  $E_2=36.73 \text{ meV}$ ,  $E_3=67.97 \text{ meV}$ ,  $E_4=72.38 \text{ meV}$  and  $E_5=91.11 \text{ meV}$ . Lasing transition occurs between  $5 \rightarrow 4$  or  $5 \rightarrow 3$ , which corresponds to a difference of  $E_{5,4}=18.73 \text{ meV}$  and a lasing wavelength of  $\lambda_{5,4} \approx 66.2 \mu\text{m}$ , which is in good correspondence with the results from [13]. The maximum energy from condition (3) is  $384 \text{ meV}$  and this condition does not add limits to our model, but the perturbation theory condition does. Limiting magnetic fields are  $B_0=2.1 \text{ T}$ ,  $B_1=2.5 \text{ T}$ ,  $B_2=3.3 \text{ T}$ ,  $B_3=4.6 \text{ T}$ ,  $B_4=7.7 \text{ T}$ ,  $B_5=23.2 \text{ T}$ . With unperturbed wavefunctions from Fig. 6 we can calculate energy and wavefunction corrections, lasing difference  $E_{5,4}$  is given in Fig. 7, while results for dipole matrix element for lasing transition is given in Fig. 8.

In Fig. 7 we can see that the energy difference of transition  $5 \rightarrow 4$  varies linearly with magnetic field which means that second order corrections are very small. In Figure 8 we can see a mild change of dipole matrix element with magnetic field. It is interesting that in this example we have an increasing effect. Our simulations show that the dipole matrix element for optical transition  $3 \rightarrow 2$  used for resonant depletion also increases with magnetic field for both radiative and non-radiative transitions more extensively (up to 15%). This example illustrates that the dipole matrix element can also rise with magnetic field.

The considered material of QW in the previous two examples was GaAs which has low nonparabolicity parameters due to a large energy gap. Both examples showed mild changes of the dipole matrix element for lasing transition. The model in [11] shows that low gap materials would give much higher nonparabolicity. On the other hand, the maximum energy condition in (3) becomes more rigorous and we are unable to model QCL structures made from InAs which would give nearly 30 times higher nonparabolicity parameters than GaAs. Fortunately we are able to model structures designed for terahertz applications because in most cases the energy states of interest are sufficiently below the maximum energy and we can consider low gap materials such as GaSb which has roughly 4 times higher parameters than GaAs. Structures for terahertz range have narrow energy separations and modeling NPE is highly important. At the same time, the narrow energy separation will also cause perturbation theory condition in (3) to be much more rigorous.

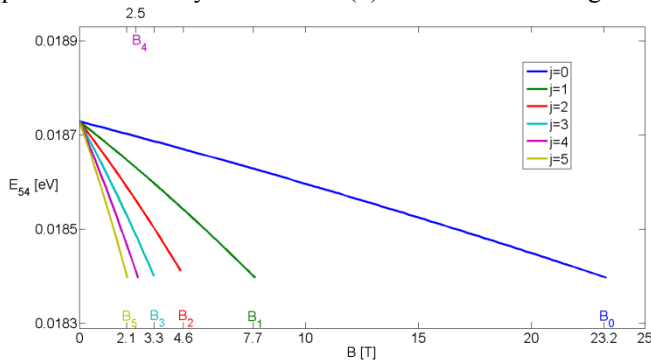


Fig. 7. Lasing energy difference for structure from [13] depending on magnetic induction for different Landau levels.

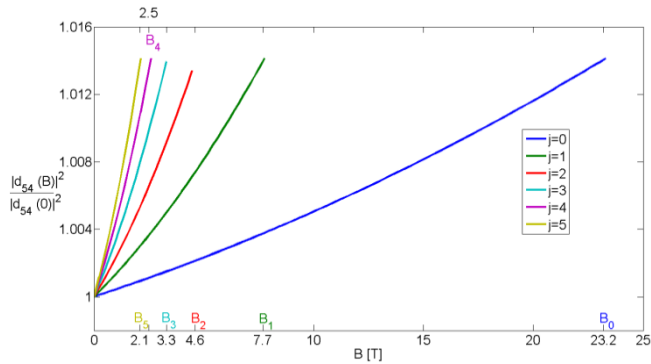


Fig. 8. Dipole matrix element squared,  $|d_{54}|^2$  for the structure from [13] as a function of magnetic induction for different Landau levels and  $|d_{54}(0)| = 56.6 \text{ \AA}$ .

We will consider a terahertz QCL proposed and experimentally realized in [14] for lasing at  $\lambda \approx 115.3 \mu\text{m}$  (2.6 THz) and  $\lambda \approx 157.9 \mu\text{m}$  (1.9 THz) which corresponds to transitions  $E_{53}=10.6 \text{ meV}$  and  $E_{54}=7.7 \text{ meV}$ , respectively, with a phonon longitudinal energy of  $E_{32}=28.9 \text{ meV}$ . This is a 4-well structure with the layer widths of active region 144, **24**, 114, **38**, 246, **30**, 162  $\text{\AA}$  (bold AISb barriers and non-bold are GaSb wells) with barrier height of 1090 meV. Applied electric field is  $5.4 \text{ kV cm}^{-1}$ . The maximum energy from condition (3) is  $E_{max} \approx 201 \text{ meV}$ , nonparabolicity parameters in GaSb are  $\alpha_0 = -10730 \text{ eV \AA}^4$ ,

$\beta_0 = -11473 \text{ eV \AA}^4$  and in the AISb are  $\alpha_0 = -330 \text{ eV \AA}^4$ ,  $\beta_0 = -2342 \text{ eV \AA}^4$ . The solutions of unperturbed Hamiltonian are shown in Fig. 9.

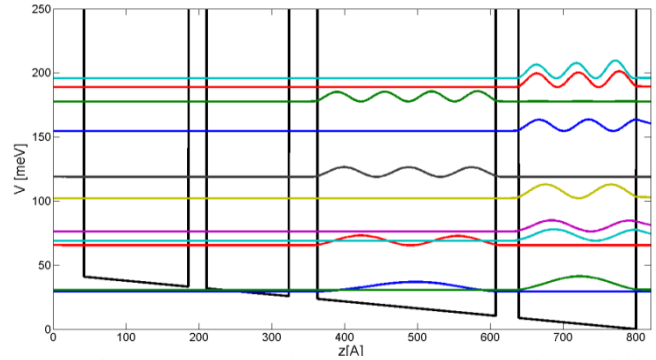


Fig. 9. The active region of QCL [14] under an electric field of  $K = 5.4 \text{ kV cm}^{-1}$  and magnetic field of induction  $B = 0 \text{ T}$ . Relevant energies and the moduli squared of non-perturbed wavefunctions are also displayed. Barrier height is 1090 meV, the picture is zoomed for better view.

The barrier height is 1090 meV and condition in (3) gives maximum energy of 201 meV, but energies of interest are below 80 meV and our model is applicable under the assumption that higher states do not contribute greatly to perturbation theory corrections. In Fig. 9 we can see that 11 states can be modeled. The states of interest are  $E_1=29.36 \text{ meV}$ ,  $E_2=30.5 \text{ meV}$ ,  $E_3=65.46 \text{ meV}$ ,  $E_4=68.96 \text{ meV}$  and  $E_5=76.22 \text{ meV}$ . Lasing transition occurs between  $5 \rightarrow 4$  or  $5 \rightarrow 3$ , which correspond to differences of  $E_{54}=7.24 \text{ meV}$  and  $E_{53}=10.76 \text{ meV}$  and wavelengths  $\lambda_{54} \approx 170.5 \mu\text{m}$  (1.7 THz),  $\lambda_{53} \approx 115.2 \mu\text{m}$  (2.6 THz) respectively, which is in good correspondence with the results from [14].

Conditions (3) yield  $B_0=0.75 \text{ T}$ ,  $B_1=0.25 \text{ T}$ ,  $B_2=0.15 \text{ T}$ ,  $B_3=0.1 \text{ T}$ ,  $B_4=0.08 \text{ T}$ ,  $B_5=0.07 \text{ T}$ , above these values theory of perturbation is not applicable (for the corresponding Landau level). The reason for this is a narrow energy separation and also the fact that  $P_t$  depends on  $M_{nk}$  (in eq. (1)), which depends on magnetic field and nonparabolic parameters. The energy difference  $E_{54}$  is given in Fig. 10, while the results for the dipole matrix element for transition  $5 \rightarrow 4$  are given in Fig. 11

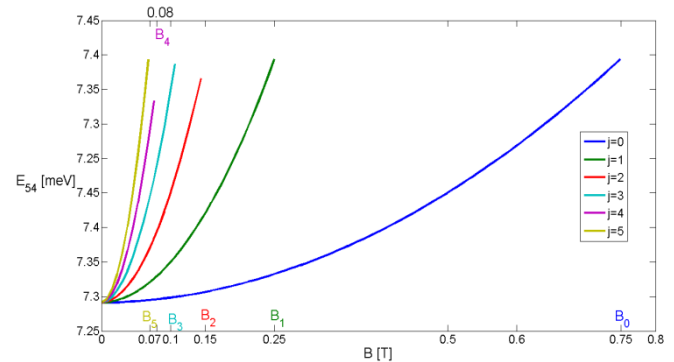


Fig. 10. Lasing energy difference for structure from [14] depending on magnetic induction for different Landau levels.

In Fig. 10 we can see that the energy difference of transition  $5 \rightarrow 4$  clearly has a square dependence on magnetic field which shows the importance of including the second order corrections from (1). Fig. 10 also indicates that possible tuning

is also not linear with magnetic field. In Figure 11 we can see an extensive decrease of the dipole matrix element for low magnetic field. If the condition in (3) were less rigorous these curves would reach minimal value below magnetic field of 1T. In eq. (4) we can see that the dipole matrix element has a second order polynomial dependence on  $B$ , and after the minimal value we would expect a rise of curves in Fig. 11 if the perturbation theory condition were less rigorous. This example illustrates the importance of modeling the dipole matrix element when an external magnetic field is applied. The results in Fig. 11 indicate that the dipole matrix element will deteriorate up to 8% for magnetic fields under 1T.

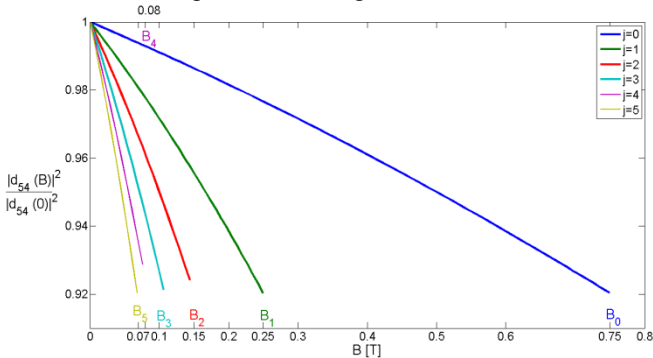


Fig. 10. Dipole matrix element squared,  $|d_{54}|^2$  for the structure from [14] as a function of magnetic induction for different Landau levels and  $|d_{54}(0)| = 711.3 \text{ \AA}$ .

In this example the dipole matrix element for optical transition  $3 \rightarrow 2$  used for resonant depletion decreases with magnetic field for both radiative and non-radiative transitions more extensively.

#### IV. CONCLUSION

In [4] the authors showed that TMM method in combination with NPE can be applied to various QCL structures. In this paper we generalized that model and presented how magnetic field influences QCL structures.

We presented effects of magnetic field on the dipole matrix element by using a 2<sup>nd</sup> order perturbation theory with Hamiltonian which includes NPE. We formed a model (1)-(3) which also includes a 1<sup>st</sup> order correction for envelope wavefunction and 2<sup>nd</sup> order corrections for energy. The application of the model is limited by the perturbation theory condition and the condition which arises from the dispersion

relation of the considered Hamiltonian. Applied to a QCL structure, this model gives us new insights on.

We showed that the dipole matrix element changes its values with different speed rates with Landau level and that in some cases the effects of external magnetic field on the dipole matrix element can not be neglected, especially in structures with high nonparabolicity (lower energy gap of quantum well material).

#### REFERENCES

- [1] M. Braun, U. Rossler, "Magneto-optic transitions and non-parabolicity parameters in the conduction band of semiconductors" *J. Phys. C: Solid State Phys.* 18, 3365-3379, 1985.
- [2] U. Ekenberg, "Nonparabolicity effects in a quantum well: Sublevel shift, parallel mass, and Landau levels" *Phys. Rev. B* 40 7714-7726, 1989.
- [3] V. Milanović, J. Radovanović, S. Ramović, "Influence of nonparabolicity on boundary conditions in semiconductor quantum wells" *Phys. Lett. A* 373, 3071-3074, 2009.
- [4] N. Vuković, J. Radovanović, V. Milanović, "Enhanced modeling of band nonparabolicity with application to a mid-IR quantum cascade laser structure" *Physica Scripta* T162, 014014, 2014.
- [5] C. Gmachl, F. Capasso, D. Sivco, A. Cho, "Recent progress in quantum cascade lasers and applications" *Rep. Prog. Phys.* 64 1533, 2001.
- [6] J. Faist, F. Capasso, D. Sivco, C. Sirtori, A. Hutchinson, A. Cho, "Quantum Cascade Laser" *Science* 264 553-556, 1994.
- [7] A. Kosterev, F. Tittel, "Chemical Sensors Based on Quantum Cascade Lasers" *IEEE J. Quantum Electron.* 38 582-591, 2002.
- [8] G. Wysocki, R. Lewicki, R. Curl, F. Tittel, L. Diehl, F. Capasso, M. Troccoli, G. Hofler, D. Bour, S. Corzine, R. Mualini, M. Giovannini, J. Faist, "Widely tunable mode-hop free external cavity quantum cascade lasers for high resolution spectroscopy and chemical sensing" *Appl. Phys. B* 92 305-311, 2008.
- [9] J. McManus, J. Shorter, D. Nelson, M. Zahnister, D. Glenn, R. McGovern, "Pulsed quantum cascade laser instrument with compact design for rapid, high sensitivity measurements of trace gases in air" *Appl. Phys. B* 92 387-392, 2008.
- [10] Z. Ikončić, V. Milanović, *Semiconductor Quantum Microstructures*, Belgrade, Republic of Serbia, University of Belgrade, 1997.
- [11] V. Golubev, V. Ivanov-Omskii, I. Minervin, A. Osutin, D. Polyakov "Nonparabolicity and anisotropy of the electron energy spectrum in GaAs" *Zh. Eksp. Teor. Fiz.* 88, 2052-2062, 1985. [Sov. Phys. JETP 61, 1214 (1985)].
- [12] J. Smiljanić, M. Žeželj, V. Milanović, J. Radovanović, I. Stanković, "MATLAB-based program for optimization of quantum cascade laser active region parameters and calculation of output characteristics in magnetic field" *Comput. Phys Commun.* 185, 998-1006, 2014.
- [13] B. Williams, S. Kumar, Q. Hu, J. Reno, "High-power terahertz quantum-cascade lasers" *Electron. Lett.* 42, 20063921, 2006.
- [14] H. Yasuda, I. Hosako, S. Miyashita, M. Patrashin "Terahertz electroluminescence from GaSb=AlSb quantum cascade laser" *Electronics Letters* vol.41, no.19, 1062-1063, 2005.

# Design of a 1 DOF MEMS motion stage for a parallel plane geometry rheometer

Yong-Sik Kim, Nicholas G. Dagalakis, Chiara Ferraris, and Svetlana Avramov-Zamurovic

**Abstract**— Rotational rheometers are used to measure paste properties, but the test would take too long to be useful for quality control (QC) on the job site. In this paper, a new type of rheometer is proposed based on a one degree of freedom (DOF) micro-electro-mechanical systems (MEMS)-based motion stage. Preliminary data will be presented to show the capability of the system to measure the viscoelastic properties of a paste. The parallel plate geometry rheometer consists of two plates, which move relative to each other to apply a strain to the material to be tested. From the stress measured and the strain applied, the rheological characteristics of the material can be calculated. The new device consists of an electrothermal actuator and a motion plate. For the rheological measurements, the device is designed to generate the shear stress up to 60 Pa and maintain its stiffness to less than 44 N/m. With these features, the device uses a square plate of 1.5 mm x 1.5 mm to provide enough area for a few microliter level volumes. The motion of the square plate is monitored by a capacitive sensor at the end of the oscillating plate which has a resolution of 1.06  $\mu\text{m}$ . When a reference cementitious paste, Standard Reference Material (SRM)-2492, is placed between the oscillating plate of the presented motion stage and a fixed plate, the reduction in the displacement of the oscillating plate is monitored showing that the presented motion stage is reasonably designed to detect the response of the reference cementitious paste.

**Index Terms**— MEMS, motion stage, electrothermal actuator, rheology, cement paste.

*Original Research Paper*  
DOI: 10.7251/ELSI1519045K

Manuscript received 1 November 2015. Received in revised form 24 November 2015.

This research was performed in part at the NIST Center for Nanoscale Science and Technology (CNST) Nano Fabrication Clean Room. This work was partially supported by the Sustainable Engineered Materials Program of the Materials and Structural Systems Division, Engineering Laboratory, National Institute of Standards and Technology, USA.

Y.-S. K. Author is with Intelligent Systems Division, Engineering Laboratory, National Institute of Standards and Technology, 100 Bureau Dr. Gaithersburg, MD, 20899, USA; e-mail: mk37do@gmail.com).

N. G. D. Author is with Intelligent Systems Division, Engineering Laboratory, National Institute of Standards and Technology, 100 Bureau Dr. Gaithersburg, MD, 20899, USA.

C. F. Author is with Materials and Structural Systems Division, Engineering Laboratory, National Institute of Standards and Technology, 100 Bureau Dr. Gaithersburg, MD, 20899, USA.

S. A. Z. is with Weapons and System Department United States Naval Academy, 105 Maryland Avenue, Annapolis, MD 21402, USA.

## I. INTRODUCTION

RHEOLOGICAL measurements of viscoelastic materials, especially cement pastes, are critical to obtain desirable material properties in civil engineering and related applications [1]. Concrete is the main material used in infrastructure construction (bridges, buildings...) and is composed of cement, water, sand, aggregate, and chemical additives. The rheological properties of concrete are related to the relative amounts of the components used especially to the rheological properties of the cement paste. The cement paste is composed of cement, water, and chemical additives. Cement could also be a blend of Portland cement and other fine powders such as fly ash and limestones. Thus a fast measurement method of the rheological properties of the cement paste would allow the engineer to optimize the concrete composition [2].

Rotational rheometer designs used to measure properties of cementitious materials from concrete [3, 4] to cement paste include parallel plates or concentric cylinders [5]. The principle of a rotational rheometer is to shear the material between two surfaces, by rotating one surface at a controlled speed and measuring the resulting torque. If the gap between the shearing surfaces is small enough, there are analytical equations to calculate the viscosity of the material. The rotation surface could rotate at a constant speed or oscillate at various frequencies [6, 7]. In this paper, the oscillatory method will be used.

To test cementitious materials, the commonly used oscillatory frequency ranges are between 0.2 Hz [6] and 1 Hz [7] depending on its application. The gaps between two plates are reported to be around 0.4 mm to 0.65 mm [2, 6]. In cement pastes, the general grain size is about 80  $\mu\text{m}$  to 100  $\mu\text{m}$  [5]. The measured shear or storage modulus varies from 100 Pa to 1.3 MPa [7]. Based on these data a micro electro mechanical systems (MEMS) rheometer for cement pastes was designed.

The idea to use MEMS technologies in rheological measurements for cement paste was motivated by the goal of building a cheap, disposable rheometer that could be used for quality control (QC) in the field. Conventional rotational rheometers like Thermo Scientific HAAKE MARS Rheometer<sup>1</sup> are expensive and are not portable. Moreover, it

<sup>1</sup> Certain commercial equipment is identified in this paper to adequately describe the experimental procedure. Such identification does not imply recommendation or endorsement by the National Institute of Standards and

would be advantageous to run multiple measurements at the same time of various composition of the paste to explore the influence of additives dosage or type on the cement paste rheological properties. Thus, a rheometer based on micro-electro-mechanical systems [8] would be advantageous. MEMS devices are small and low-cost [9, pp. 50–51], and can be designed to be mounted to run multiple experiments at the same time [10]. For the MEMS-based rheometer, the parallel plate geometry rheometers were used due to their simple structure.

A MEMS-based linear motion stage replaces the oscillating plate in the parallel plate rotational rheometers, and uses an optical method to measure their motion [8]. The electrostatic actuators are commonly used in MEMS-based linear motion stages for their long range motions but need a clean environment for their operations [11]–[13]. The rheometer has to apply enough shear force and be stable against materials that would flow outside the shearing plates, so thermal actuators are desirable for rheological systems for their milli-Newton level force and reliable operation under dirty or harsh environment.

This paper describes design and fabrication of 1 degree of freedom (DOF) linear motion stage for rheological measurement. This stage is composed of an actuator, an oscillating plate, and eight folded springs and each component is analyzed in the following section. An electrothermal actuator is adapted as an actuator and designed for its reliable operation in dusty environments [14], [15]. A capacitive displacement sensor is attached at the end of the oscillating plate to monitor its behavior and the large square plate of micro-scale level is used to hold the paste tested. This device is fabricated based on Silicon-on-Insulator Multi-User Multi-Processes (SOI-MUMPs) [16] and tested with a cementitious reference material, SRM-2492 [17] composed of an aqueous solution of corn syrup and limestone powder. The experimental results are obtained with the MEMS based 1 DOF linear motion stage and its application in a parallel plate rotational rheometer is discussed..

## II. DESIGN OF THE MEMS-BASED 1 DOF MOTION STAGE

Figure 1 illustrates the conceptual model of the parallel plate type MEMS-rheometer. The rheometer is composed of two plates; a stationary plate and an oscillating plate. A material will be placed between the two plates. In this paper, the stationary plate is an ordinary glass substrate and the oscillating plate will be replaced by the MEMS-based 1-DOF motion stage. When the oscillating plate applies a shear force to a material, its corresponding displacement is measured by the embedded sensor. The oscillating plate is a 1.5 mm x 1.5 mm square plate and is able to contain up to a few micro-liters of cementitious materials. The displacement and the shear force can be used to calculate the rheological properties of the material.

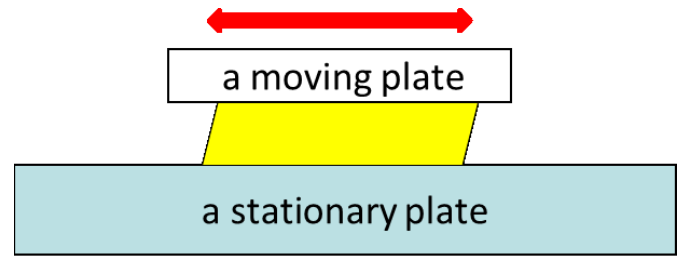


Fig. 1. The parallel plates type rheometer

The 1-DOF motion stage is composed of one dual-bent beam electrothermal actuator, an oscillating plate, and one embedded capacitive sensor and its schematic diagram is shown in Fig. 2(a). The oscillating plate is supported by eight folded springs which hold the plate in position and minimize its out-of-plane deformation when a test material is placed between the two plates. The dual bent-beam type electrothermal actuator consists of two bent-beam type electrothermal actuators in a series. With a serial connection, this actuator reduces its stiffness to 50 % of single bent-beam type electrothermal actuator, which makes the motion stage respond with more sensitivity during a material test. The details for each component are described in the following sections.

### A. The analysis for the dual-bent beam electrothermal actuator

The schematic model of the presented motion stage is illustrated in Fig. 2(a). In the dual bent-beam electrothermal actuator, two bent-beam type electrothermal actuators are connected to the same lateral bar. This serial connection reduces its stiffness in half, but the analytic relationship for the bent-beam actuator is still valid. There is a similar actuator reported as a one-ring spring actuator [18], where this lateral bar is thermally isolated and operates as a mechanical constraint. In this paper, the lateral bar is used to simply connect two bent-beam type actuators, because perfect thermal insulation of the lateral bar is hard to implement with MEMS fabrication technologies.

In this case, the total stiffness of the actuator,  $K_{act}$  can be expressed as a serial connection of two bent-beam actuators as

$$\frac{1}{K_{act}} = \frac{1}{K_{bent}} + \frac{1}{K_{bent}} \quad \text{or} \quad K_{act} = \frac{K_{bent}}{2} \quad (1)$$

where  $K_{bent}$  is the stiffness of the bent-beam type actuator. The output displacement of the motion platform will be expressed based on a parallel connection of springs as:

$$U_{plat} = \frac{F_{act}}{K_{act} + K_{plat}} \quad (2)$$

where  $F_{act}$  is the force generated by the dual bent-beam type actuator, and  $K_{plat}$  is the stiffness of the oscillating plate. Each term is explained in the following section.

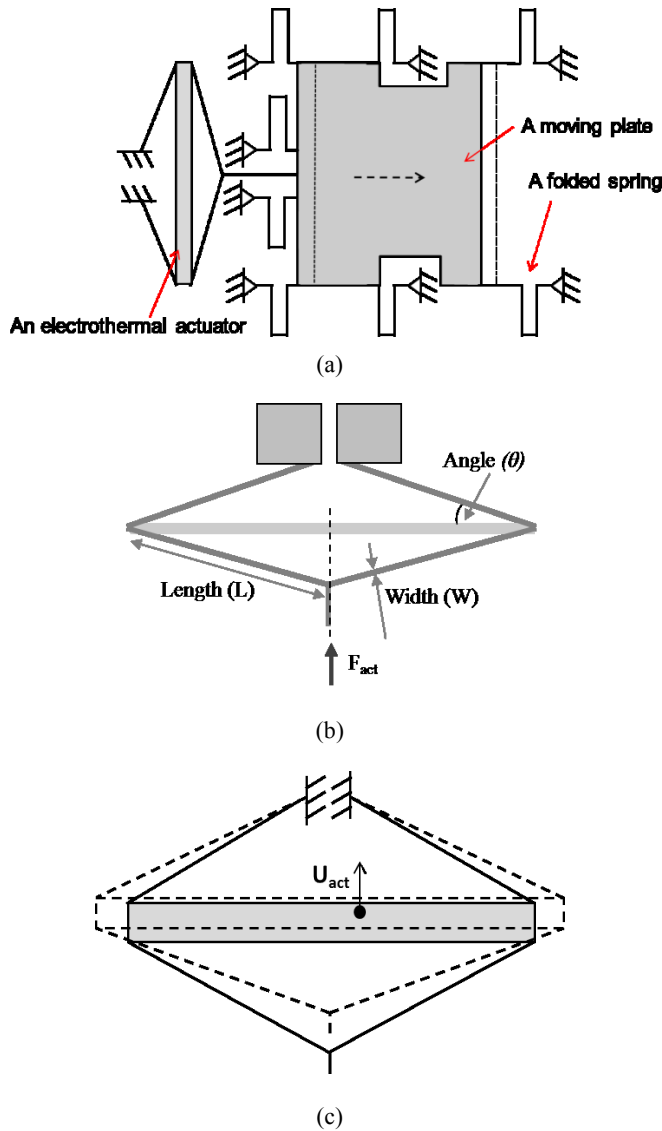


Fig. 2. The schematic model; (a) the presented 1-DOF motion stage; (b) the dual bent-beam electrothermal actuator; (c) the expected mechanical behavior of (b)

The schematic design of the presented dual bent-beam electrothermal actuator is shown in Fig. 2(b). The dual bent-beam is based on the thermal expansion of the lateral beam when the current flows through the actuators, whose expected behavior is shown in Fig. 2(c). In Fig. 2(c), the solid line stands for its original shape and a dotted line represents the expanded shape. Based on this mechanism, the stiffness of the actuator can be expressed [19] as:

$$K_{act} = n \frac{\sin^2 \theta E W T}{L} \quad (3)$$

where  $n$  is beam number,  $E$  is Young's modulus of silicon,  $W$  is the beam width,  $L$  is the beam length as described in Fig. 2(b), and  $T$  is the beam thickness. Equation (3) expects the stiffness of the presented dual bent-beam actuator would be 43.04 N/m based on the design parameters listed in Table 1.

As expected, this value is a half of the original bent-beam type actuator. The stiffness calculated in finite element analysis (FEA) is 43.7 N/m. These values indicate equation (3) predicts the stiffness with the error of less than 1 %.

The expected force from the actuator,  $F_{act}$  can be expressed based on a beam theory [20] and the geometric relationship between the lateral bar and two bent-type actuators as:

$$F_{act} = \alpha \Delta T_{ave} E T (W_{lateral} \tan \theta - 2n W \sin \theta) \quad (4)$$

where  $\alpha$  is coefficient of thermal expansion of silicon,  $\Delta T_{ave}$  is an average temperature rise of the actuator,  $W_{lateral}$  is the beam width of the lateral beam and  $T$  is the thickness, and  $\theta$  is the beam angle of the bent-beam actuator. Based on these relationships, the main design parameters are set and listed in Table 1.

TABLE I  
THE DESIGN PARAMETERS IN THE PRESENTED MOTION STAGE

Symbol	Design parameter	Values
$W$	Actuator beam width	22.37 $\mu\text{m}$
$\theta$	Actuator beam angle	0.8 degrees
$L$	Actuator beam length	2350 $\mu\text{m}$
$T$	Actuator beam thickness	30 $\mu\text{m}$
$n$	Number of beams in actuator	5
$L_{spring}$	Folded spring link length	1000 $\mu\text{m}$
$L_s$	Folded spring short link length	100 $\mu\text{m}$
$W_{spring}$	Folded spring link width	15 $\mu\text{m}$
$W_s$	Folded spring neck length	100 $\mu\text{m}$
$K_{plat}$	The stiffness of the oscillating plate	51.76 N/m
$K_{act}$	The stiffness of the actuator	43.7 N/m

### B. The folded springs

The folded spring shown in Fig. 3 supports the four corners of the oscillating plate, and is a compliant mechanism which transmits a translational motion without significant loss or motion error. The folded spring is made up of three cantilever beams and is located at corners and near the actuator as shown in Fig. 2(a). The main purpose of the eight springs is not only to allow only one directional motion, but also to reduce any out-of-plane deformation of the oscillating plate.

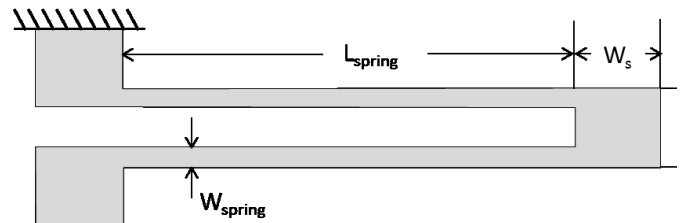


Fig. 3. The design of the folded spring

The stiffness of the oscillating plate is the summation of the stiffness of the eight folded springs [18] and can be expressed as:

$$\frac{2}{K_{plat}} = \frac{1}{ET} \left( \frac{L_{spring}^3}{2W_{spring}^3} + \frac{6(1+\mu)L_{spring}}{5W_{spring}} + \frac{L_s}{2W_s} + \frac{3L_{spring}^3 L_s}{2W_s^3} \right) \quad (5)$$

where  $\mu$  is the Poisson's ratio of silicon, and the other design parameters are indicated in Fig. 3. The value for each design parameter is listed in Table 1. Based on these geometries, the stiffness of the oscillating plate is about 53.4 N/m based on equation (3). With the design parameters described above, equation (2) can be extended as:

$$U_{plat} = \frac{2\alpha EW T \sin\theta}{3kp \left( n \sin^2 \theta \frac{EWT}{L} + K_{plat} \right)} V^2 \quad (6)$$

where  $\alpha$  is the coefficient of thermal expansion of silicon,  $K_{plat}$  is given by Eq. (5), and  $V$  is the driving voltage applied to the actuator. Equation (6) indicates that the displacement of the motion stage is proportional to the square of the driving voltage.

### III. FINITE ELEMENT ANALYSIS (FEA)

Finite element analysis (FEA) simulation [21] is also utilized to verify the analysis described above and predict the thermal and structural behavior of the presented motion stage. The material properties used in the FEA are cited from a previous publication [20] and the same wafers are utilized in the fabrication. In this simulation, the ends of the eight folded springs and the ends of the actuator are assumed to be firmly fixed for structural analysis and they are connected to a heat sink at room temperature of 20 °C for thermal analysis.

The expected mechanical behavior is calculated in FEA and plotted in Fig. 4(a). This is the response corresponding to the excitation by the driving voltage of 5 V. This is calculated to result in the temperature rise of 542.6 °C. This temperature value is close to the maximum endurable limit of silicon; 550 °C [22], so the displacement by this can be interpreted as the maximum displacement of the motion stage without any permanent damage. The stress distribution is also visualized based on von Mises stress in Fig. 4(b). The expected maximum stress will be 193 MPa and distributed near the folded springs and the actuator when the oscillating plate is in its operation. This indicates that the stiffness of the folded spring and the square plate are well adjusted. In addition to this, the maximum value is far less than the yield strength of silicon 7 GPa, so the calculated displacement shown in Fig. 4(a) is expected to be repeatable without any permanent damage.

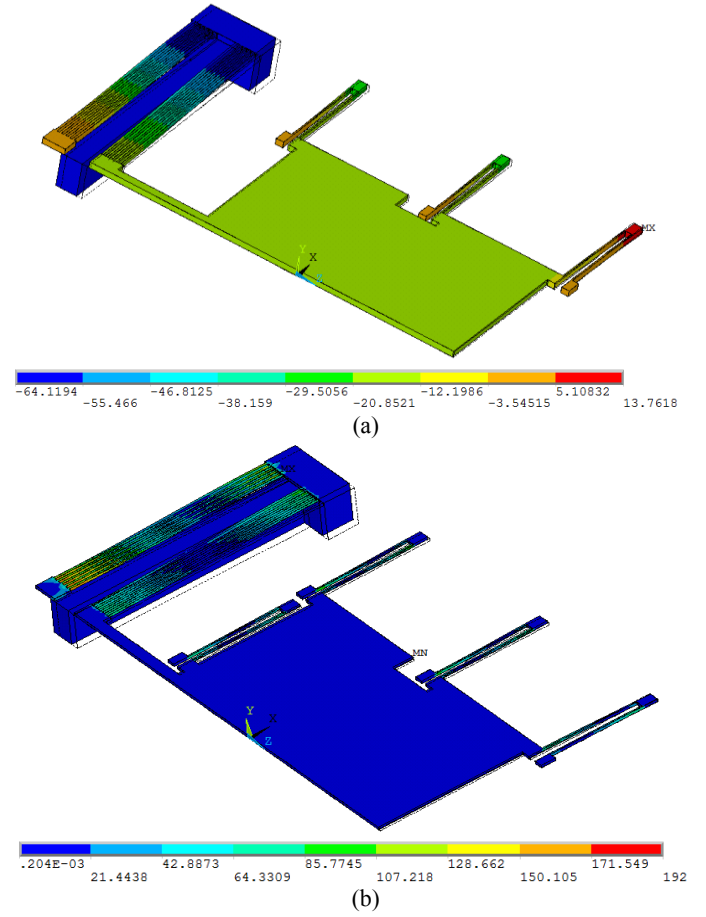


Fig. 4. FEA simulation results by the temperature rise up to 542.6 °C; (a) the displacement vector sum (in  $\mu\text{m}$  unit); (b) von Mises stress distribution over the stage (in MPa unit)

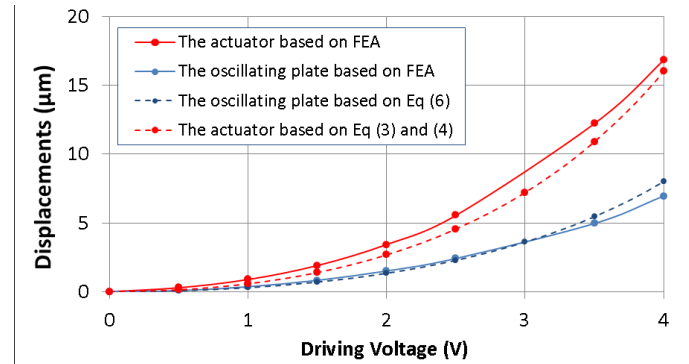


Fig. 5. The calculated displacement of the oscillating plate and the actuator from FEA and analytic relationship

The relationship between the driving voltage and the corresponding output displacement is also inspected in FEA. The displacement of the oscillating plate is calculated based on the driving voltage and plotted in Fig. 5. The actuator is expected to generate more motions than the oscillating plate. This behavior is also compared with the analytic relationship from the previous section; the displacement of the motion stage is calculated based on Eq (6) and that of the actuator is from Eq (3) and Eq (4). These calculations are plotted in

dotted lines in Fig. 5, which indicates that the analytic relationship in the previous section shows reasonable trends

compared with FEA, as a function of the driving voltage.

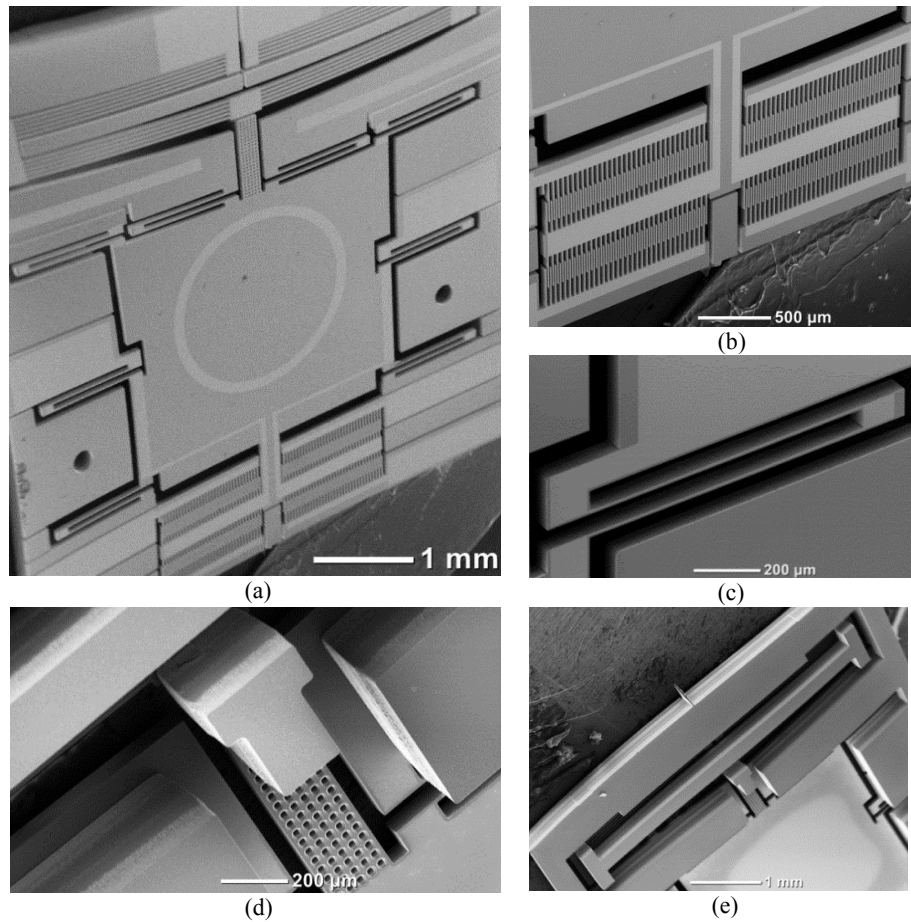


Figure 6: SEM images of a fabricated motion stage; (a) a frontal full view, (b) an embedded capacitive sensor, (c) a close-up view of a the folded spring, (d) the connecting block underneath the lateral bar in (e), (e) the backside view of the lateral bar in the actuator

#### IV. MICRO-FABRICATION

The fabrication process for the oscillating plate follows standard MEMS fabrication processes: Silicon-On-Insulator Multi-User Multi-Processes (SOI-MUMPs) [16] and a Silicon-On-Insulator (SOI) wafer. The SOI wafer used for the presented motion stage consists of a  $30\ \mu\text{m}$  thick device layer, a  $400\ \mu\text{m}$  thick handle layer, and a  $2\ \mu\text{m}$  thick buried oxide layer. The fabrication process consists of four steps – one metal deposition process on the device layer of a SOI wafer, two deep reactive ion etching (DRIE) processes for the device layer and the handle layer of an SOI wafer, and the removal process of a buried oxide layer. The details about this fabrication are described in details in a similar MEMS-based motion stage study [20].

Based on the fabrication procedure described above, the presented motion stage has been fabricated with an embedded capacitive sensor. Their detailed images are shown in Fig. 6, where the bright white areas are electric paths for the actuator and the embedded capacitive sensors. Grey areas are made of silicon and black areas are holes through the wafer. The full frontal view of the presented motion stage is shown in Fig.

6(a), where the dual bent-beam electrothermal actuator, the oscillating plate, and the embedded capacitive sensor are linked to each other. Figure 6(b) is the detailed image of the embedded sensor, which is made up of multiple interdigitated fingers and able to generate differential output from two pairs of finger groups to eliminate resident capacitance. The close-up view of the folded spring is shown in Fig. 6(c), where the bright line is an electric wire conductive path for the embedded capacitive sensor. The actuator is electrically disconnected from the oscillating plate by a physical gap, which is supported by the connecting block underneath it in Fig. 6(d). Figure 6(e) is the backside of the actuator. The lateral bar underneath the actuator will hold the whole actuator for reliable operation.

#### V. EXPERIMENTAL RESULTS

The mechanical response of the presented motion stage and the embedded capacitive sensor was experimentally evaluated. For this experiment, two metal pads near the actuator are electrically connected to direct current (DC) power supply units (Agilent Model 3322A<sup>1</sup>) to control the actuator. The two

electrodes and one ground of the embedded capacitive sensor are connected to an Analog Device<sup>1</sup> single channel Capacitive-to-Digital converter AD7747<sup>1</sup> [22], which converts the capacitance change into voltage information for computers. With these features, the displacements of the oscillating stage are measured separately by an optical profiler (VEECO<sup>1</sup> NT1100 [23]), which will be used as a reference value to evaluate the capabilities of the embedded capacitive sensor.

embedded sensor is expected to be 1.06  $\mu\text{m}$ . With this calibrated sensor, the displacement of the oscillating plate is measured through the embedded capacitive sensor, when the cementitious material is loaded and unloaded, respectively. The operating frequency used for all the tests was 0.5 Hz and various displacements are tested. The corresponding experimental results are shown in Fig. 7.

Water will evaporate from the paste material when exposed to the atmosphere and thus the particles will interlock, as shown in Fig. 7(a). With the reference material SRM-2492, the results obtained less than 5 min after being placed on the oscillating plate have no significant change, but the values are really low after 15 min, indicating a significant change in the material, probably due to water evaporation. Based on this observation, all tests are done within 5 min after the sample is exposed to air.

Figure 7(b) shows the reduction of the displacements of the oscillating plate when a sample material is loaded between the oscillating plate and a fixed plate as described in Fig. 1. The reference material for the paste rheometers is placed on the stationary plate with a nano-liter syringe [24]. After the reference material is placed between the two plates, the size of the physical gap between the two plates will be measured with the NT1100 and the approximate contact area of the material is visually measured under a microscope. The motion of the oscillating plate decreases by about 44 % when the target material is loaded. This reduction indicates that the design of the presented motion stage is designed reasonably to be sensitive to the changes due to a sample and the embedded sensor is able to detect the change of the motion to this degree. This difference is plotted and compared with FEA as a function of a driving voltage in Fig. 7(c). The cases with a sample loaded and unloaded show a similar pattern with the expectation based on FEA.

The shear rate and displacement of the oscillating plate will be controlled by the amplitude of the injection voltage and its operating frequency. Figure 8 shows the various motions with the driving voltage from 2 V to 5 V showing that the different shear rate is expected with the presented motion stage. Based on these experimental data and the analytic relationship, a Bingham model [25] can be built for further analysis later. These are preliminary data but it shows that MEMS could be used to measure the rheological properties of paste. Further tests are needed and also, a wider range of shear rate would be desirable to probe ranges that are useful in the construction industry.

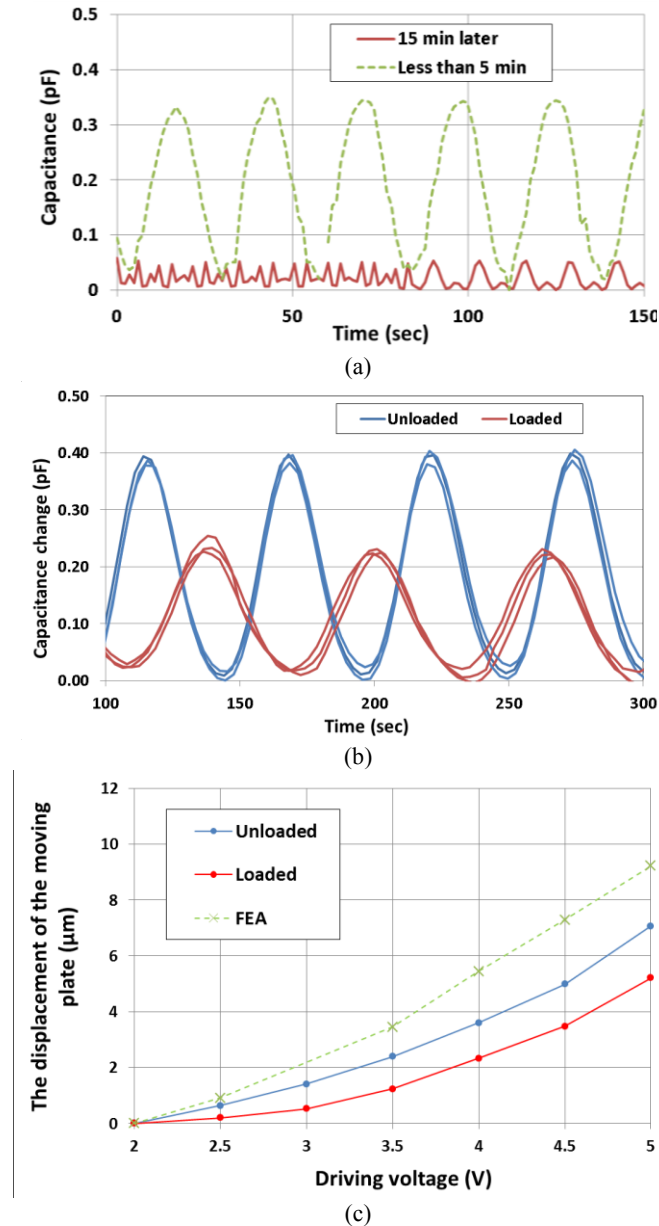


Figure 7: Experimental results of the displacement of the motion stage for two cases; sample loaded and unloaded: (a) the motion after the paste is exposed to air, (b) the difference of the capacitance with a paste being loaded and unloaded, (c) the capacitance change of (b) as a function of a driving voltage

The embedded sensor measured the capacitance change from the motion from a few microns to tens of microns. Based on the measurements from NT1100<sup>1</sup>, the capacitance-to-displacement ratio of the embedded sensor was obtained, which is 106.41  $\mu\text{m}/\text{pF}$ . The Capacitive-to-Digital converter chip has the accuracy of 10 fF, so the resolution of the

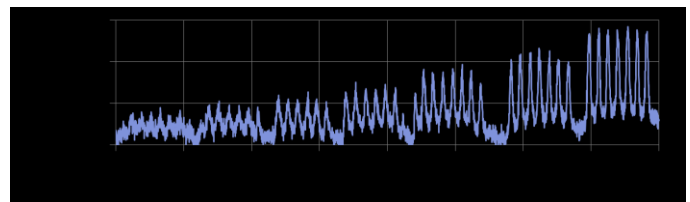


Figure 8: Capacitance sensor output for different actuator driving voltage amplitude rates

## VI. CONCLUSION

The design, fabrication, and testing of a MEMS based motion stage has been presented for rheological properties measurement of paste type materials. This MEMS based system is designed to replace the parallel plate rotational rheometers. For the rheological application, the presented motion stage adopts (1) the dual bent-beam type electrothermal actuator for a low stiffness operation, (2) a large square plate to contain enough cementitious material, (3) an embedded capacitive sensor to monitor the displacement of the motion stage, and (4) derive a Bingham mathematical model to represent cementitious materials. Through these procedures, the presented rheometer is able to generate rheological data of up to the shear rate of 0.0275 1/s and the shear stress of 45 Pa.

Compared with conventional rheometers, this MEMS-based rheometer provides more detailed information in a relatively short shear rate range. Design optimization or a new design concept is needed to compensate the missing shear rate change. Further analysis and tests are required to apply for new applications such as biomedical or gels for their viscoelastic properties.

## REFERENCES

- [1] Brower, Lynn and Ferraris, Chiara F., "Comparison of Concrete Rheometers: International Tests," *Concr. Int.*, pp. 41 – 47, Vol. 25 #8, 2003
- [2] C. F. Ferraris, Measurement of the rheological properties of cement paste: a New Approach, Int. RILEM Conf., *The role of Admixtures in High Performance Concrete*, J. G. Cabrera and R. Rivera-Villareal, eds., Monterrey (Mexico) March (1999) pp. 333-342 (<http://ciks.cbt.nist.gov/monograph/>).
- [3] C. Ferraris, L. Brower editors, "Comparison of concrete rheometers: International tests at LCPC (Nantes, France) in October 2000", *NISTIR 6819*, 2001 (<http://fire.nist.gov/bfrlpubs/build01/PDF/b01074.pdf>)
- [4] C. Ferraris, L. Brower editors, "Comparison of concrete rheometers: International tests at MB (Cleveland OH, USA) in May 2003", *NISTIR 7154*, 2004 (<http://ciks.cbt.nist.gov/~ferraris/PDF/DraftRheo2003V11.4.pdf>).
- [5] G. Marin, A. A. Collyer, and D. W. Clegg, *Rheological Measurements*. Collyer, AA, Clegg, D. W., Eds, 1988.
- [6] L. J. Struble and M. A. Schultz, "Using creep and recovery to study flow behavior of fresh cement paste," *Cem. Concr. Res.*, vol. 23, no. 6, pp. 1369–1379, 1993.
- [7] Z. Sun, T. Voigt, and S. P. Shah, "Rheometric and ultrasonic investigations of viscoelastic properties of fresh Portland cement pastes," *Cem. Concr. Res.*, vol. 36, no. 2, pp. 278–287, 2006.
- [8] G. F. Christopher, J. M. Yoo, N. Dagalakis, S. D. Hudson, and K. B. Migler, "Development of a MEMS based dynamic rheometer," *Lab. Chip*, vol. 10, no. 20, pp. 2749–2757, 2010.
- [9] M. J. Madou, "*Fundamentals of microfabrication*. 2002," Boca Raton Fla. CRC Press, vol. 200, pp. 298–205.
- [10] K. A. Ronaldson, A. D. Fitt, A. R. H. Goodwin, and W. A. Wakeham, "Transversely Oscillating MEMS Viscometer: The 'Spider,'" *Int. J. Thermophys.*, vol. 27, no. 6, pp. 1677–1695, 2006.
- [11] Q. Yao, J. Dong, and P. M. Ferreira, "Design, analysis, fabrication and testing of a parallel-kinematic micropositioning XY stage," *Int. J. Mach. Tools Manuf.*, vol. 47, no. 6, pp. 946–961, 2007.
- [12] D. Mukhopadhyay, J. Dong, E. Pengwang, and P. Ferreira, "A SOI-MEMS-based 3-DOF planar parallel-kinematics nanopositioning stage," *Sens. Actuators Phys.*, vol. 147, no. 1, pp. 340–351, 2008.
- [13] Y. Ando, "Development of three-dimensional electrostatic stages for scanning probe microscope," *Sens. Actuators Phys.*, vol. 114, no. 2, pp. 285–291, 2004.
- [14] J.-S. Park, L. L. Chu, E. Siwapornsathain, A. D. Oliver, and Y. B. Gianchandani, "Long throw and rotary output electro-thermal actuators based on bent-beam suspensions," in *Micro Electro Mechanical Systems*, 2000. MEMS 2000. The Thirteenth Annual International Conference on, 2000, pp. 680–685.
- [15] W.-C. Chen, P.-I. Yeh, C.-F. Hu, and W. Fang, "Design and characterization of single-layer step-bridge structure for out-of-plane thermal actuator," *Microelectromechanical Syst. J. Of*, vol. 17, no. 1, pp. 70–77, 2008.
- [16] K. Miller, A. Cowen, G. Hames, and B. Hardy, "*SOIMUMPs design handbook*," MEMScAP Inc Durh., 2004.
- [17] Ferraris C.F., Stutzman P., Winpigler J., Guthrie W., "Certification of SRM 2492: Bingham Paste Mixture for Rheological Measurements" , *SP-260-174 Rev. 2012*, June 2012 ([http://www.nist.gov/manuscript-publication-search.cfm?pub\\_id=911268](http://www.nist.gov/manuscript-publication-search.cfm?pub_id=911268))
- [18] J. K. Luo, A. J. Flewitt, S. M. Spearing, N. A. Fleck, and W. I. Milne, "Three types of planar structure microspring electro-thermal actuators with insulating beam constraints," *J. Micromechanics Microengineering*, vol. 15, no. 8, p. 1527, 2005.
- [19] J. K. Luo, A. J. Flewitt, S. M. Spearing, N. A. Fleck, and W. I. Milne, "Modelling and fabrication of microspring thermal actuator," in *Nanotech 2004 Vol.1: Technical Proceedings of the 2004 NSTI Nanotechnology Conference and Trade Show*, vol. 1, Nano Science and Technology Institute, 2004, pp. 355–358.
- [20] Y.-S. Kim, J.-M. Yoo, S. H. Yang, Y. M. Choi, N. G. Dagalaks, and S. K. Gupta, "Design, fabrication and testing of a serial kinematic MEMS XY stage for multifinger manipulation," *J. Micromechanics Microengineering*, vol. 22, no. 8, 2012.
- [21] ANSYS Fluent, "*12.0 User's Guide*," User Inputs Porous Media, p. 6, 2009 on <http://www.ansys.com>.
- [22] Analog Device, AD7747, 24-bit, 1 channel capacitance to digital converter on <http://www.analogdevice.com>.
- [23] "Dynamic MEMS Measurement Option for Wyko NT1100 Optical Profilers." on <http://www.veeco.com>
- [24] "MICROMAN." Positive-displacement pipet, M10 model on <http://www.gilson.com/Pipette/Products/44.224>
- [25] Hackley V. A, Ferraris C.F., "The Use of Nomenclature in Dispersion Science and Technology" NIST Recommended Practice Guide, SP 960-3, 2001, <http://fire.nist.gov/bfrlpubs/build01/art108.html>

# MEMS mirrors using sub-wavelength High-Contrast-Gratings with asymmetric unit cells

Milan Maksimović

**Abstract**—High-contrast gratings (HCG) are ultra-thin elements operating in sub-wavelength regime with the period of the grating smaller than the wavelength and with the high-index grating material fully surrounded by low-index material. Design of MEMS mirrors made from HCG with specific reflectivity response is of great practical interest in integrated optoelectronics. We theoretically investigate design of the spectral response for HCGs with the complex unit cells. We show that the spectral response can be tailored via the unit cell perturbations and with the asymmetric unit cell perturbations may introduce completely new spectral response. Our results can serve as guidance for the design of the complex HCGs and help with the choice of the efficient initial grating topology prior to global optimization procedure.

**Index Terms**—High index contrast, subwavelength grating, MEMS, optical phased array.

*Original Research Paper*  
DOI: 10.7251/ELS1519052M

## I. INTRODUCTION

THE optical grating is an important and widespread element used for manipulating or tailoring the spatial, temporal and spectral properties of light. A new type of high-contrast gratings (HCG) has been proposed recently, see [1]. HCGs are ultra-thin elements operating in the sub-wavelength regime, with a period of the grating smaller than the wavelength and with high-index grating material fully surrounded by low-index material. These structural characteristics of HCGs give rise to a variety of novel features with a great importance in integrated optoelectronics such as: ultra-broadband high reflectivity, high-quality-factor resonances, wave front phase control for planar focusing reflectors and lenses in integrated optics, etc. [1]-[4].

The motivation for extensive research in the manufacturing and design of HCGs and for their practical use has been to obtain an alternative for the distributed Bragg reflectors (DBR) for broadband high-reflectivity filtering applications [2]-[5]. The nature of HCGs dictates that their spectral response is very dependent on the polarization and as such it is applied for polarization control filters [6]. Also, novel ultra-

low loss hollow-core waveguides are possible with the use of two HCGs as highly reflectivity mirrors [7]. Very interesting recent results emphasize the use of non-periodical and non-uniformly scaled HCG to imprint local phase shift onto an incident wave and to achieve focusing on a very small scale [8-9].

Modeling of HCGs can be effectively performed by numerous numerical methods for modeling optical response of gratings [10]. In this paper, we perform numerical simulations using the well known rigorous coupled wave analysis (RCWA) [11] in our own implementation. An important aspect of modeling HCGs is the use of different approximation methods, loosely named coupled-mode theory, that reveal some insight into the peculiar nature of HCGs electromagnetic response [12]-[16].

Another important technology is MEMS (micro-electromechanical systems), because it enables the application of silicon fabrication technologies to the development of micro optical elements in general [17],[18]. Fabrication of HCGs as MEMS mirrors structures or other integrated optoelectronics elements has been demonstrated [1].

Design and optimization of specific spectral, angular or spatial characteristics for periodic HCGs is of great practical interest. Recently, we investigated modeling and optimization of 1D HCGs with a periodic grating structure but with a complex unit cells topology [19]-[20]. The main emphasis of our paper is on the theoretical analysis suitable for the design of HCGs with prescribed spectral properties such as broadband reflection or high-Q resonances. In our approach, optimization tasks could be facilitated if we start with a design that already possesses the desired features.

In this paper, we further exemplify our method for spectral tailoring with the perturbations of the HCGs unit cell topology. We start with an analysis of the periodic HCGs supporting high broadband reflectance. Second, structural perturbations in the form of deformed unit cells are introduced into the simple periodic structures already optimized for the specific broadband response. Third, we analyze reflection/transmission resonances in the structure where the unit cell is symmetrically or asymmetrically perturbed. In the examples we provide, the role of the unit cell symmetry is revealed as the origin of spectral resonances. Finally, we make some comments on further applications of HCG mirrors for tailoring phase response.

## II. HIGH CONTRAST GRATINGS MODELING

### A. Modeling HCGs with general methods

The common form of HCG is a periodic array of rectangular high-index bars surrounded by low index material.

Manuscript received 12 October 2015 (write the date when you have first sent the manuscript for review). Received in revised form 20 October 2015 (write the date when you have sent the manuscript in its revised form if revisions required for your paper after review).

Milan Maksimović is with the Focal-Vision and Optics, Enschede, The Netherlands (corresponding author to provide phone: +31-053-4287-885; e-mail: milan.maksimovic@focal.nl).

The HCG is excited by plane wave excitation with defined polarization and under a normal or oblique incidence angle. The period of the grating structure is smaller than the wavelength of the incoming wave and hence the HCG is sub-wavelength. This means that only the zeroth diffraction order mode is propagating outside the grating region. In the case of oblique incidence the sub-wavelength operating condition of  $\Lambda > \lambda$  is replaced by  $(1+\sin\theta) \Lambda > \lambda$  for oblique incidence.

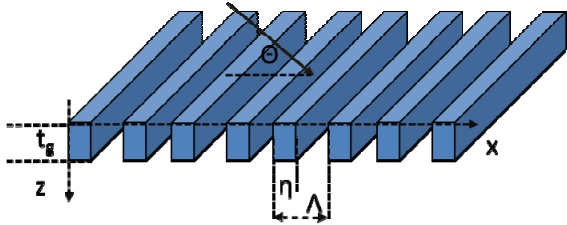


Figure 1 Basic geometry of high index contrast grating with a unit cell period  $\Lambda$  and high index bar width  $\eta\Lambda$ , where  $\eta$  is the duty cycle of the grating and  $t_g$  is the grating height. The structure is periodic in the  $x$ -direction, and is infinitely extended in the  $y$  direction with the plane wave incident from the top under an incidence angle  $\Theta$ .

The structure depicted in Figure 1 is invariant along the  $y$ -direction and illuminated by the incident plane wave under an angle  $\Theta$ . The electromagnetic field can be decomposed into two different polarizations TE (with  $E_y, H_x, H_z$  the only non-null components) and TM (with  $H_y, E_x, E_z$  the only non-null components). The wave equations can be written in the compact form:

$$\mathbf{L}_{\text{TE(TM)}} \Phi(x, z) = -\frac{1}{k^2} \partial_z^2 \Phi(x, z), \quad (1)$$

with  $\Phi(x, z)$  representing either  $E_y$  or  $H_y$  component depending on polarization. The operator  $\mathbf{L}$  is defined as:

$$\mathbf{L}_{\text{TE}} = \frac{1}{k^2} \partial_z^2 + n^2(x), \quad (2)$$

$$\mathbf{L}_{\text{TM}} = \frac{1}{k^2} n^2(x) \partial_x \frac{1}{n^2(x)} \partial_x + n^2(x), \quad (3)$$

with  $k=2\pi/\lambda$  and  $n(x)$  being the refractive index distribution. Since the operator  $\mathbf{L}$  does not depend on the  $z$ -variable, the separation of variables leads to the representation

$$\Phi(x, z) = \varphi(x) e^{\pm ikz} \quad (4)$$

where  $\varphi$  is the eigenfunction for corresponding eigenvalue problem

$$\mathbf{L}_{\text{TE(TM)}} \varphi(x) = r^2 \varphi(x) \quad (5)$$

Owing to the periodicity of the structure the eigenfunctions are pseudo-periodic  $\varphi(x + \Lambda) = \varphi(x) e^{\pm ik\alpha\Lambda}$  with  $\alpha = \sin(\Theta)$  determined by the incidence angle while the square root of the eigenvalue is chosen in such way that  $\text{Im}(r) < 0$  or  $r > 0$  if the eigenvalue is real. The solutions in the exterior of the grating can be expressed in terms of propagating and evanescent plane wave components

$$\Phi_{\text{IN}}(x, z) = \Phi_{\text{inc}}(x, z) + \sum_m r_m e^{-i(k_x x + k_z z)}, \quad (6)$$

$$\Phi_{\text{OUT}}(x, z) = \sum_m t_m e^{-i(k_x x + k_z(z-t_g))}, \quad (7)$$

where  $r_m, t_m$  are reflection and transmission coefficients. Owing to the periodicity of the geometry and the fact that the grating is homogeneous in the propagation direction ( $z$ -axis), the permittivity and the field components can be represented by Fourier expansion. Further, boundary conditions are used for the neighboring regions to form a matrix representation and enable the calculation of the coupling coefficient for each Fourier component. This mathematical method is known as the rigorous coupled wave analysis method (RCWA) and it has been widely applied in solving grating problems of different complexity [10]-[11]. Furthermore, the symmetry of the structure plays an important role in the form of general solution. HCG has a standard discrete and continuous translations symmetry but additional symmetries such as mirror symmetry of the unit cell may further restrict the solution to the full problem. Other general purpose methods such as finite element method (FEM) or finite difference time domain (FDTD) method can be used to model HCG structures, see [11] for an overview.

### B. Modeling HCGs: coupled mode theory (CMT)

There are several semi-analytical, approximate methods relying on an expansion of the fields in the grating region in a specially chosen basis. These formalisms rely on the expansion using periodic waveguide modes as the basis for the field representation in the grating region and have been developed in several versions under the name as the coupled mode [1], [13] or the coupled Bloch-mode method [12]. Another version of the coupled mode approach has been derived in [15].

An essential part of the method is to identify waveguide modes in the grating region and their interaction as responsible for transfer of energy across the grating [1],[13],[14]. Many interesting physical effects can be understood in terms of resonant excitation of leaky modes (Bloch modes of periodic waveguide) supported by the structure. Under normal incidence the excitation of two coupled Bloch-modes and their destructive interference are responsible for the spectral properties of HCGs such as broadband reflection. In the case of oblique incidence more complicated interactions that include different and numerous waveguide modes are important.

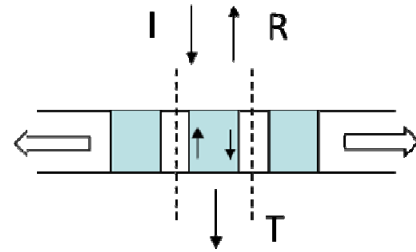


Figure 2 Sketch of the high index contrast grating with depiction of excited waveguide modes in the grating region. Interference of these modes is responsible for all properties of HCGs.

Further, in the deep subwavelength region the Effective Medium Theory is a very useful tool [12], while its applicability relies on the excitation of a single propagating mode. Hence, it does not predict the features of the spectral response for HCGs in the case where (small) number of modes

is excitable. In the case of simple structures these CMT and similar approaches offer valuable insights into the physics of HCGs, but as pure numerical methods they do not outperform the standard RCWA in terms of convergence properties for more complex structures and across full parameter space [1]. In addition, these methods can give an insight into the design with the semi-analytical formalism they provide. Also, a parallel between HCGs and 1D photonic crystals has been explored in literature [16].

### III. DESIGN OF HCG MIRRORS

#### A. HCGs mirror with broadband reflection

An important property of HCGs is possibility to design a broadband reflection response for integrated mirrors that are also ultra-thin and lightweight compared to other solutions [1].

The design parameters for broadband HCG mirrors are the grating period  $\Lambda$ , the grating thickness  $t_g$  and the duty cycle  $\eta$ , whereas the grating refractive index is a given parameter. The first step in design using numerical methods like RCWA is the parameter analysis of the reflection spectrum using scaled parameters. The second step is local optimization using a suitably chosen merit function [21] like the one given in equation below:

$$MF = \frac{\Delta\lambda}{\lambda_0} \frac{1}{N} \sum_{\lambda=\lambda_1}^{\lambda_2} R_{TE(TM)}(\lambda) g(\lambda) \quad (8)$$

where  $\Delta\lambda=\lambda_2-\lambda_1$  is the expected bandwidth around the central wavelength  $\lambda_0$  which is assumed to be in the middle of the required range,  $R(\lambda)$  is the spectral reflectance for a chosen polarization calculated numerically and  $g(\lambda)$  is a suitably chosen Gaussian function. Once the optimal parameters of HCGs are found using the chosen local or global algorithm, the tolerances of HCGs parameters can be investigated. In the final step, the structure can be optimized to have not only good efficiency but also large tolerance values.

Interestingly, semi-analytical methods of the coupled mode theory enable physical understanding and efficiency in pre-design of broadband reflection [1]. Namely, the nature of HCGs for a specific set of parameters supports only 2 waveguide modes that exist simultaneously in the grating region. These two contra-propagating modes are mutually interfering and can be made to destructively interfere at the exit port of the HCG. In this situation the response is characterized with a very broad bandwidth of high reflectivity. This particular physical picture has been confirmed in literature using similar couple-mode approaches [12]-[15].

We consider a design example of a broadband mirror operating for an TM polarization and formed by silicon bars of refractive index  $n_g=3.48$  and a duty cycle  $\eta=0.75$ , fully immersed in air.

Three distinctive operating regions can be identified with the HCGs: diffraction region, near-wavelength region and deep-sub-wavelength region. In the first region, many diffraction modes beyond zero modes are excited. In the second region HCG parameters are such that the grating is already in the sub-wavelength domain and its response is characterized by excitation of a small number of Bloch (waveguide) modes. This region is most interesting for realization of a high reflectivity broadband response. Finally in the third region the

HCG is operating in the deep sub-wavelength domain where only a single propagating mode is excited, the spectral response is without resonance features and the effective mode theory explains well the HCG operation. The reflectivity map shown in Figure 3 can serve as the basis for selecting a suitable period and height (depending on the chosen wavelength) to achieve broadband reflection, which is in this case  $\Lambda=0.75 \mu\text{m}$ , thickness  $t_g=0.48 \mu\text{m}$ . The spectral reflectivity for these parameters is shown in Figure 4. The broadband reflectivity is a consequence of interference of the waveguide modes supported by the structure.

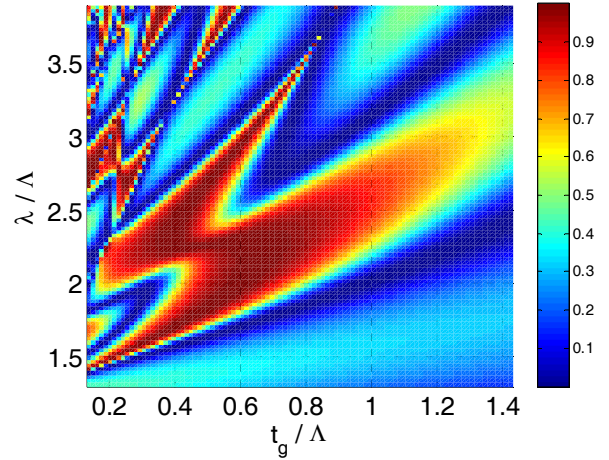


Figure 3 Reflection response dependence on normalized wavelength and grating thickness for TM polarized illumination with normal incidence for a HCG with the duty cycle  $\eta=0.75$ , high index material  $n_g=3.48$  and low index material  $n_0=1$ .

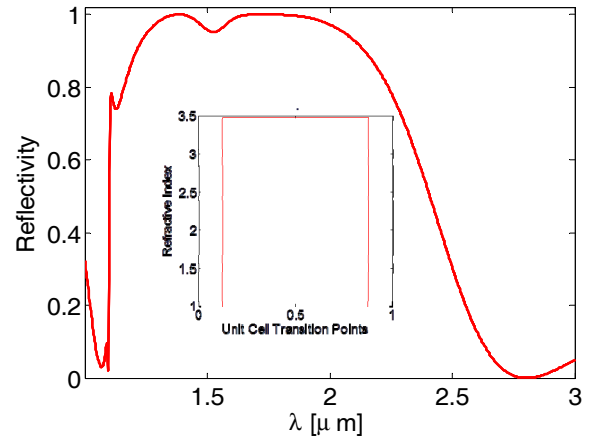


Figure 4. Reflection response (TM polarization, normal incidence) for HCG with the period  $\Lambda=0.77 \mu\text{m}$ , duty cycle  $\eta=0.75$ , thickness  $t_g=0.480 \mu\text{m}$ , high index material  $n_g=3.48$  and low index material  $n_0=1$ .

#### B. Shaping spectral reflectivity in HCGs mirror with asymmetrical unit cell

The first possible method for tailoring the spectral response is the introduction of defects or asymmetries in the unit cell of the periodic structure. This strategy already proved successful in controlling the excitation of guided resonances in the case of photonic crystal slabs with aperiodically structured unit cells [22]-[27]. The second method starts with a full aperiodic design for HCG, beyond the unit cell. This approach has been

used in photonics and plasmonics to enable tailoring of the spectral response and field profiles [16],[22]. Previously, we analyzed the construction of HCGs with complex unit cells where the topology of the unit cell is derived from a deterministic aperiodic sequence [16].

We consider symmetric and asymmetric perturbations of the periodic structure optimized for broadband reflection, see Fig. 5. We introduce a perturbation of the structure by the repositioning the transition points in the unit cell

$$x_1^p = x_1^0 - \Delta x; x_2^p = x_2^0 + \Delta x; x_{3(4)}^p = x_c \pm \Delta x \quad (9)$$

$$x_c = (x_1^0 + x_2^0)/2; \Delta x = p(x_2^0 - x_1^0) \quad (10)$$

where  $x_n^p$  represents a new set of transition points in the symmetrically perturbed structure starting from the original transition points  $x_n^0$ ,  $\Delta x$  is the relative transition point shift with the parameter  $p$  describing the relative perturbation calculated with respect to the width of the high index bar,  $x_c$  is the central point in the symmetric unit cell. New transition points are calculated in a similar fashion for an asymmetrically perturbed structure with the omission of the perturbation on the one side of the central high index bar. In all cases we keep the total content of the high index material the same between the original and the perturbed structure so that the effective refractive index remains the same.

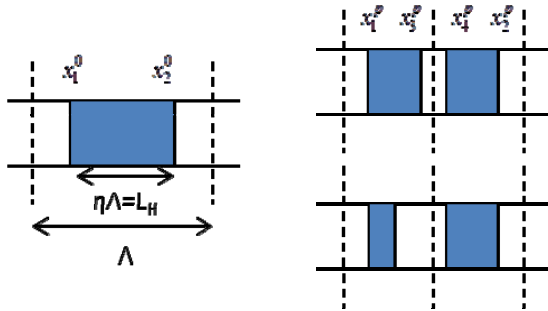


Figure 5. HCG with a symmetrically and an asymmetrically perturbed structure with high index bars on both sides of the center. The unit cell is normalized and the refractive index profile for the transition points between 0 and 1 is depicted.

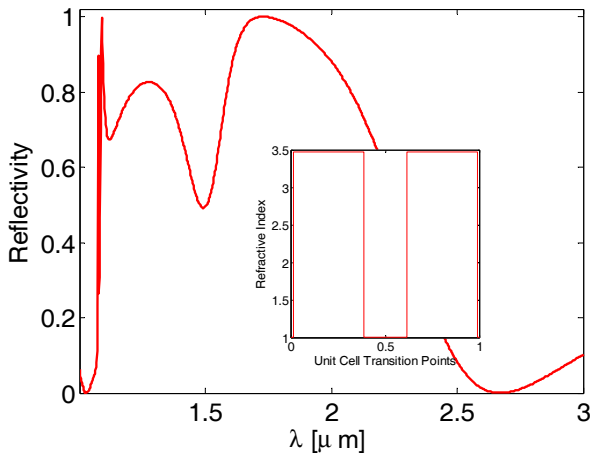


Figure 6. Reflectivity of the HCG with the period  $\Lambda=0.77 \mu\text{m}$ , duty cycle  $\eta=0.75$ , height  $t_g=0.48 \mu\text{m}$ , high index material  $n_g=3.48$  (Si) and low index material  $n_0=1$  and a symmetrically perturbed structure with high index bars on both sides of the center and for a relative shift  $p=0.15$ . The refractive index distribution in the unit cell is shown in the inset.

We consider a HCG with a period  $\Lambda=0.77 \mu\text{m}$ , duty cycle  $\eta=0.75$ , height  $t_g=0.48 \mu\text{m}$ , high index material  $n_g=3.48$  (Si) and low index material  $n_0=1$ . The reflectivity of the symmetrically perturbed structure is shown in Figure 6: the central high-index region is symmetrically split into 2 parts and moved outwards from the center of the unit cell. The reflectivity is deformed but resonances or similar spectral features are not present in the regions of broadband reflectivity.

The reflectivity of the asymmetrically perturbed structure is shown in Figure 7: the central high index region is symmetrically split into 2 parts and moved outwards from center of the unit cell in asymmetric fashion. High reflectivity is preserved under perturbation, but a resonance appears in the regions of the previously broadband high reflectivity. These very sharp resonances appear even with very small perturbations of the structure. Figure 8 shows a close-up of the reflection resonance and refractive index distribution with the  $p=0.15$ .

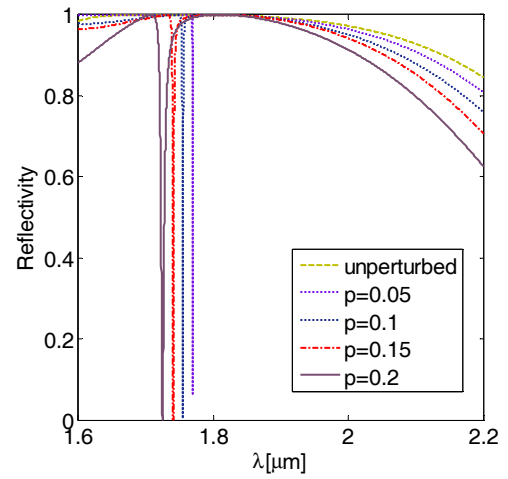


Figure 7 Reflectivity of the HCG with a period  $\Lambda=0.77 \mu\text{m}$ , duty cycle  $\eta=0.75$ , height  $t_g=0.48 \mu\text{m}$ , high index material  $n_g=3.48$  (Si) and low index material  $n_0=1$  and asymmetrically perturbed structure with high index bars on both sides of the center and for different relative shift parameters.

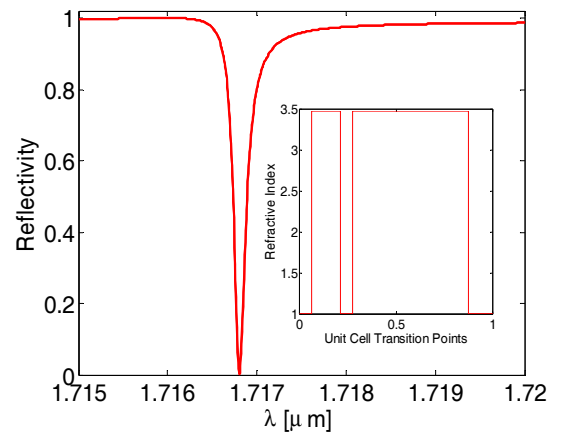


Figure 8 Reflectivity of the HCG with a period  $\Lambda=0.77 \mu\text{m}$ , duty cycle  $\eta=0.75$ , height  $t_g=0.48 \mu\text{m}$ , high index material  $n_g=3.48$  (Si) and low index material  $n_0=1$  and asymmetrically perturbed structure with parameter  $p=0.15$ . Refractive index distribution is shown in the inset.

The comparison of the spectral response for symmetrically and asymmetrically perturbed structures, like those in Figures 6 and 7, suggests that the spectral response is robust under symmetric unit cell perturbations, while asymmetric unit cell perturbations introduce a new spectral response. In our previous work we showed the examples of highly fragmented spectra present in the case of HCGs with the aperiodic topology in the unit cell [19]. Furthermore, we showed that the systematic use of an aperiodic design of the unit cell enables control of the number of spectral resonances and the symmetry of the fields in the prescribed spectral band [20]. A similar phenomenology related to resonances has been observed in the spectral response of photonic crystals with an aperiodic or defect-based structure [25], [26], [27]. The mechanism responsible for the excitation of these resonances relies on symmetry breaking due to perturbation that opens coupling of the incident wave into the transmitted channel.

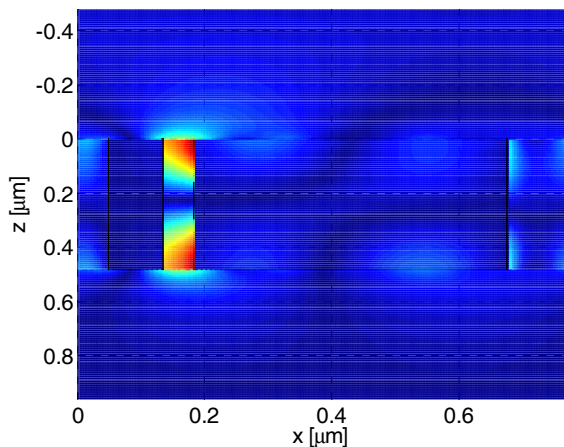


Figure 9 Field distribution at resonance wavelength of  $1.716 \mu\text{m}$  for HCG with the period  $\Lambda=0.77 \mu\text{m}$ , duty cycle  $\eta=0.75$ , height  $t_g=0.48 \mu\text{m}$ , high index material  $n_g=3.48$  (Si) and low index material  $n_0=1$  and asymmetrically perturbed structure with parameter  $p=0.15$ .

The field distribution of the leading field component (TM polarization) in the unit cell at the resonance of  $1.716 \mu\text{m}$  is shown in Figure 10. Owing to asymmetry of the unit cell the field distribution is also asymmetric, while showing interesting strong localization in the low index region between two high index bars and with the negligible penetration in the high index material. Hence, field concentration in the region of free space between high index bars makes it accessible for local probing. This is potentially interesting for sensing applications [28]. Beside the reflectivity magnitude, the phase response plays an important role in some devices such as planar focusing mirrors and optical phased arrays described in Section 4. The asymmetric design of the unit cell leads to the appearance of many resonances in the spectral reflection magnitude and phase, as seen in Figure 10.

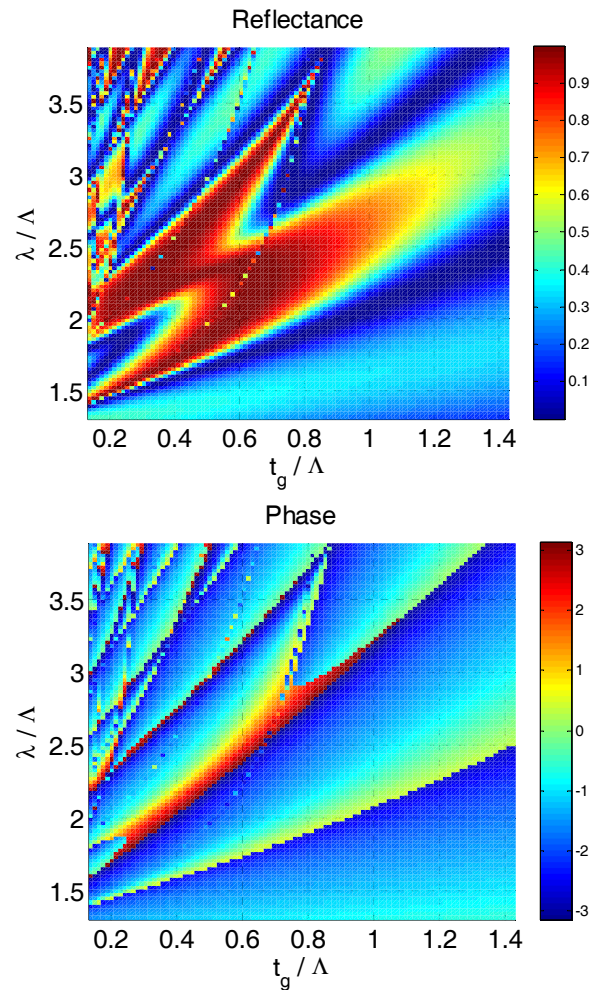


Figure 10 Reflection and phase response of the HCG structure at the wavelength of  $1.716 \mu\text{m}$  with a varying duty cycle for a fixed period  $\Lambda=0.77 \mu\text{m}$ , high index material  $n_g=3.48$  (Si). The asymmetric unit cell structure is the same as in Figure 8.

#### IV. MEMS MIRRORS WITH SUB-WAVELENGTH HCGS

##### A. Planar focusing mirrors using non-periodic HCGs

An HCG can be designed to function as an ultrathin planar lens and focusing reflector [1], [8]. This design requires a non-periodic, chirped (sub-wavelength) grating structure enabling control of the reflected beam phase, without changing the high reflectivity of the mirror

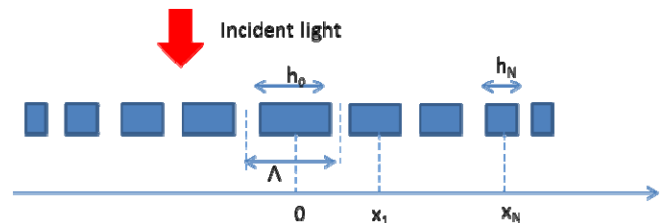


Figure 11 Sketch of the chirped grating structure defining a planar HCG element with spatially varying phase response. The local width of the high index bar is changed within a single unit cell

A design approach is to use scaling of the HCG parameters to shift the desired reflection response at a specified wavelength by scaling the geometrical parameters of the grating. Hence, if the grating has a particular complex reflection coefficient  $\mathbf{r}_0$  at a vacuum wavelength  $\lambda_0$ , then a new grating structure with the same reflection coefficient at the wavelength  $\lambda$  scales by the factor  $s = \lambda/\lambda_0$ , giving  $\mathbf{r}(\lambda) = \mathbf{r}_0(\lambda/s) = \mathbf{r}_0(\lambda_0)$ . Further, the reflection properties of HCGs depend mostly on the local geometry around a specific spatial location. Hence, the non-uniform scaling of the reference grating will lead to local adjustment of the reflection phase while maintaining a large reflectivity at the specified wavelength, see the sketch in Figure 10. If the phase at a certain spatial coordinate is  $\varphi(x,y)$  and the non-uniform grating has a slowly varying spatial scale  $s(x,y)$ , the reflection response is the same as for a periodic structure with reflection  $\mathbf{r}_0(\lambda) = \mathbf{r}_0(\lambda/s(x,y))$ . In the simplest design approach the base period may be kept constant and only the duty cycle can be changed provided that the phase response is sufficiently variable. A more complex design may use a variation of the base period and also the adjustment of the local thickness of the high index bar. Hence, an algorithm to choose local grating parameters so that the desired phase is reached may be possible using calculation of periodic structures.

The phase variation along the x-axis impressed upon reflected light incident on the chirped grating may lead to strong focusing effect if the phase variation is of the following form:

$$\varphi(x) = \frac{2\pi}{\lambda} \left( f + \frac{\varphi_{\max}}{2\pi} \lambda - \sqrt{x^2 + f^2} \right), \quad (11)$$

where  $f$  is the focal length and  $\varphi_{\max}$  is the maximum phase change between the middle and the edge of the grating. The continuous phase distribution presented by expression (11) is approximated with the discrete phase distribution defined by the chirped grating.

### B. Optical phased arrays using HCGs.

Recently it has been demonstrated that a MEMS mirror with the HCG grating can be used as a phase-tuning element which passively transmits or reflects the incoming light while modifying its phase [1], [9]. A simple architecture of a MEMS-based phase tuner can be realized by a ‘‘piston’’ mirror approach whereby a mirror is displaced to provide the desired phase shift of reflected light. A sketch of a typical design of the phase tuning element is shown in Figure 12. A high contrast grating mirror is placed in the square frame suspended from thin flexure springs that allow for grating movement. The substrate incorporates (usually) a distributed Bragg reflector (DBR) or possibly a metal mirror. The mirror can be actuated by applying voltage between the contacts at each mirror.

Finally, an array of individually addressable mirrors forms an optical phased array that enables beam steering. The reflection  $r$  and the phase of an individual phase tuning element can be simplistically modeled as:

$$r = e^{i\varphi_{HCG}} \frac{|r_{HCG}| - |r_{DBR}| e^{2i\varphi}}{1 - |r_{HCG}| |r_{DBR}| e^{2i\varphi}} = |r| e^{i\Phi}, \quad (12)$$

where the roundtrip phase is

$$2\varphi = \varphi_{HCG} + \varphi_{DBR} + 2\pi \frac{2(d_0 - \Delta d)}{\lambda}, \quad (13)$$

and the resulting phase shift is

$$\Phi = \varphi_{HCG} + 2 \operatorname{atan} \left( \frac{1 + \sqrt{R_{HCG}}}{1 - \sqrt{R_{HCG}}} \tan \varphi \right) + \pi + 2\pi \frac{2\Delta d}{\lambda}. \quad (14)$$

This model takes into account that the HCG mirror is moving and the substrate is stationary. In practice, the total phase shift is usually less than  $2\pi$  and the reflectance is less than ideal. However, the range of phase element tuning can be addressed additionally with the asymmetric unit cell design. This is due to the fact that phase response is also influenced by resonance induced with the asymmetric unit cell design similar to those discussed in Section 3.

The above design is essentially an all-pass filter (APF) realized as an asymmetric Fabry-Perot (FP) resonator with a carefully designed reflectivity of the top and bottom mirror. When actuating the top mirror to tune the length of the FP resonator across its FP resonance, the reflection phase of the incident light normal to the surface experiences a continuous phase change approaching  $2\pi$ , while the reflection magnitude is close to unity. The speed of optical phase tuning depends on the mechanical resonance frequency of the HCG MEMS mirror and it allows for very high speed operation owing to the small mass of the HCG compared to other solutions such as DBR mirror. Actual beam steering in the far-field is achieved by creating the desired near-field phase front of the reflected beam on the whole array. Hence, a chip-scale, high-speed, high-integration-density, small-footprint, low-power-consumption operation of this optical phased array is of interest in many applications such as optical circuit switching, light detection and ranging (LIDAR), imaging, sensing, precision targeting etc.

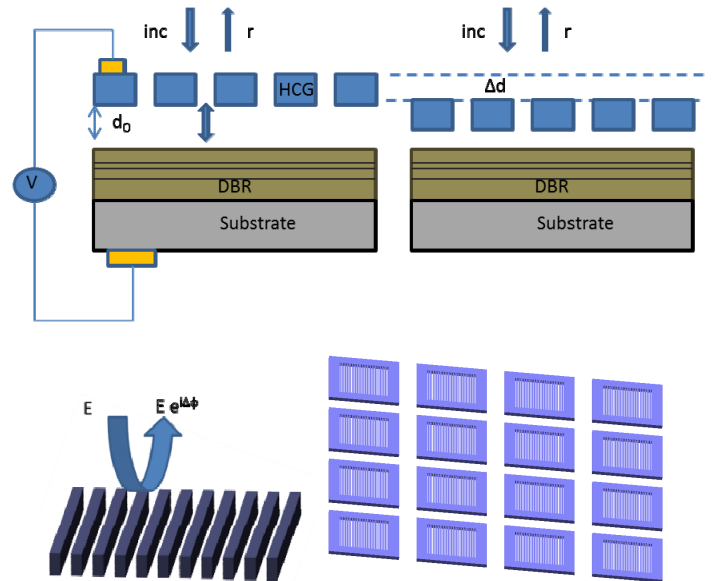


Figure 12 Sketch of a single phase tuning element and a MEMS mirrors array with HCGs for optical phase control.

## V. CONCLUSIONS

High-contrast gratings (HCG) are important structures in integrated opto-electronics enabled by recent developments in MEMS technology. We showed that the spectral response of HCGs can be tailored via the unit cell perturbations. More specifically, we demonstrated that an asymmetric design of unit cell leads to the appearance of specifically located spectral resonances. We showed that both the magnitude and the phase response are influenced by this asymmetric design. Our results can serve as a guidance for the design of complex HCGs and help with the choice of the efficient initial grating topology prior to global optimization procedure. In addition, they may open more freedom in tailoring amplitude and phase response of the HCG mirrors for specific applications such as high-Q resonance filters, planar focusing elements, beam steering optical phased arrays, etc.

## REFERENCES

- [1] C. J. Chang-Hasnain and W. Yang, "High-contrast gratings for integrated optoelectronics", *Advances in Optics and Photonics* 4, 379–440 (2012).
- [2] Y. Rao, W. Yang, C. Chase, M. C. Huang, D. P. Worland, S. Khaleghi, M. R. Chitgarha, M. Ziyadi, A. E. Willner, C. J. Chang-Hasnain, "Long-wavelength VCSEL using high-contrast grating," *IEEE J. Sel. Top. Quantum Electron.* 19, 1701311 (2013)
- [3] Y. Zhou, M. Moewe, J. Kern, M. C. Y. Huang, C. J. Chang-Hasnain, "Surface-normal emission of a high-Q resonator using a subwavelength high-contrast grating," *Opt. Express* 16(22), 17282–17287 (2008).
- [4] A. Ricciardi, S. Campopiano, A. Cusano, T. F. Krauss, L. O'Faolain, "Broadband mirrors in the near-infrared based on subwavelength gratings in SOI." *IEEE Photonics Journal*, 2(5): 696-702, (2010)
- [5] Y. Wang, D. Stellinga, A. B. Klemm, C. P. Reardon, T. F. Krauss, "Tunable Optical Filters Based on Silicon Nitride High Contrast Gratings." *IEEE Journal of Selected Topics in Quantum Electronics*, vol. 21, no. 4, 1-6, (2015)
- [6] K. Ikeda, K. Takeuchi, K. Takayose, I.-S. Chung, J. Mørk, H. Kawaguchi, "Polarization-independent high-index contrast grating and its fabrication tolerances," *Appl. Opt.* 52, 1049-1053 (2013).
- [7] Y. Zhou, V. Karagodsky, B. Pesala, F. G. Sedgwick, C. J. Chang-Hasnain, "A novel ultra-low loss hollow-core waveguide using subwavelength high-contrast gratings," *Optics Express* 17.3:1508-1517, (2009)
- [8] D. Fattal, J. Li, Z. Peng, M. Fiorentino, and R. G. Beausolei, "Flat dielectric grating reflectors with focusing abilities," *Nat. Photonics* 4(7), 466–470 (2010).
- [9] B.-W. Yoo, M. Megens, T. Chan, T. Sun, W. Yang, C.J. Chang-Hasnain, D.A. Horsley, M.C. Wu, "Optical phased array using high contrast gratings for two dimensional beam forming and beam steering." *Optics Express* 21.10,12238-12248, (2013)
- [10] E. Popov, editor, *Gratings: Theory and Numeric Applications*, Institut Fresnel, CNRS, AMU, 2012
- [11] M. Moharam, E. Grann, D. Pommet, and T. Gaylord, "Formulation for stable and efficient implementation of the rigorous coupled-wave analysis of binary gratings," *J. Opt. Soc. Am. A* 12, 1068-1076 (1995)
- [12] P. Lalanne, J.P. Hugonin, P. Chavel, "Optical properties of deep lamellar Gratings: A coupled Bloch-mode insight," *IEEE Journal of Lightwave Technology*, vol.24, no.6, (2006)
- [13] V. Karagodsky, F. Sedgwick, and C. Chang-Hasnain, "Theoretical analysis of sub-wavelength high contrast grating reflectors," *Opt. Express* 18, 16973-16988 (2010).
- [14] V. Karagodsky and C. Chang-Hasnain, "Physics of near-wavelength high contrast gratings," *Opt. Express* 20, 10888-10895 (2012).
- [15] A. Ahmed, M. Liscidini, R. Gordon, "Design and Analysis of High-Index-Contrast Gratings Using Coupled Mode Theory," *IEEE Photonics Journal*, vol.2, no.6, pp.884-893, (2010)
- [16] W. Yang, C. J. Chang-Hasnain, "Physics of high contrast gratings: a band diagram insight", *Proc. SPIE* 863303 (2013)
- [17] O. Solgaard, A.A. Godil, R.T. Howe, L.P. Lee, Y.-A. Peter, H. Zappe, "Optical MEMS: From micromirrors to complex systems.", *IEEE Journal of Microelectromechanical Systems*, vol. 23 no. 3, 517-538, (2014)
- [18] H. Zappe, "Micro-optics: A micro tutorial," *Adv. Opt. Technol.*, vol. 1, no. 3, pp. 117–126, 2012
- [19] M. Maksimović, "Modeling and optimization of high index contrast gratings with aperiodic topologies", *Proceedings of SPIE Vol. 8789, 87890L* (2013)
- [20] M. Maksimović, "Resonances in high-contrast gratings with complex unit cell topology", *International Workshop on Optical Waveguide Theory and Numerical Modeling (OWTNM 2013)*, Enschede, The Netherlands, proceedings paper O-1.2, (2013)
- [21] C. Chevallier, F. Genty, N. Fressengeas, J. Jacquet, "Robust Design by Antioptimization for Parameter Tolerant GaAs/AIO<sub>x</sub> High Contrast Grating Mirror for VCSEL Application." *Journal of Lightwave Technology*, vol. 31, no. 21 3374-3380, (2013)
- [22] E. Maciá, *Aperiodic Structures in Condensed Matter: Fundamentals and Applications*, CRC Press, (2009)
- [23] L. Dal Negro and S.V. Boriskina, "Deterministic aperiodic nanostructures for photonics and plasmonics applications", *Laser Photonics Rev.*, 1–41 (2011)
- [24] Maksim Skorobogatiy and Jianke Yang, *Fundamentals Of Photonic Crystal Guiding*, Cambridge University Press, 2009
- [25] O. Kiliç, M. Digonnet, G. Kino, and O. Solgaard, "Controlling uncoupled resonances in photonic crystals through breaking the mirror symmetry," *Opt. Express* 16, 13090-13103 (2008).
- [26] I. Gallina, M. Pisco, A. Ricciardi, S. Campopiano, G. Castaldi, A. Cusano, and V. Galdi, "Guided resonances in photonic crystals with point-defected aperiodically-ordered supercells," *Opt. Express* 17, 19586-19598 (2009).
- [27] M. Maksimović, M. Hammer and E. W. C. van Groesen, "Coupled optical defect micro-cavities in one-dimensional photonic crystals and quasi-normal modes", *Opt. Eng.* 47(11), 114601, (2008)
- [28] Z. Jakšić, *Micro and Nanophotonics for Semiconductor Infrared Detectors: Towards an Ultimate Uncooled Device*, Springer, 2014

# Joint Effect of Heterogeneous Intrinsic Noise Sources on Instability of MEMS Resonators

Olga Jakšić, Ivana Jokić, Miloš Frantlović, Danijela Randjelović, Dragan Tanasković, Žarko Lazić and Dana Vasiljević-Radović

**Abstract**—This article's focus is on the numerical estimation of the overall instability of microelectromechanical-system-based (MEMS) resonators, caused by intrinsic noise mechanisms that are different in nature (electrical, mechanical or chemical). Heterogeneous intrinsic noise sources in MEMS resonators that have been addressed here are Johnson–Nyquist noise,  $1/f$  noise, noise caused by temperature fluctuations and adsorption-desorption induced noise. Their models are given first (based on analytical modeling or based on empirical expressions with experimentally obtained parameters). Then it is shown how each one contributes to the phase noise, a unique figure of merit of resonators instability. Material dependent constants  $\alpha$  and knee position in noise spectrum, needed for empirical formulae referring to  $1/f$  noise, have been obtained experimentally, by measurements of noise of MEMS components produced in the Centre of Microelectronic Technologies of the Institute of Chemistry, Technology and Metallurgy in Belgrade. According to these measurements,  $\alpha$  varies in the range from  $0.776 \cdot 10^{-4}$  to  $2.26 \cdot 10^{-4}$  and cut off frequency for  $1/f$  noise varies from 147 Hz to 1 kHz. The determined values are then used for the modeling of micro-resonator phase noise with electrical origin and overall phase noise of a micro-resonator. Numerical example for calculation of overall phase noise is given for a micro-cantilever, produced by the same technology as measured components. The outlined noise analysis can be easily extended and applied to noise analysis of MEMS resonator of an arbitrary shape.

**Index Terms**— $1/f$  noise, adsorption, desorption, temperature fluctuations, intrinsic noise, Johnson noise, micro cantilever, Nyquist noise, phase noise, power spectral density, thermal noise, thermo-mechanical noise, white noise.

*Original Research Paper*  
DOI: 10.7251/ELSI1519059J

## I. INTRODUCTION

THE importance of “micro-electro-mechanical-systems” i.e. MEMS and “micro-opto-electro-mechanical-systems” i.e. MOEMS devices grows over time in many fields.

Manuscript received 08 November 2015. Received in revised form 15 December 2015.

This work has been supported by the Serbian Ministry of Education and Science through the project TR 32008.

O. M. Jakšić, Ivana Jokić, Miloš Frantlović, Danijela Randjelović, Dragan Tanasković, Žarko Lazić and Dana Vasiljević-Radović are with the Centre of Microelectronic Technologies, Institute of Chemistry, Technology and Metallurgy, University of Belgrade, Belgrade, Serbia (corresponding author: Olga Jakšić phone: +381-11-262-8587; fax: +381-11-2182-995; e-mail: olga@nanosys.ihtm.bg.ac.rs).

Miniaturization of components, enabled by nanotechnologies, ensured further integration of oscillators with ever smaller passive components and other functional blocks. As a consequence, we have lower power consumption but also tunability, new functionalities [1] and better overall performances of many devices: new nano-resonators can have their fundamental resonance frequency of over 10 MHz [2] and a quality factor reaching  $2 \cdot 10^4$  [3], new ultrathin silicon cantilevers can detect attonewton forces [4] and new sensors ensure mass detection of a single molecule [5]. Limiting performances of these devices are governed by intrinsic noise sources [6] (assuming extrinsic noise sources are suppressed by shielding and other noise reduction techniques [7]).

The mechanisms of intrinsic noise in MEMS and NEMS (“nano-electro-mechanical-systems”) devices are diverse. They differ in physical nature, in magnitude, in mathematical approach suitable for their modeling, they behave differently with scaling and the balance between extrinsic and intrinsic noise becomes also different with scaling (in an integrated circuit all noise mechanisms of its constituent parts are intrinsic). They all contribute to the same output signal, and it is important to know how the joint effect of all of them determines limiting performances and also how it affects device's optimization and characterization.

The often met constituent parts in MEMS and NEMS devices are resonant structures: cantilevers, beams, membranes and “comb-like” structures. In this work we consider the cantilever as the basic part.

This paper focuses on the theoretical modeling of intrinsic noise sources of a micro-cantilever with the piezo-resistive read-out and presents experimental determination of technology-dependent parameters appearing in theoretical models. The second section addresses fluctuations in different domains: the electrical noise induced by fluctuations in movement of free carriers, Johnson-Nyquist and  $1/f$  noise, noise caused by temperature fluctuations, noise induced by fluctuations in mechanical displacement of moving parts in a MEMS resonator and noise induced by resonator's mass fluctuations due to adsorption-desorption processes. This is followed by a section addressing the phase noise, a unique figure of merit for the estimation of the resonator instability where the connection of heterogeneous intrinsic noise mechanisms with phase noise is given. The paper finally considers the application of the outlined theory.

## II. THEORY

### A. Thermal noise

Thermal noise is an intrinsic noise mechanism that exists in all MEMS devices with electrical parts, or to be more precise in all MEMS devices with free carriers and an electrical read-out. Even if there were no current flowing through the device, if there is an electrical read-out, the output voltage would be the consequence of the thermal motion of free carriers.

Thermal noise was first studied experimentally in 1928 by John B. Johnson [8] at Bell Telephone Laboratories. Analytical explanations of Johnson's experiments from a thermodynamical point of view were given by his colleague Harry Nyquist [9], also at Bell Telephone Laboratories. Thus thermal noise is often called Johnson noise, Nyquist noise or Johnson-Nyquist noise.

According to Nyquist theory, the power spectral density of voltage fluctuations ( $S_{VJ}$ ) stems from thermal agitation of electric charges in MEMS resistors whose resistance is  $R$ , at temperature  $T$  and frequency  $f$ . It is proportional to the quadruple product of that resistance and the total energy per each degree of freedom:

$$S_{VJ} = 4R \frac{hf}{e^{hf/k_B T} - 1} \left( V^2 / \text{Hz} \right). \quad (1)$$

where  $h$  is Plank constant and  $k_B$  is Boltzmann constant.

Based on the fluctuation-dissipation theorem developed by Callen and Welton [10] in 1951, the Nyquist theorem may be generalized. An electrical circuit is a linear system and the same formula is valid for an arbitrary electrical circuit with an impedance  $Z$ , and in that case the real part of  $Z$  is put in the expression (1) instead of  $R$ . In practical applications where the total energy per degree of freedom may be considered constant (equal to  $k_B T$ ) within specified ranges of frequency and temperature, the following formula is valid:

$$S_{VJ} = 4k_B T \text{Re}\{Z\} \left( V^2 / \text{Hz} \right). \quad (2)$$

In case of a pure resistor, this equation leads to a flat power spectrum, so thermal noise is also known as a white noise.

### B. $1/f$ Noise

Prior to his famous work on experimental observations of thermal noise published in *Physics Review* in 1928 [8], Johnson wrote a letter to *Nature* [11] where he commented on voltage fluctuations that “appears to be the result of thermal agitation of the electric charges in the material of the conductor”. In that letter, he also commented on fluctuations that depend not on temperature but inversely on frequency — so we may say today that Johnson had discovered electrical ' $1/f$  noise' known also as flicker or pink noise. Flicker noise has remained the topic of active theoretical and experimental research till today [12]. The overall agreement is that, contrary to thermal noise, flicker noise is a non-equilibrium phenomenon, it appears in the presence of polarization in electrical circuits. Its probable cause is assumed to be scattering of free carriers during the transport through

conducting material [13]. In this paper, we describe the power spectral density of voltage fluctuations induced by flicker noise by the empirical expression introduced by F. N. Hooge [14]:

$$S_{VH} = \frac{\alpha V_B^2}{Nf} \left( V^2 / \text{Hz} \right) \quad (3)$$

where  $V_B$  stands for the bias of the electrical circuit,  $f$  is frequency,  $N$  is the number of free carriers and alpha is a material-dependent constant that has to be determined experimentally. According to [15], alpha ranges from  $10^{-3}$  to  $10^{-7}$ , depending on the material.

### C. Temperature Fluctuations-Induced Noise

Noise induced by temperature fluctuations is another example of how the fluctuation-dissipation theorem can be applied to any linear dissipative system in thermodynamic equilibrium. According to derivations outlined in [16], [17], the expression for the power spectral density of temperature fluctuations is:

$$S_{\Delta T} = \frac{4k_B T^2 G_{th}}{(G_{th}^2 + 4\pi^2 f^2 C_{th}^2)} \left( K^2 / \text{Hz} \right). \quad (4)$$

Here  $C_{th}$  is the heat capacity calculated as a product of the specific heat and the volume of the observed structure and  $G_{th}$  stands for thermal conductivity which is calculated using the Steffan-Boltzmann law. The power spectral density of this noise is Lorentzian, its typical shape being shown in Fig. 1.

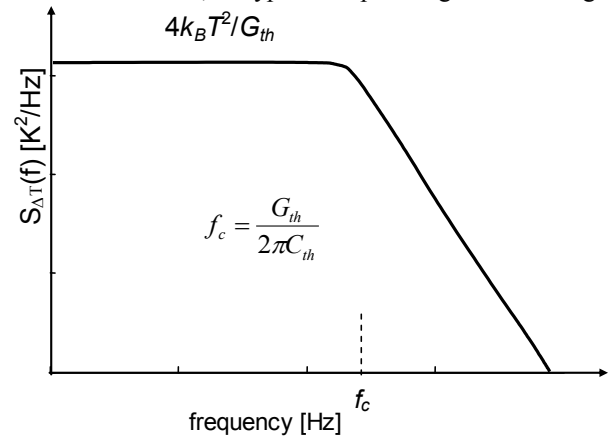


Fig. 1. Power spectral density of temperature fluctuations in a microstructure with a thermal conductivity  $G_{th}$  and a heat capacity  $C_{th}$ .

### D. Thermo-mechanical Noise

Thermo-mechanical noise is a consequence of mechanisms of energy transfer between the structure of a mechanical resonator and its surroundings in equilibrium. The detailed derivation outlined in [18] and in literature stated therein leads to the following expression for the power spectral density of the displacement fluctuations of a micro-resonator:

$$S_X = \frac{4k_B T k}{Q\omega_0} \frac{1/m_r^2}{(\omega_0^2 - 4\pi^2 f^2)^2 + \left( \frac{\omega_0 2\pi f}{Q} \right)^2} \left( m^2 / \text{Hz} \right). \quad (5)$$

$Q$  is quality factor,  $m_r$  is the resonators mass,  $k$  is the

resonator stiffness constant, and  $\omega_0$  the resonant angular frequency. The meaning of other terms is the same as above. A typical spectrum is shown in Fig. 2.

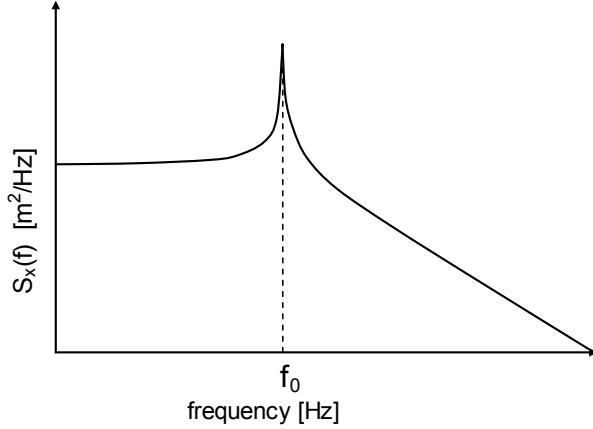


Fig. 2. Power spectral density of displacement fluctuations in a micro-resonator with a resonant frequency  $f_0$ .

### E. Adsorption-desorption Induced Noise

The last important intrinsic noise source considered here is the adsorption-desorption noise. It is a mass fluctuation-induced noise and its importance grows as the resonator dimensions scale down so it may, under some conditions, be the dominant noise mechanism in a micro-resonator. It has been first observed by Yong and Vig [19]. In 2002, based on an analogy between adsorption-desorption processes of molecules on a solid surface and generation-recombination processes of charge carriers in a semiconductor, Djurić et al developed the first mathematical model of the power spectral density of mass fluctuations caused by monolayer monocomponent adsorption of surrounding gas molecules on the resonator surface [20]:

$$S_{\Delta m} = \frac{4M_a^2 C_2 N_m b p A}{C_2^2 (b p + 1)^3 + 4\pi^2 f^2 (b p + 1)} \left( \frac{\text{kg}^2}{\text{Hz}} \right). \quad (6)$$

Here  $M_a$  is the mass of a gas molecule,  $C_2$  is the constant inversely proportional to the mean residential time of adsorbed molecules on the surface,  $N_m$  is the maximal number of adsorption sites on the surface,  $A$  is the resonator surface area,  $p$  is pressure and  $b$  is calculated as

$$b = \frac{\alpha_s \tau \cdot 3.513 \cdot 10^{22}}{N_m \sqrt{M_a T}} \quad (7)$$

Expression (7) is valid if pressure is given in Torr, and  $\alpha_s$  here is the sticking coefficient representing the affinity of gas molecules towards the surface and  $\tau$  is the mean residential time of adsorbed gas molecules on the resonator surface.

Typical spectrum for power spectral density of resonator mass fluctuations caused by adsorption-desorption noise has a Lorentzian shape. It is shown in Fig 3.

The model of bi-component monolayer adsorption-induced micro-cantilever mass fluctuations is developed in [21], and Fig 4 shows the typical spectrum where one can distinguish two knees suitable for noise spectroscopy.

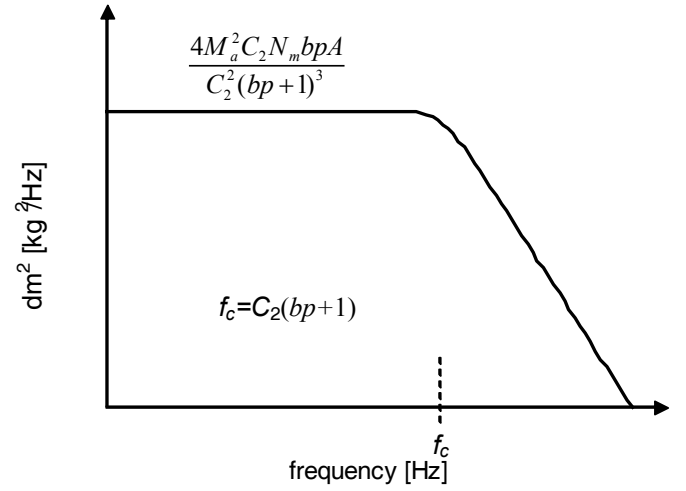


Fig. 3. Power spectral density of resonator mass fluctuations caused by nanocomponent monolayer adsorption of surrounding gas on resonator surface.

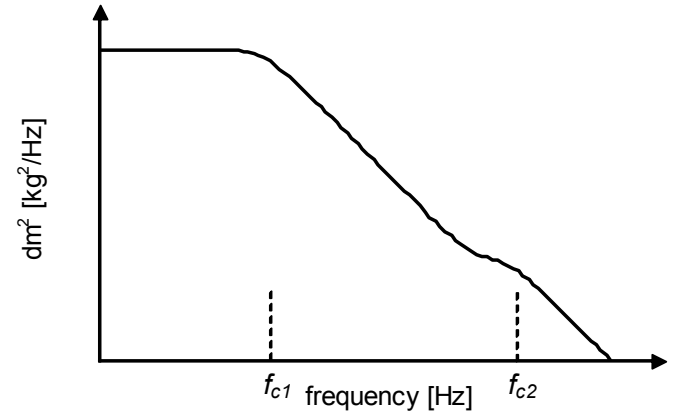


Fig. 4. Power spectral density of resonator mass fluctuations caused by bicomponent monolayer adsorption of surrounding gas on resonator surface.

### III. PHASE NOISE

The figure of merit for the quality of a micro-resonator is its phase noise. The definition, based on the double-sideband power spectral density of phase fluctuations  $S_\phi$ , is given by the standard IEEE 1139 (IEEE Standard Definitions of Physical Quantities for Fundamental Frequency and Time Metrology—Random Instabilities) [22]:

$$L(f) = \frac{1}{2} S_\phi(f) \quad (8)$$

The overall power spectral density of phase fluctuations of a micro-resonator is calculated as a sum of all power spectral densities of phase fluctuations calculated for every particular intrinsic noise mechanism separately. After summing, the result is often given in decibels:

$$L(f) = 10 \log \left( \frac{1}{2} S_\phi(f) \right) \quad (9)$$

Here  $f$  is, just as in theory of phase noise in electrical oscillators [23], the distance (along the frequency axis) from the resonant frequency, as shown in Fig. 5.

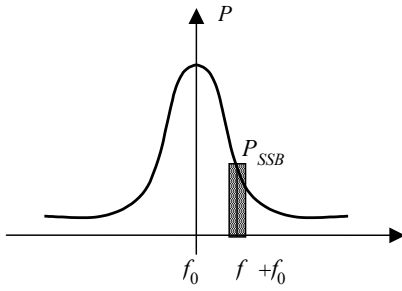


Fig. 5. Power spectral density of an electrical oscillator. Phase noise is defined as the ratio of  $P_{SSB}$  (the single-sided power emitted at the frequency  $f$  from a resonant frequency  $f_0$  in a bandwidth of 1 Hz) and  $P$  (the overall power emitted when the oscillator is in its resonant mode).

Only after establishing the connection of heterogeneous fluctuations caused by different mechanisms of intrinsic noise with the power spectral density of phase fluctuations it is possible to find their joint effect on micro-resonator stability.

#### A. Phase Noise Induced by Voltage Fluctuations

Voltage fluctuations in micro-mechanical resonators with electrical read-out may be treated according to the theory of electrical oscillators. The modeling of connection between voltage fluctuations due to thermal and flicker noise and phase fluctuations in electrical oscillators is empirically established by Leeson [24]. According to Leeson, phase noise in oscillators has two origins: up-conversion of electrical noise (flicker and Johnsons) to the high-frequency region around the resonant frequency and phase fluctuations that modulate the resonant frequency. Their effect on phase fluctuations of an oscillator depends on the resonant frequency  $f_0$  and the quality factor  $Q_L$  (index  $L$  refers to a closed loop):

$$\begin{aligned} S_{\phi Osc}(f) &= S_{\phi Amp} \left( 1 + \left( \frac{f_0}{2fQ_L} \right)^2 \right) = \frac{S_V(f)}{P_0} \left( 1 + \left( \frac{f_0}{2fQ_L} \right)^2 \right) \\ &= \frac{S_{VJ}}{P_0} \left( 1 + \frac{f_c}{f} \right) \left( 1 + \left( \frac{f_0}{2fQ_L} \right)^2 \right) \end{aligned} \quad (10)$$

An oscillator is attained as an amplifier in a frequency selective closed loop and the connection between phase fluctuations of an amplifier  $S_{\phi Amp}$  and voltage fluctuations  $S_V$  is  $P_0$ , the power of the signal at the resonant frequency.

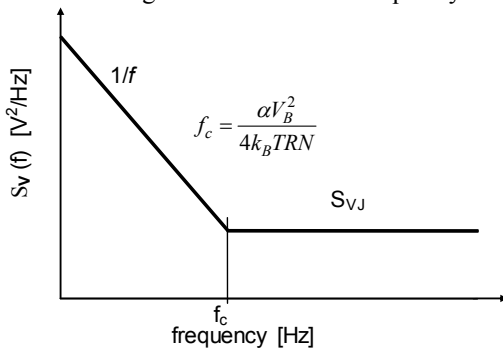


Fig. 6. Thermal and flicker noise before up-conversion to region around resonant frequency

In a micromechanical resonator voltage fluctuations have the same form: spectrum produced by the calculation of

thermal and  $1/f$  noise using (1) or (2) and (3) is given in Fig. 6 and has the same form of a spectrum of an amplifier in an open loop  $S_{\phi Amp}$  used in (10). The connection between the phase fluctuations and the phase fluctuations in a mechanical microresonator is done by taking into account the displacement fluctuations.

Here we consider the piezoresistive read-out made by a Wheatstone bridge where one of four identical resistors is placed on the moving resonating part of a cantilever and all three other resistors are placed on the steady base of a cantilever. The output voltage equals one quarter of the product of the bias voltage  $V_B$ , displacement  $X$  and cantilevers voltage sensitivity to displacement  $S$ . In [26] Cleland and Roukes showed that the power spectral density of phase fluctuations equals the power spectral density of the displacement fluctuations divided by the mean square amplitude of oscillations  $\langle X_0^2 \rangle$ .

Phase noise in microresonator due to thermal and flicker noise is then

$$\begin{aligned} S_{\phi\{V\}}(f) &= S_{\phi}(S_{\Delta X}(S_V)) \left( 1 + \left( \frac{f_0}{2fQ_L} \right)^2 \right) \\ &= S_{\phi} \left( \frac{16S_V}{S^2V_B^2} \right) \left( 1 + \left( \frac{f_0}{2fQ_L} \right)^2 \right) = \frac{16S_V}{\langle X_0^2 \rangle S^2V_B^2} \left( 1 + \left( \frac{f_0}{2fQ_L} \right)^2 \right) \\ &= \frac{16S_{VJ}}{\langle X_0^2 \rangle S^2V_B^2} \left( 1 + \frac{f_c}{f} \right) \left( 1 + \left( \frac{f_0}{2fQ_L} \right)^2 \right) \end{aligned} \quad (11)$$

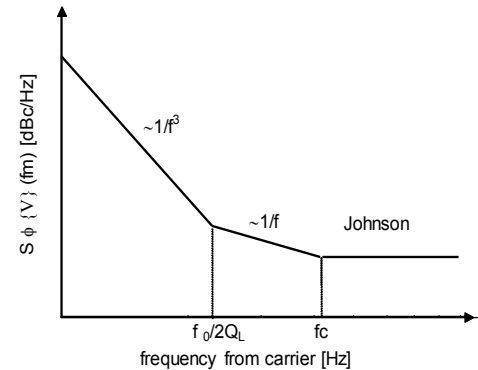


Fig. 7. Power spectral density of phase fluctuations for an oscillator with a high quality factor

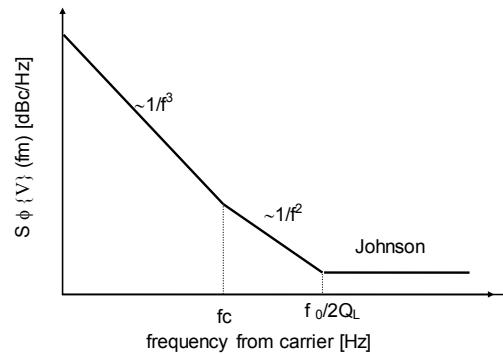


Fig. 8. Power spectral density of phase fluctuations for an oscillator with a low quality factor

In general the spectrum has a shape like that in Fig. 7 or Fig 8. depending on the values for  $f_c$  and  $f_0/(2Q_L)$ .

Oscillators with a low quality factor have the diagram as shown in Fig. 8 where the first knee corresponds to  $f_c$  and the second to  $f_0/(2Q_L)$ . The knee positions are reversed for oscillators with high quality factors. In both cases, in order to apply (11) the knee position must be determined experimentally or estimated based on good knowledge of material properties.

### B. Phase Noise Induced by Temperature Fluctuations

According to reasoning by Vig in [25], fluctuations of the normalized frequency of the resonator are proportional to fluctuations in temperature with a factor of proportionality  $\alpha_T$ , so the power spectral densities of these fluctuations relate as:

$$S_{y\{\Delta T\}}(f) = \alpha_T^2 S_{\Delta T}(f) \quad (12)$$

The power spectral density of resonator phase fluctuations induced by fluctuations in temperature is then

$$S_{\phi\{\Delta T\}}(f) = \frac{f_0^2}{f^2} S_{y\{\Delta T\}}(f) = \frac{f_0^2}{f^2} \alpha_T^2 S_{\Delta T}(f) \quad (13)$$

Notation is as stated before.

### C. Phase Noise Induced by Displacement Fluctuations

Let us observe the power spectral density of displacement fluctuations given by expression (5) and shown in Fig. 2 in the vicinity of the resonant frequency:

$$S_X(f + f_0) = \frac{2k_B T}{Qk\pi} \frac{f_0^3}{\left(f^2 + 2f_0 f\right)^2 + \left(\frac{f_0^2}{Q} + \frac{f_0 f}{Q}\right)^2} \quad (14)$$

The power spectral density of phase fluctuations is the ratio of the power spectral density of displacement fluctuations and the mean square of the amplitude  $X_0$  of mechanical oscillations [26]:

$$S_{\phi\{X\}}(f) = \frac{S_X(f + f_0)}{\langle X_0^2 \rangle} \quad (15)$$

In the frequency range of interest it is valid that

$$\frac{f_0}{Q} \ll f \ll f_0. \quad (16)$$

Bearing that in mind the derivations outlined in [18], [25], [26] and in references therein, one comes to the final expression for the power spectral density of phase fluctuations caused by fluctuations in displacement of a mechanical resonator.

$$S_{\phi\{X\}}(f) = \frac{k_B T f_0^2}{Q^2 P_C f^2} \quad (17)$$

Here  $P_C$  is the resonators power dissipation calculated using the Stefan–Boltzmann law.

### D. Phase Noise Induced by Mass Fluctuations

Mass fluctuations directly affect the resonant frequency [20]:

$$f_0 = \sqrt{\frac{k}{m_0 + \Delta m}} \cong f_0 \left(1 - \frac{\Delta m}{2m_0}\right). \quad (18)$$

$m_0$  is the overall mass of the resonator and  $\Delta m$  is the adsorption-induced mass change. The corresponding power spectral density of phase fluctuations of a micro-resonator is then [27]:

$$S_{\phi\{\Delta m\}}(f) = \frac{f_0^2}{f^2} S_y(f) = \frac{f_0^2}{f^2} \frac{S_{\Delta m}(f)}{f_0^2} = \frac{1}{f^2} \frac{S_{\Delta m}(f) f_0^2}{m_0^2}. \quad (19)$$

Now (6) can be used in case when single-component monolayer adsorption takes place on the surface of a micro-resonator. Alternatively, expressions developed in [21] can be used if bi-component monolayer adsorption occurs. One could also use another appropriate expression for the power spectral density of resonator mass fluctuations caused by various adsorption-desorption processes (arbitrary mixture of gases [28], multilayer adsorption [29], adsorption–desorption processes coupled with mass transfer and surface diffusion [30], etc.).

## IV. EXPERIMENTS AND RESULTS

Electrical noise measurements of SP4, SP6 and SOI-SP9 and SP9 pressure sensors produced in ICTM-CMT, Belgrade, Serbia and of pressure sensors produced by KELLER, Switzerland were performed in order to characterize those already produced devices, but also in order to estimate the flicker noise knee and factor alpha needed for the theoretical investigation and the design of micro-cantilevers that may be produced by using the same technology.

The experimental set-up for these electrical noise measurements is shown in Fig. 9

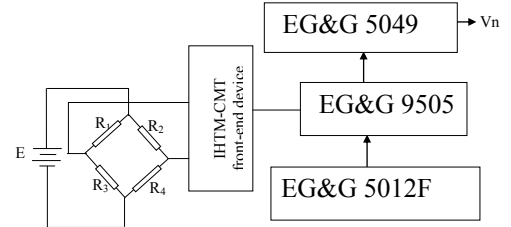


Fig. 9. Experimental set-up for electrical noise measurements. EG&G 5049 is a noise measurement unit, EG&G 9505 is a lock-in analyser and EG&G 5012F is a reference oscillator unit

The Wheatstone bridge is composed of four p-type piezo resistors formed by boron diffusion in n-Si substrate. The piezo resistors are placed on membrane fabricated using bulk micromachining. Voltage supply  $E$  has been built out of 1.5V batteries in order to avoid power line interference, hence its values were 1.5V, 3V, 4.5V, 6V, 7.5V, 9V, 10.5V and 12V - Table I. An analog front-end, designed in ICTM-CMT has been used for signal interface from a sensor under test to a lock-in analyser EG&G 9505. A reference oscillator for lock-in analyser was EG&G 5012F. Measured noise voltage was recorded from a lock/ins noise measurement unit EG&G 5049.

For every measured sensor, each obtained noise spectrum has been fitted with  $y = P1 + P2/x$ . P1 corresponds to thermal noise and P2 corresponds to flicker noise. Fig. 10 shows a

typical noise spectrum.

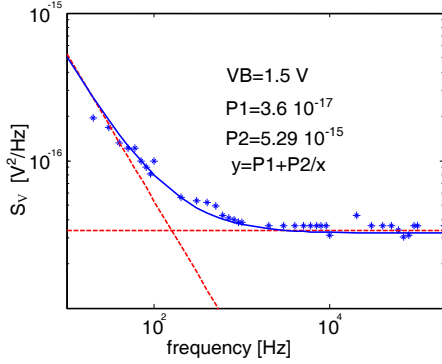


Fig. 10. Symbols: power spectral density of measured voltage fluctuations for SP4 ICTM-CMT pressure sensor, lines: fitting results, voltage supply is 1.5 V

Table I shows some of the results obtained for flicker noise parameter alpha in Hooge's formula, expression (3).

TABLE I  
ALPHA PARAMETER IN HOOGE'S FORMULA FOR FLICKER NOISE

$V_B$ (V)	$P1(10^{-17})$	$P2(10^{-15})$	$\alpha$	$f_c$ (Hz)
1.5	3.6	5.29	2.26	146.944
3	4.9	7.26	0.776	354
4.5	7.22	30.25	1.436	418.7
6	8.1	49	1.3	605
7.5	11.025	88.36	1.51	801.5
9	12.1	100	1.19	826
10.5	16.9	169	1.47	1000

Considering all measurements of CMT components based on boron-doped n-type silicon wafers, the obtained numerical values for the alpha parameter were in a range from  $0.776 \cdot 10^{-4}$  to  $3.8514 \cdot 10^{-4}$ . The results for alpha obtained after measurements of components produced by KELLER were in a range from  $1.899 \cdot 10^{-5}$  to  $1.4603 \cdot 10^{-4}$ .

Obtained values were used for modeling and investigations of limiting performances of a piezo resistive microcantilever shown in Fig. 11. Two cantilevers were considered. The first one, PMG1, has the first mode resonant frequency of 62 kHz and size of  $200 \mu\text{m} \times 2 \mu\text{m} \times 50 \mu\text{m}$ . The second one, PMG2, has the first mode resonant frequency of 110 kHz and a size of  $150 \mu\text{m} \times 2 \mu\text{m} \times 50 \mu\text{m}$ .

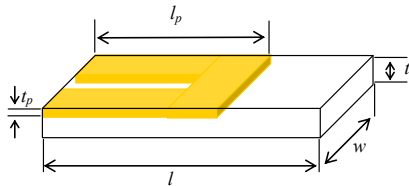


Fig. 11. Schematics of a piezo resistive micro-cantilever

It is assumed that in working conditions microcantilevers are surrounded by a mixture of gases. Table II shows the parameters of gases used in expressions related to adsorption-desorption process. The mean residential time of adsorbed molecules, needed for (7), is calculated using the expression:

$$\tau = \tau_0 e^{E_d/RT} \quad (20)$$

TABLE II  
GAS PARAMETERS

Symbol	Quantity	Meaning
$M_{a1}$	$46.48 \cdot 10^{-27}$ kg	mass of a single molecule of nitrogen
$M_{a2}$	$3.32 \cdot 10^{-27}$ kg	mass of a single molecule of hydrogen
$N_{m1}$	$8 \cdot 10^{18}$ cm <sup>-2</sup>	surface density of adsorbed $N_2$ molecules
$N_{m2}$	$20 \cdot 10^{18}$ cm <sup>-2</sup>	surface density of adsorbed $H_2$ molecules
$\alpha_s$	1	sticking coefficient of gas molecules to surface
$R$	1.978 cal/Kmol	universal gas constant
$E_{d1}$	15.5 kcal/mol	desorption energy of nitrogen molecules
$E_{d2}$	8 kcal/mol	desorption energy of hydrogen molecules
$\tau_0$	$10^{-13}$ s	period of crystal lattice vibrations

Fig. 12 shows typical results for phase noise components calculated in order to estimate the level of instability of a micro-cantilever with piezo resistive read-out. The results are given for the piezo-resistive micro-cantilever PMG1.  $E$  stands for the intrinsic noise sources induced by circuits for electrical read-out, i.e. Johnson-Nyquist and flicker noise, calculated using the experimentally obtained alpha parameter in Hooge's formula and Leeson's model with the quality factor of a resonator in a closed loop  $Q = 100$ .  $T$  stands for phase noise induced by temperature fluctuations.  $TM$  stands for thermo-mechanical noise and  $AD$  is for noise induced by adsorption and desorption of nitrogen molecules at a pressure of 10 Pa and hydrogen molecules at a pressure of 0.001 Pa.

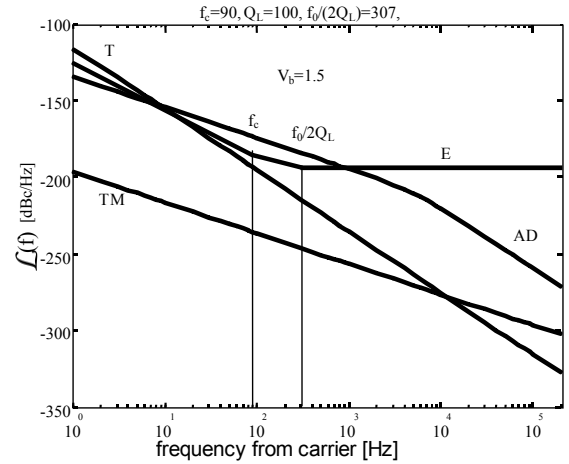


Fig. 12. Phase noise of a micro-cantilever induced by: thermomechanical noise (TM), fluctuations in temperature (T), voltage fluctuations due to Johnson-Nyquist and flicker noise (E) and adsorption-desorption noise (AD) due to traces of nitrogen (at 10 Pa) and hydrogen (0.01 Pa) in the vicinity of the piezo resistive micro-cantilever surface

## V. DISCUSSION AND CONCLUSIONS

Noise in MEMS and NEMS has been studied in 1999 [33] and after a decade it is still a topic of great importance for many applications [6]. Experimental and numerical results given in this paper demonstrate an application of a systematic theoretical apparatus for the complete analysis of heterogeneous intrinsic noise in an arbitrary micro-resonator and may be also applied to an arbitrary micro-electro-mechanical structure including similar resonating parts: micro-cantilevers, micro-bridges, micro-membranes etc.

The outlined theory enables a comparative analysis of heterogeneous intrinsic noise mechanisms in micro-electromechanical resonators. The results imply that with scaling, in MEMS components, some intrinsic noise mechanisms may be promoted. This is in particular valid for adsorption-desorption noise that is insignificant in larger devices, but in certain frequency ranges in MEMS devices may prove itself dominant.

It has been shown how one can estimate the joint effect of separate noise sources on limiting performances of MEMS resonators.

The experimentally obtained values of the parameter  $\alpha$  in Hooge's formula for power spectral density of flicker noise fit well in ranges for  $\alpha$  reported in literature: in [14]  $\alpha$  is  $2 \cdot 10^{-3}$ , in [31]  $\alpha$  is ranged from  $3 \cdot 10^{-6}$  to  $3 \cdot 10^{-4}$  and in [32]  $\alpha$  ranges from  $10^{-7}$  to  $10^{-3}$  depending on the material (polycrystalline, crystalline, amorphous silicon).

#### REFERENCES

- [1] B. A. Cetiner, J. Y. Qian, H. P. Chang, M. Bachman, G. P. Li, and F. De Flaviis, "Monolithic integration of RF MEMS switches with a diversity antenna on PCB substrate," *IEEE Trans. Microw. Theory Tech.*, vol. 51, no. 1, pp. 332–335, Jan. 2003.
- [2] T. Mattila, J. Kiihamäki, T. Lamminmäki, O. Jaakkola, P. Rantakari, A. Oja, H. Seppä, H. Kattelus, and I. Tittonen, "A 12 MHz micromechanical bulk acoustic mode oscillator," *Sensors Actuators A Phys.*, vol. 101, no. 1–2, pp. 1–9, Sep. 2002.
- [3] A. N. Cleland and M. L. Roukes, "Fabrication of high frequency nanometer scale mechanical resonators from bulk Si crystals," *Appl. Phys. Lett.*, vol. 69, no. 18, pp. 2653–2655, 1996.
- [4] T. D. Stowe, K. Yasumura, T. W. Kenny, D. Botkin, K. Wago, and D. Rugar, "Attomewton force detection using ultrathin silicon cantilevers," *Appl. Phys. Lett.*, vol. 71, no. 2, pp. 288–290, 1997.
- [5] K. L. Ekinci, "Ultimate limits to inertial mass sensing based upon nanoelectromechanical systems," *J. Appl. Phys.*, vol. 95, no. 5, p. 2682, 2004.
- [6] F. Mohd-Yasin, D. J. Nagel, and C. E. Korman, "Noise in MEMS," *Meas. Sci. Technol.*, vol. 21, no. 1, p. 012001, Jan. 2010.
- [7] H. W. Ott, *Electromagnetic Compatibility Engineering*. Wiley, 2011.
- [8] J. B. Johnson, "Thermal agitation of electricity in conductors," *Phys. Rev.*, vol. 32, no. 1, pp. 97–109, 1928.
- [9] H. Nyquist, "Thermal agitation of electric charge in conductors," *Phys. Rev.*, vol. 32, no. 1, pp. 110–113, 1928.
- [10] H. Callen and T. Welton, "Irreversibility and Generalized Noise," *Phys. Rev.*, vol. 83, no. 1, pp. 34–40, Jul. 1951.
- [11] J. B. Johnson, "Thermal Agitation of Electricity in Conductors," *Nature*, vol. 119, pp. 50–51, 1927.
- [12] H. Wong, "Low-frequency noise study in electron devices: review and update," *Microelectron. Reliab.*, vol. 43, no. 4, pp. 585–599, Apr. 2003.
- [13] F. N. Hooge, J. Kedzia, and L. K. J. Vandamme, "Boundary scattering and 1/f noise," *J. Appl. Phys.*, vol. 50, no. 12, p. 8087, 1979.
- [14] F. N. Hooge, "1/f noise sources," *IEEE Trans. Electron Devices*, vol. 41, no. 11, pp. 1926–1935, 1994.
- [15] F. N. Hooge, T. G. M. Kleinpenning, and L. K. J. Vandamme, "Experimental studies on 1/f noise," *Reports Prog. Phys.*, vol. 44, no. 5, pp. 479–532, May 1981.
- [16] Z. Djurić, J. Matović, D. Randjelović, Z. Jakšić, and T. Danković, "Noise in Micromechanical Structures Caused By Temperature Fluctuations," in *5th NEXUSPAN Workshop on Thermal Aspects in Microsystem Technology, 6-8 May 1998, Budapest, Hungary*, 1998, pp. 142–151.
- [17] F. Bordononi and A. D'Amico, "Noise in sensors," *Sensors Actuators A Phys.*, vol. 21, no. 1–3, pp. 17–24, Feb. 1990.
- [18] O. Jakšić, "Noise in MEMS," University of Belgrade, 2005, Mag. thesis.
- [19] Y. K. Yong and J. R. Vig, "Resonator Surface Contamination - A Cause of Frequency fluctuations?," *IEEE Trans Ultrason Ferroelectr Freq Control*, vol. 36, no. 4, pp. 452–458, 1989.
- [20] Z. Djurić, O. Jakšić, and D. Randjelović, "Adsorption-desorption noise in micromechanical resonant structures," *Sensors Actuators, A Phys.*, vol. 96, no. 2–3, pp. 244–251, Feb. 2002.
- [21] Z. Djurić, L. Jokić, M. Frantlović, O. Jakšić, and D. Vasiljević-Radović, "Adsorbed mass and resonant frequency fluctuations of a microcantilever caused by adsorption and desorption of particles of two gases," in *24th International Conference on Microelectronics (IEEE Cat. No. 04TH8716)*, 2004, vol. 1, pp. 197–200.
- [22] "IEEE Std 1139-1999," *IEEE Std 1139-1999*. p. 0\_1-, 1999.
- [23] A. Hajimiri and T. H. Lee, "A general theory of phase noise in electrical oscillators," *IEEE J. Solid-State Circuits*, vol. 33, no. 2, pp. 179–194, 1998.
- [24] D. B. Leeson, "A simple model of feedback oscillator spectrum," *Proc. Lett. IEEE*, vol. February, pp. 329–330, 1966.
- [25] J. R. Vig and Y. Kim, "Noise in microelectromechanical system resonators," *IEEE Trans Ultrason Ferroelectr Freq Control*, vol. 46, no. 6, pp. 1558–1565, 1999.
- [26] A. N. Cleland and M. L. Roukes, "Noise processes in nanomechanical resonators," *J. Appl. Phys.*, vol. 92, no. 5, pp. 2758–2769, 2002.
- [27] I. Jokić, M. Frantlović, Z. Djurić, and M. Dukić, "Adsorption-desorption phase noise in RF MEMS/NEMS resonators," in *2011 10th International Conference on Telecommunication in Modern Satellite Cable and Broadcasting Services (TELSIKS)*, 2011, pp. 114–117.
- [28] Z. Djurić, I. Jokić, M. Frantlović, and O. Jakšić, "Fluctuations of the number of particles and mass adsorbed on the sensor surface surrounded by a mixture of an arbitrary number of gases," *Sensors Actuators B Chem.*, vol. 127, no. 2, pp. 625–631, Nov. 2007.
- [29] Z. G. Djurić, I. M. Jokić, M. M. Djukić, and M. P. Frantlović, "Fluctuations of the adsorbed mass and the resonant frequency of vibrating MEMS/NEMS structures due to multilayer adsorption," *Microelectron. Eng.*, vol. 87, no. 5–8, pp. 1181–1184, May 2010.
- [30] Z. Djurić, I. Jokić, and A. Peleš, "Fluctuations of the number of adsorbed molecules due to adsorption-desorption processes coupled with mass transfer and surface diffusion in bio/chemical MEMS sensors," *Microelectron. Eng.*, vol. 124, pp. 81–85, Jul. 2014.
- [31] J. A. Harkey and T. W. Kenny, "1/f noise considerations for the design and process optimization of piezoresistive cantilevers," *J. Microelectromechanical Syst.*, vol. 9, no. 2, pp. 226–235, 2000.
- [32] L. K. J. Vandamme, "Is the 1/f noise parameter  $\alpha$  a constant?," in *7th International Conf. on "Noise in Physical Systems" and 3rd International Conference on 1/f noise, Montpellier, France, 17-20 May 1983*.
- [33] Z. Djurić, "Mechanisms of noise sources in microelectromechanical systems," *Microelectron. Reliab.*, vol. 40, no. 6, pp. 919–932, 1999.

# Prototype of the Multichannel Acquisition System Developed for ICTM Pressure Transmitters

P. Poljak, B. Vukelić, M. Vorkapić and D.V. Randjelović

**Abstract**— This paper presents a prototype of the multichannel acquisition unit AKV-100 developed for purposes of pressure and temperature measurements using proprietary ICTM pressure transmitters TPa-110 based on MEMS piezoresistive pressure sensors and thermocouples TMMU01. Details about the acquisition unit, dedicated software, measurement setup and test procedure are given. Measurements results are presented and the directions of future research activities are discussed.

**Index Terms**—acquisition, pressure measurement, pressure transmitter, thermocouples, MEMS pressure sensors.

Original Research Paper

DOI: 10.7251/ELS1519066P

## I. INTRODUCTION

THE ACQUISITION unit AKV-100 was realized because of need for the development of a low-cost and flexible system that would allow simultaneous data acquisition from pressure transmitters and thermocouples fabricated by ICTM – CMT. Commercially available acquisition systems dedicated for data acquisition from pressure transmitters and K-type thermocouples have a significantly higher price than AKV-100. Besides, the existing systems usually are of modular type, with a separate module for pressure transmitters and another module for the thermocouples. They are connected with the central unit and power supply, which are also independent modules. Previous research at ICTM-CMT was following that direction too [1].

The AKV-100 unit enables user to perform data acquisition from 9 channels, 4 of which are dedicated for ICTM pressure transmitters TPa-110 [2, 3], while 5 channels are to be connected with K-type thermocouples TMMU01.

Manuscript received 08 November 2015. Received in revised form 15 December 2015.

This work has been partially supported by the Serbian Ministry of Education, Science and Technological Development within the framework of the Project TR32008.

P. Poljak, B. Vukelić, M. Vorkapić and D.V. Randjelović are with the Centre of Microelectronic Technologies, Institute of Chemistry, Technology and Metallurgy, University of Belgrade, Njegoševa 12, 11000 Belgrade, Serbia, (corresponding author to provide phone: +381-11-2628-587; fax: +381-11-2182-995; e-mail: predrag.poljak@nanosys.ihm.bg.ac.rs).

The first part of the paper gives details about the acquisition system, AKV-100 unit, measurement setup and dedicated software. In the second part, experimental results obtained in laboratory conditions, using one active channel for pressure transmitter are given. Finally, the obtained test results and the directions of future research are discussed.

## II. ACQUISITION SYSTEM

### A. Acquisition Unit AKV-100

The Acquisition unit AKV-100 is developed at ICTM for acquisition of measurement data from 9 channels. The block diagram in Fig. 1. shows the acquisition module together with other components, PC with the installed special software developed at ICTM-CMT, 4 pressure transmitters TPa-110, 5 thermocouples TMMU01 and the external supply 24V/850mA.

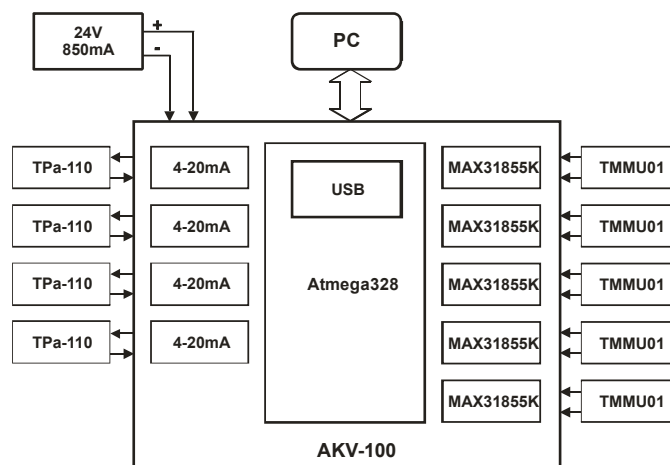


Fig. 1. Block diagram of the acquisition module AKV-100 illustrating pressure transmitters (TPa-110) and thermocouples (TMMU01) connected to all available measurement channels. PC with special software and external power supply for the pressure transmitters is also shown.

The pressure transmitters TPa-110 are intended for the measurement of absolute or gauge pressure, utilize MEMS-based piezoresistive pressure sensor chips fabricated in ICTM-CMT and give the standard 5-20 mA industrial output.

Apart from a lower cost, as mentioned before, the acquisition unit AKV-100 has the following advantages:

1. User-friendly power supply realized through a USB communication cable. The same supply is used for thermocouples, while an independent additional supply 24V/0.84A is used for pressure transmitters,

2. Analogue to digital conversion of the signal collected from the thermocouples is performed in modules which contain MAX31855K integrated circuit which performs conversion and then transfers the data to the local microcontroller via SPI interface bus,

3. The same two connection lines of the transmitters serve not only for the signal transfer like in available commercial solutions, but also for the power supply provided by AKV-100 itself. .

The central part of the AKV-100 acquisition unit is an 8-bit microcontroller Atmel Atmega328 [4] with external modules. Pressure transmitters generate an analog current signal in the 4-20mA range . The current signal produces voltage drop across a resistor, which is input into internal 10-bit A/D converter. Since current is linearly dependent on  $\epsilon$  pressure, and voltage drop is proportional to current, pressure value for each channel, can easily be determined using the next equation:

$$U_{ad}[i] = \frac{V_{ref}}{2^{10}} * voltage\_read[i],$$

$$I\_current[i] = \frac{U_{ad}[i]}{R_{ref}} * 1000,$$

$$pressure[i] = k * I\_current[i] + n,$$
(1)

where  $voltage\_read[i]$  is the current digital value of voltage generated by A/D converter,  $U_{ad}$  is analogue value of the same voltage,  $V_{ref} = 5\text{ V}$  is the reference voltage of A/D converter,  $I\_current[i]$  is analogue value of the current in mA,  $R_{ref}$  is the reference resistor,  $pressure[i]$  is the value of the measured pressure. Coefficients  $k$  and  $n$  depend on the pressure range of the transmitter. The TPa-110 pressure transmitters are optimized for a pressure range of (0-10) bar.

Analogue signals collected from the thermocouples are firstly sent to the integrated circuit MAXIM MAX31855K and the obtained digital signals are transferred afterwards to the microcontroller via SPI interface bus. AKV-100 contains 5 MAXIM MAX31855K circuits which share one SPI interface bus with the microcontroller.

### B. Experimental Setup

The experimental setup is shown in Fig. 2. ICTM transmitters are placed inside the temperature test chamber HERAEUS VÖTSCH VMT 08/140 which assures good temperature control. The transmitters are connected with the acquisition unit AKV-100, which performs, among other operations, pressure calculation.

Fig. 3 shows a photograph of the four ICTM TPa-110 pressure transmitters connected with the AKV-100 acquisition unit.

The pressure calibrator (MENSOR APC-600) sets the pressure in ascending and then descending order in the range from 0.1-10.1 bar with the step of one bar. User application

software performs communication with the pressure calibrator as well as with the AKV-100 acquisition unit.

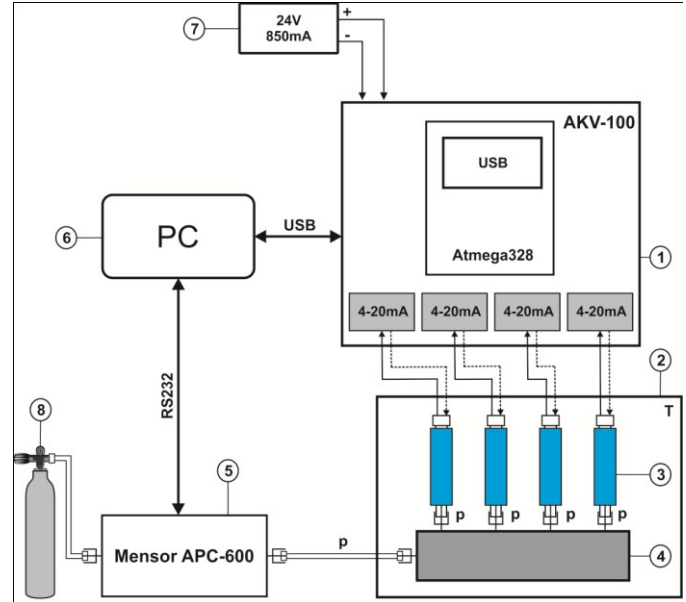


Fig. 2. Experimental setup: 1) AKV-100 acquisition unit, 2) temperature test chamber, 3) Pressure transmitters, 4) pneumatic manifold, 5) Pressure Calibrator Mensor APC-600, 6) PC with software for AKV-100, 7) external power supply, 8) nitrogen container.

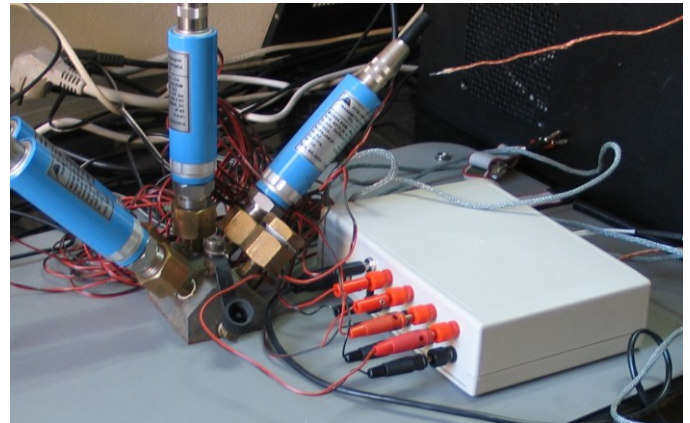


Fig. 3. Photograph of the four ICTM TPa-110 pressure transmitters connected with the AKV-100 acquisition unit.

### C. Software for AKV-100

For the development of user application, ANSI C language was used as one of the most widespread test and measurement programming languages. Source code was created within the ANSI C integrated development environment LabWindows/CVI [5].

Communication between PC and MENSOR APC-600 pressure calibrator is realized by a "Virtual Serial COM Port". The user chooses the relevant "Virtual Serial COM Port" and afterwards the switch "Start Mensor" is set to "ON" position. In this way communication is established and the value of pressure generated by MENSOR APC-600 [6] is shown in the associated field of the user application window as shown in Fig 4.

Communication with the acquisition device AKV-100 is established in a manner similar to the one described above. The user chose the relevant “Virtual Serial COM Port” and this time the switch “Start AKV” is set to “ON” position. As soon as communication is established, the value of the current output signal generated by the pressure transmitter is displayed in the associated field of the user interface window. After choosing the appropriate transmitter pressure range, the pressure value proportional to the measured current is calculated. This value is also displayed in the associated field of the user application window.

The user application has two internal “timers” which are invisible and not available to user. One timer performs periodic voltage acquisition from the AKV-100 unit, while the other calculates the value of the pressure measured by ICTM pressure transmitter based on the collected data using (1).

Automatic data acquisition from the pressure calibrator and the acquisition device is enabled by the switch “Automatsko Merenje”. During the automatic acquisition, pressure and current values are collected subsequently and the data are stored in dedicated file.

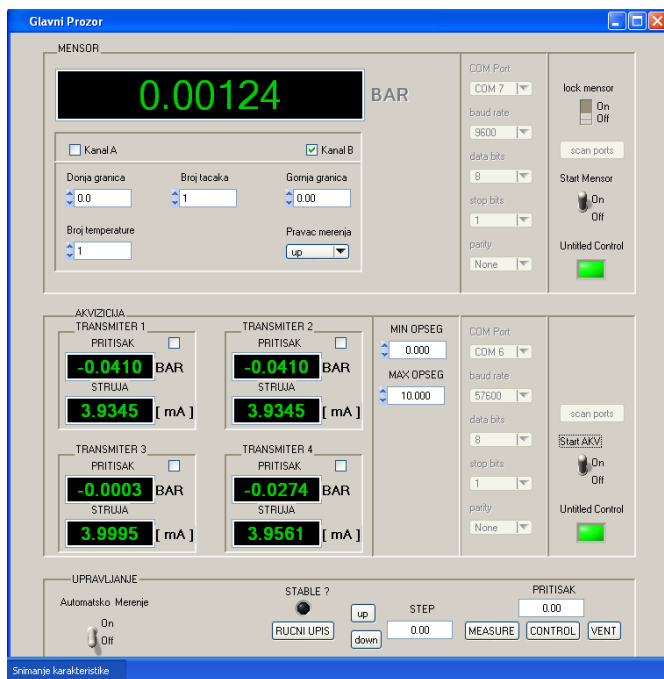


Fig. 4. User application window.

### III. MEASUREMENT RESULTS

Measurements were performed in laboratory conditions using the above mentioned temperature test chamber which is limited to a relatively narrow temperature range (-80 - 180 °C), far below the operating range of the K-type thermocouples, therefore the channels for the thermocouples were not used. Pressure transmitters were connected to the respective channels of AKV-100. The transmitters were placed in a temperature test chamber HERAEUS VÖTSCH VMT 08/140. Measurements were done at three different temperatures, (-10, 17.7, 50) °C. Reference pressure was generated by a MENSOR

APC-600 pressure calibrator.

After setting the chamber temperature, 30 minutes were allowed for the temperature stabilization. At each selected temperature measurement sequence was controlled by software. For each reference pressure value, the transmitter output was recorded. MENSOR APC-600 generated several pressure values and for each reference value, the transmitter output was recorded.

Fig. 5 shows dependance of the raw transmitter output, which is a current signal, on all reference pressure values in one measurement sequence obtained at a temperature of 17.7 °C.

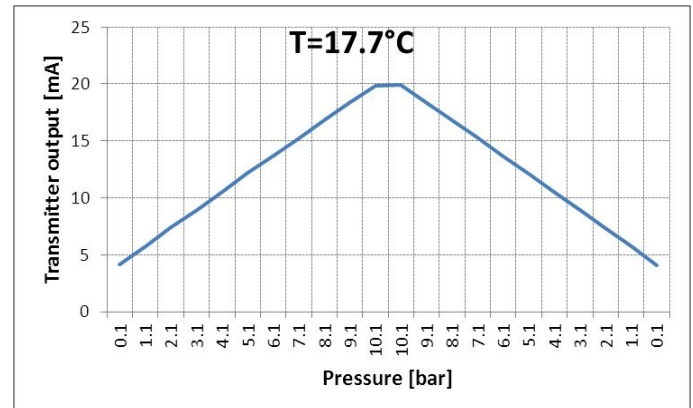


Fig. 5. Dependence of the raw transmitter output (current signal) measured at temperature 17.7°C on reference pressures generated by MENSOR APC-600 pressure calibrator.

The current value recorded at the output of pressure transmitter was further transformed into measured pressure value which was displayed in the user interface window.

Fig. 6 shows pressure values measured by the ICTM transmitter and the corresponding reference values generated by MENSOR APC-600 pressure calibrator. Pressures measured at all test temperatures for each calibration pressure are listed in Table I.

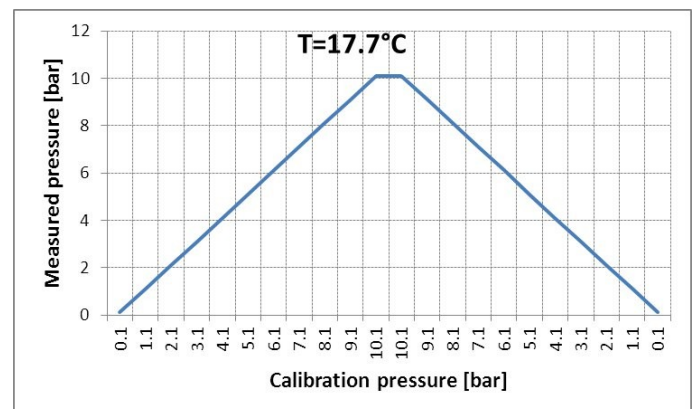


Fig. 6. Dependence of the pressure values measured by transmitter and displayed in the User application window on reference pressures generated by MENSOR APC-600 pressure calibrator.

TABLE I  
PRESSURES MEASURED BY ICTM TRANSMITTER AT THREE DIFFERENT  
TEMPERATURES FOR EACH REFERENCE PRESSURE GENERATED BY  
MENSOR APC-6000 PRESSURE CALIBRATOR

MENSOR [bar]	AKV-100 [bar]		
	T=50°C	T=17.7°C	T=-10°C
0.1	0.100086	0.100043	0.099841
1.1	1.10001	1.10001	1.10001
2.1	2.10001	2.09998	2.1
3.1	3.10001	3.09999	3.09999
4.1	4.1	4.09999	4.10001
5.1	5.10002	5.10001	5.1
6.1	6.10001	6.1	6.1
7.1	7.10002	7.10001	7.1
8.1	8.10002	8.10001	8.10001
9.1	9.10002	9.10001	9.10001
10.1	10.1	10.1	10.1
10.1	10.1	10.1	10.1
9.1	9.10001	9.09999	9.09998
8.1	8.10001	8.10002	8.1
7.1	7.1	7.10001	7.10001
6.1	6.09998	6.10002	6.10003
5.1	5.10003	5.1	5.1
4.1	4.09999	4.09999	4.10002
3.1	3.1	3.10002	3.1
2.1	2.1	2.09999	2.10001
1.1	1.09999	1.1	1.09998
0.1	0.099872	0.099943	0.099936

#### IV. CONCLUSION

A prototype of the multichannel acquisition system dedicated for use with ICTM pressure transmitters and thermocouples was developed. The system was successfully tested in a configuration with one ICTM pressure transmitter connected.

As expected, the main limitation of the realized prototype, is the low accuracy. For the future solution, it is planned to use an A/D converter with higher resolution.

Research and development of various types of transmitters for the industrial use is one of the main activities at ICTM-CMT. In order to successfully place transmitters on the market, it is of interest to develop various interfaces as well as specialized acquisition devices compatible with international industrial standards. The prototype presented in this work is the first device of such kind developed at ICTM-CMT. In the near future we expect to develop improved acquisition systems.

#### REFERENCES

- [1] M. Vorkapić, M. Starčević, B. Popović, M. Frantlović, P. Poljak, S. Minić "Model of improvement transducers in small series production", *Tehnika*, pp. 1043-1047, 2011.
- [2] M. Matić, Ž. Lazić, K. Radulović, M. M. Smiljanić, M. Rašljčić "Experimental Determination of Optimal Piezoresistive Pressure Sensor Linearity" in *Proc. of 57th ETRAN Conference*, Zlatibor, Serbia, June 3-6, 2013, pp. MO3.1.1-6 (in Serbian)
- [3] M.P. Frantlović, V.J. Jovanov, B.L. Miljković, „Intelligent Industrial Transmitters of Pressure and Other Process Parameters“, *Telfor J.* Vol. 1,2, pp. 65–68., 2009.
- [4] <http://www.atmel.com/devices/atmega328.aspx>
- [5] <http://www.ni.com/lwcv/technical-resources/>
- [6] [http://www.mensor.com/cpc6000\\_en\\_co.WIKA](http://www.mensor.com/cpc6000_en_co.WIKA)

# Analytical modelling of the transient response of thermopile-based MEMS sensors

D.V. Randjelović, A.G. Kozlov, O.M. Jakšić, M.M. Smiljanić and P.D. Poljak

**Abstract**—This work presents an analytical model dedicated to study of the transient response of multipurpose MEMS devices based on thermopile sensors. In general, thermopile sensors response depends on ambient temperature, thermal conductivity of the gas inside the housing and the pressure of the gas. The presented model takes into account all these parameters. This model was successfully implemented for the study of transient behaviour of our multifunctional sensors with p<sup>+</sup>Si/Al thermocouples and a bulk micromachined bilayered membrane. Simulations were performed for different gases of interest and conclusions were deduced regarding the influence of relevant parameters on the thermal time constant. This analytical approach is general and flexible enough to be implemented for analysis of the transient behaviour of thermopile-based sensors when used for different applications.

**Index Terms**— analytical modelling, MEMS sensors, thermopile, transient response

Original Research Paper  
DOI: 10.7251/ELS1519070R

## I. INTRODUCTION

Thermopile-based MEMS sensors belong to thermal type sensors with a broad range of applications (IC sensors, thermal converters, accelerometers, flow sensors, vacuum sensors, gas type sensors, chemical sensors ...) [1-6]. Their performance depends on processes of heat transfer on the chip as well as on the thermal interaction between the sensor and the surrounding ambient.

We developed multifunctional sensors with p<sup>+</sup>Si/Al thermocouples and p<sup>+</sup>Si (P-type) or Al (A-type) heater which were successfully tested as flow sensors, vacuum sensors and thermal converters [4-6]. The thermal isolating structure is a bilayer membrane consisting of sputtered silicon dioxide and a residual n-Si layer.

Manuscript received 30 October 2015. Received in revised form 20 October 2011.

This work has been partially supported by the Serbian Ministry of Education, Science and Technological Development within the framework of the Project TR32008.

D.V. Randjelović, O.M. Jakšić, M.M. Smiljanić and P.D. Poljak are with the Centre of Microelectronic Technologies, Institute of Chemistry, Technology and Metallurgy, University of Belgrade, Njegoševa 12, 11000 Belgrade, Serbia, (corresponding author to provide phone: +381-11-2628-587; fax: +381-11-2182-995; e-mail: danijela@nanosys.ihm.bg.ac.rs).

A.G. Kozlov is with Omsk State University, Pr. Mira, 55a, Omsk, 644077, Russia

The performance of these sensors is strongly influenced by residual n-Si thickness. Apart from this parameter, thermopile sensors response depends on the ambient temperature, the thermal conductivity of the gas inside the housing and the pressure of the gas. This work presents an analytical model which takes into account all the relevant parameters mentioned above and is dedicated to study of transient response of multipurpose devices based on thermopile sensors.

## II. ANALYTICAL MODELING OF TRANSIENT RESPONSE

Based on the core analytical model introduced in [4], several special models were developed with the purpose of studying multipurpose sensor performance when the device is used for a specific application [5, 6]. The same situation is with the model described in this work. In the first part of this section the structure of A- and P-type thermopile based MEMS sensors is given, and in the second part, analytical model dedicated for study of transient response of these sensors is presented.

### A. Sensor structure

Figure 1 shows a structure of a P-type sensor with a p<sup>+</sup>Si heater mounted on a TO-8 housing. Two independent thermopiles with 30 thermocouples each are placed on a sandwich membrane consisting of sputtered silicon dioxide (1 μm) and a residual n-Si layer. A-type structures have the same design, the only difference is that their heater is formed of sputtered Al placed on the upper side of the membrane. Functional structures with residual layer thicknesses ( $d_{n-Si}$ ) in the range (3 - 25) μm were fabricated.

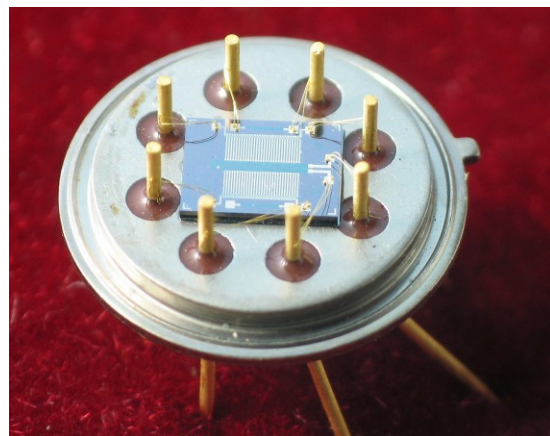


Fig. 1. P-type sensor mounted on TO-8 housing.

Figure 2 depicts the cross section of the structure along the shorter side of the chip. The lengths of the two zones used in analytical modelling are also shown. The zone 0 with the length  $l_0$  is delimited by the middle of the chip and the outer edge of the heater. The zone 1 with the length  $l_1$  is delimited by the outer edge of the heater and the membrane edge.

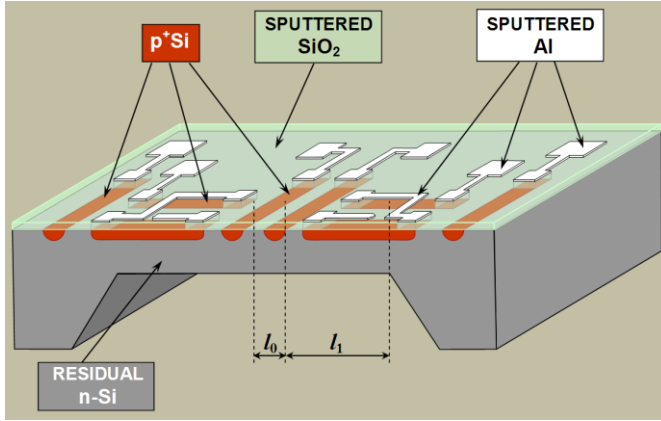


Fig. 2. Cross section of the P-type structure.

### B. Analytical model of transient response

The thermal time constant ( $\tau$ ) of the sensors was calculated using expressions derived in [4, 7] which were modified by taking into account the pressure and temperature dependence of gas thermal conductivity. Influence of gas pressure was taken into account using relations presented in [6], while the temperature dependence of the thermal conductivity of the specific gas was calculated using data given in [3].

We assume that the sensor is mounted in a housing so that the distance between the upper side of the sensor and the housing cap is  $d_u$  and the distance between the bottom side of the membrane and the housing base is  $d_b$ . Taking into account the influence of both pressure and temperature, the thermal conductivity of the gas inside the housing can be calculated using the following relation:

$$\lambda_{gas}(p, T) = \left( \frac{1}{\lambda_{hp}(T)} + \frac{1}{\gamma_{lp}(T)p} (d_u^{-1} + d_b^{-1}) \right)^{-1} \quad (1)$$

Parameters  $\lambda_{hp}$  and  $\gamma_{lp}$  are characteristic for the high and the low pressure region, respectively. The temperature dependence of the parameter  $\lambda_{hp}$  is described by relation given in [3]

$$\lambda_{hp} [mW/(Km)] = A \cdot (T/1000)^2 + B \cdot (T/1000) + C \quad (2)$$

where  $T$  is temperature in Kelvins [K], while A, B and C are constant coefficients.

At lower pressures, the dominant parameter is  $\gamma_{lp}$  which can be determined using relation given in [8]

$$\gamma_{lp}(T) = \frac{c}{3} \sqrt{\frac{8M}{\pi k_B T}} \quad (3)$$

where  $k_B = 1.38 \cdot 10^{-23}$  J/K is Boltzmann's constant,  $c$  is the specific heat capacity,  $M$  is the molecular weight and  $T$  is the ambient temperature.

The model presented in this work is based on the analytical model with two zones described in detail in [4]. The characteristic dimensions ( $l_0$  and  $l_1$ ) of each rectangular zone  $j = \{0, 1\}$  of the two-zone model are marked in Figure 2. The length of the first zone,  $l_0$ , is constant and for the specific design equals 0.18 mm. The length of the second zone,  $l_1$ , depends on  $d_{n-Si}$ . In the case of anisotropic etching of Si (100) wafer with a nominal thickness of 380  $\mu m$  the following relation is valid:

$$l_1 = 1620 \mu m - \left( 560 \mu m + \frac{380 \mu m - d_{n-Si} [\mu m]}{\tan(54.7^\circ)} \right) \quad (4)$$

In general, in the zone "j" there are "n" layers of different materials "i" with their thickness  $d_i^j$ . In this model each multilayered zone is replaced with homogenous one characterized by equivalent parameters. In order to determine these parameters the coefficient of "coverage"  $k_i^j$  is introduced, defined as the ratio of the area covered by elements fabricated of material "i" to the area of the zone "j". Besides, for each zone the equivalent thickness is calculated using formula

$$d_e^j = \sum_{i=1}^n k_i^j d_i^j \quad (5)$$

Based on this value, equivalent values of other parameters such as thermal conductivity ( $\lambda_e$ ), thermal diffusivity ( $a_e$ ), specific heat capacity ( $c_e$ ) and density ( $\rho_e$ ) can be calculated using general expression

$$\eta_e^j = \left( \sum_{i=1}^n k_i^j d_i^j \eta_i^j \right) / d_e^j \quad (6)$$

where  $\eta_e^j$  represents any of the above listed parameters.

Using expressions derived in [4] the equation for the thermal time constant in the first order approximation can be deduced

$$\tau_1(p, T) = \frac{(l_0 + l_1)^2}{\left( \frac{\pi}{2} \right)^2 a_e + \left( \frac{A_0(p, T)}{c_{e0} \rho_{e0} d_0} + \frac{A_1(p, T)}{c_{e1} \rho_{e1} d_1} \right) (l_0 + l_1)} \quad (7)$$

where:

- coefficient of total convective and radiative losses for the two zones is

$$A_j(p, T) = h_j(p, T) + 4\sigma_B(\epsilon_{ju} + \epsilon_{jl})T^3, \quad j = \{0, 1\} \quad (8)$$

where  $\sigma_B = 5,67 \cdot 10^{-8} \text{ W/(m}^2\text{K}^4)$  is Stefan-Boltzmann constant, while  $\epsilon_{ju}$  and  $\epsilon_{jl}$  are emissivities of the upper and the lower surface of the zone “j”,

- convection coefficients for each zone are

$$h_j(p, T) = \lambda_{gas}(p, T) \left( d_u^{-1} + d_b^{-1} \right), \quad j = \{0, 1\}, \quad (9)$$

- equivalent thermal diffusivity,  $a_e$ , of the whole structure is determined based on the values of this parameter calculated for each zone using general formula (6), which are substituted in following expression

$$a_e = \frac{a_{e0}l_0 + a_{e1}l_1}{l_0 + l_1}. \quad (10)$$

### III. RESULTS

Based on the analytical expressions derived in previous section, transient behaviour of the sensors was studied for an atmosphere of nitrogen ( $\text{N}_2$ ), helium (He) and carbon dioxide ( $\text{CO}_2$ ) at different ambient temperatures. The results obtained for nitrogen are a good approximation for air due to the dominant part of nitrogen in air composition.

The values of coefficients and parameters appearing in (2) and (3) are listed in Table I. The molecular weight of the chosen gases,  $M$ , is expressed in atomic mass units ( $1 \text{ u} = 1.66 \cdot 10^{-27} \text{ kg}$ ).

TABLE I

VALUES OF COEFFICIENTS A, B AND C USED IN (2) FOR CALCULATION OF  $\lambda_{HP}$  AND PARAMETERS OF THE GASES OF INTEREST USED IN (3) FOR CALCULATION OF  $\gamma_{LP}$

GAS	A	B	C	$c$ [J/kgK]	$M$ [u]
Nitrogen ( $\text{N}_2$ )	-30	+90	+1.1	1041	28
Helium (He)	-100	+418	+37.6	5193	4
Carbon dioxide ( $\text{CO}_2$ )	-1	+83	-7.74	851	44

Figure 3 presents a typical pressure dependence of gas thermal conductivity for all three chosen gases. Since helium has the highest thermal conductivity at atmospheric pressure, it undergoes the most prominent change with the change of pressure.

The transient response of the sensor is illustrated by its thermal time constant. Figure 4 shows the results of analytical simulation obtained for a P-type structure with  $d_{n-Si} = 5 \mu\text{m}$  in nitrogen atmosphere for different ambient temperatures in the range (10 - 40) °C. It is obvious that ambient temperature does

not have strong influence on the thermal time constant of the sensor. The influence of different gases on thermal time constant of the sensor was also studied.

Figure 5 shows simulation data obtained for a P-type structure with  $d_{n-Si} = 3 \mu\text{m}$  and a structure with completely removed residual n-Si ( $d_{n-Si} = 0 \mu\text{m}$ ). The analysis was performed for the three chosen gases at an ambient temperature of 20 °C. The structure with completely removed residual n-Si is fabricated on a SOI wafer, which assures excellent thermal isolation. This effect in general improves the sensor performance. As illustrated in Fig. 5., at atmospheric pressure, the thermal time constant of the SOI structure is higher than in Si structure in nitrogen and carbon dioxide, while it remains the same for helium.

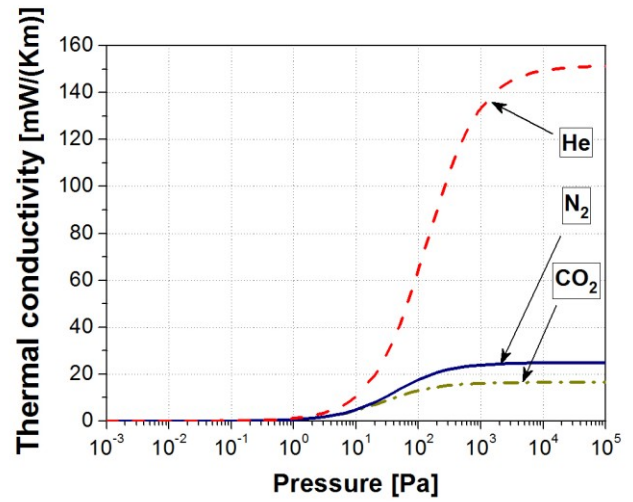


Fig. 3. Pressure dependence of thermal conductivity of helium, nitrogen and carbon dioxide at 20 °C.

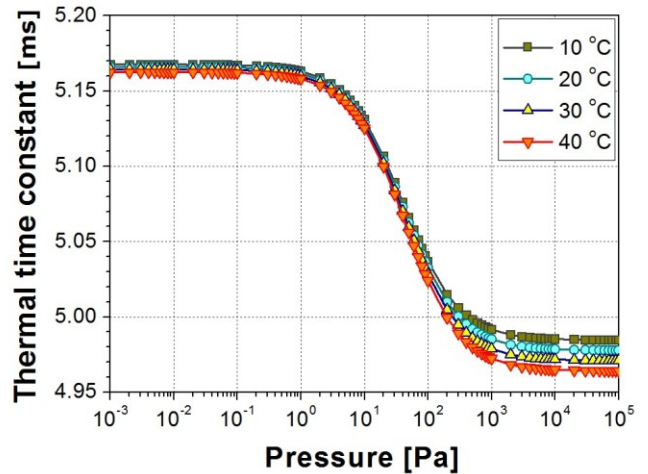


Fig. 4. Dependence of thermal time constant on nitrogen pressure at ambient temperatures (10, 20, 30, 40) °C. Simulations were obtained for P-type structure with  $d_{n-Si} = 5 \mu\text{m}$ .

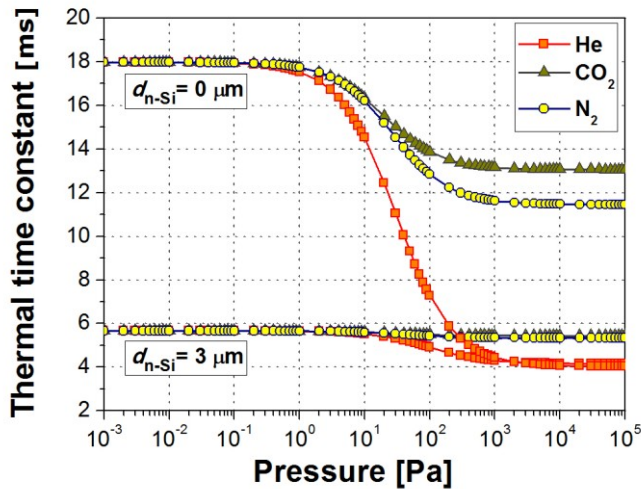


Fig. 5. Dependence of thermal time constant on pressures of He, CO<sub>2</sub> and N<sub>2</sub>. Simulations were performed for P-type structures with  $d_{n-Si} = 3 \mu\text{m}$  and  $d_{n-Si} = 0 \mu\text{m}$  at ambient temperature of 20 °C.

Experiments were also conducted in order to measure the thermal time constant of the fabricated sensors. For this purpose, the heater of the sensors was connected to Hewlett-Packard 8002A Pulse Generator. Voltage pulses with 1.01 V amplitude, 100 ms width and a very long period were applied. The output signal was Seebeck voltage at one of the thermopiles. The thermopile voltage was stored using a Tektronix TDS3000B Digital Oscilloscope. As an illustration, measurement results obtained for A-type sensor with  $d_{n-Si} = 10.5 \mu\text{m}$  are presented in Figure 6. Based on the analysis of the transient response of the sensors with different membrane thicknesses it was concluded that the thermal time constant assumes a value in the (4 – 5) ms range.

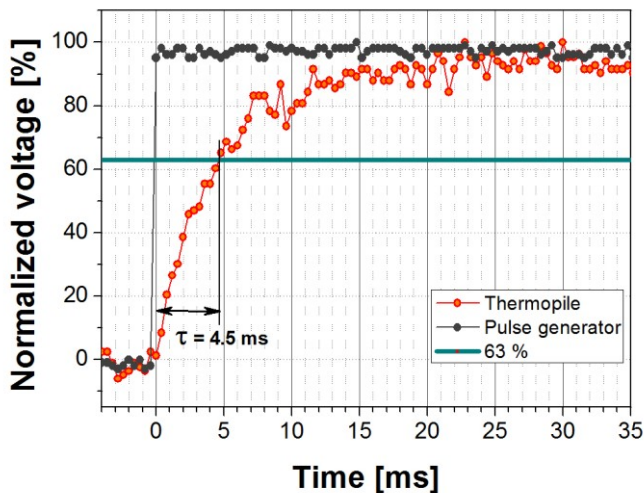


Fig. 6. Normalized input voltage generated with Pulse Generator and time response measured at one thermopile of A-type sensor with  $d_{n-Si} = 10.5 \mu\text{m}$ .

#### IV. CONCLUSION

It can be concluded that ambient temperature does not exert a strong influence on the thermal time constant of the sensor. Simulation results are in good agreement with the experimental data obtained for sensors with various residual n-Si thicknesses. The influence of gas pressure and gas type on the thermal time constant is increasing with a decrease of residual n-Si thickness. Among gases of interest, helium has the strongest influence on the thermal time constant of thermopile sensors due to the fact that it is almost 5 times better thermal conductor compared with nitrogen and carbon dioxide.

The same conclusions are valid for A-type structures. Based on the results presented in [4], a somewhat lower value of the thermal time constant can be expected for the same thickness of residual n-Si in the case of A-type structures.

Gas type detection could be performed based on measurement of the thermal time constant of our multipurpose sensors. This analytical approach is generalized and flexible enough to be implemented for the analysis of the transient behaviour of thermopile-based sensors when used for different applications. Important conclusions regarding transient response can be deduced which should enable optimization of sensor structure for a specific application.

#### ACKNOWLEDGMENT

The authors would like to thank Mag. Sci. Dragan Tanasković from the ICTM-CMT for the photographs of the sensors.

#### REFERENCES

- [1] G. C. M. Meijer, A. W. Herwaarden, *Thermal Sensors*, IOP Publishing, Bristol, 1994.
- [2] M. Bugnacki, J. Pyle, P. Emerald, "A Micromachined Thermal Accelerometer for Motion, Inclination, and Vibration Measurement", *Sensors*, June 2001, Available: <http://archives.sensorsmag.com/articles/0601/98/index.htm>.
- [3] Xensor Integration, Available: <http://www.xensor.nl/pdf/files/sheets/tcg3880.pdf>.
- [4] D. Randjelović, A. Petropoulos, G. Kaltsas, M. Stojanović, Ž. Lazić, Z. Djurić, M. Matić, "Multipurpose MEMS Thermal Sensor Based on Thermopiles", *Sens. Actuat. A-Phys*, vol. 141, pp. 404-413, 2008.
- [5] D. Randjelović, Z. Djurić, A. Petropoulos, G. Kaltsas, Ž. Lazić, M. Popović, "Analytical modelling of thermopile based flow sensor and verification with experimental results", *Microelec. Eng.*, vol. 86, pp. 1293-1296, 2009.
- [6] D. Randjelović, V. Jovanov, Ž. Lazić, Z. Djurić, M. Matić, "Vacuum MEMS Sensor Based on Thermopiles – Simple Model and Experimental Results", in *Proc. 26th Int. Conf. MIEL 2008*, Niš, Serbia, 2008, Vol 2, pp. 367-370.
- [7] A. G. Kozlov, "Optimization of thin-film thermoelectric radiation sensor with comb thermoelectric transducer", *Sens. Actuators*, vol. 75, pp. 139-150, 1999.
- [8] P. Eriksson, J. A. Anderson, G. Stemme, "Thermal Characterization of the Surface Micromachined Silicon Nitride Membranes for Thermal Infrared Detectors", *IEEE J. Microelectromech. Syst.*, vol. 6, pp. 55-61, 1997.

# Position Measurement over Wide Range by Simultaneous Use of Low and High Coherence Light Source

Miloš C. Tomić and Zoran V. Đinović

**Abstract**—In this paper we propose and experimentally demonstrate a new technique for position/displacement measurement using fiber optic interferometry. We simultaneously employ a low- and a high- coherence light source in the same opto-mechanical configuration. The low coherence signal was obtained using a Fizeau receiving interferometer, implemented as an optical glass wedge, accompanied by a linear CCD array. Combining low- and high-coherence parts was possible because we showed that the accuracy of low-coherence based position measurement was better than 50 nm, less than the high coherence signal periodicity. We verify the method in the dynamic range of low-coherence measurement of about 100  $\mu\text{m}$ , while the accuracy of the high-coherence part was about  $\pm 1$  nm. Thus, the method provides more than 100,000 measuring points. The advantages of this sensing technique include absolute position/displacement measurement in a large dynamic range with nanometer accuracy.

**Index Terms**—fiber-optics, interferometry, measurement, sensors

*Original Research Paper*  
DOI: 10.7251/ELSI1519074T

## I. INTRODUCTION

POSITION and/or displacement measurement is probably the most often measured physical parameter in measurement science and technology. There are many different approaches (e.g. inductive, capacitive, ultrasound, etc.), which have found application in industrial sensors and transducers. However, the use of certain sensor/transducer type is always determined with environmental conditions at the measuring place. A big challenge is the measurement of physical and chemical parameters in harsh environments, or those characterized with specific technical requirements, where sensors must ensure electro-magnetic induction (EMI) immunity, be explosion proof, corrosion resistant, have small size and mass, etc. Of course, it is assumed that such devices have high accuracy,

Manuscript received 08 November 2015. Received in revised form 15 December 2015.

This work was financially supported by the Austrian Science Fund (FWF) within the framework of the Project L139-N02 “Nanoscale measurement of physical parameters” and ACMIT GmbH.

M. C. Tomić is with the School of Electrical Engineering, University of Belgrade, Belgrade, Serbia (e-mail: milos.tomic@gmail.com).

Z. V. Đinović is with ACMIT GmbH, Wiener Neustadt, Austria. (e-mail: zoran.djinovic@acmit.at).

large dynamic range, high measuring rate, high reliability, etc. Beside in common processing industry, such features are very often encountered in aircraft and automotive industry and particularly in medicine.

Optical sensors generally can fulfill most of the aforementioned demands. However, the use of bulk optical components, such as mirrors, lenses, gratings, etc. is unavoidably accompanied by impairment of the initial sensor performance due to contamination build-up and opto-mechanical misalignment caused by thermal and vibrational influences. Fiber-optic sensors, being all-dielectric, very flexible and small in dimensions, offer a number of advantageous solutions capable to overcome these drawbacks [1, 2]. Such an example is the application of fiber-optic sensing technology in optical coherence tomography (OCT), as a novel imaging technology in modern clinical laboratories. OCT provides high-resolution cross-sectional images of the internal microstructure of living tissue. In the skin and other highly scattering tissues, OCT can image small blood vessels and other structures as deep as 1–2 mm beneath the surface with axial resolution of  $< 15\mu\text{m}$  [3, 4]. Although this resolution is one to two orders of magnitude higher than that of a conventional ultrasound image, there is still room for improvements. At the heart of the system is a fiber-optic position sensor based on low-coherence interferometry with mechanical scanner on the receiving side that limits overall sensitivity of OCT. Our approach, presented in this study, generally aims toward optimization of fiber-optic position/displacement sensor, bearing in mind practical applications such as OCT.

Basically, interferometry is one of the most accurate measuring techniques for position/displacement measurement in subnanometer range. A conventional interferometric sensor utilizes a monochromatic, high-coherence light source such a laser or laser diode. However, the output signal of such a sensor is periodic in nature and consequently limits the unambiguous measuring range. This range can be extended by some accompanying techniques such as the two-wavelengths interferometry, tunable light source or quadrature signals [5–7]. Nevertheless, in all these cases, periodicity of the cosine function causes ambiguity in absolute position determination with a period of quarter of wavelength. It can be overcome by the conventional fringe-counting technique, but the initialization problem still remains. Low-coherence interferometry [8, 9], on the other hand, overcomes the problem of absoluteness and initialization since it generates an

interferometric pattern with Gaussian shape by mechanical scanning of the optical path at the receiving side. The absolute position can be unambiguously determined with an accuracy of several tenths of nanometers by using some of techniques for finding the center of coherence zone, i.e. the maximum of Gaussian function. However, every movable part in the sensing configuration, either for optical path scanning or/and phase-shifting, is a permanent source of instabilities and inaccuracies. Recently, Zhao et al. [10] reported on a novel absolute displacement measurement technology which completely excludes scanning. It is based on the wavenumber spectrum of low coherence interferometry with a resolution of about 6 nm in a measuring range of 50  $\mu\text{m}$ . Wang et al. [11] achieved measurement resolutions below 1 nm in a range of 6 mm by multiplexing low- and high-coherence fiber-optic interferometric system, also without mechanical scanning.

In this paper we employ both techniques at the same time using a single measuring interferometer and avoiding a mechanical scanner. On the receiving side, we separate the signals belonging to the high- and the low-coherence light sources. It is achieved using different wavelengths for low- and high-coherence sources. The main advantages of this novel technique are relatively low resolution demands in every single evaluation step, either low- or high-coherence. A long-term stable and accurate sensing system is realized by the electronic interrogation of the low-coherence signal by 1D CCD. The high-coherence signal is captured by a photo diode.

## II. PRINCIPLE OF OPERATION

The proposed method is based on the simultaneous use of two in principle different interferometric measurement techniques, low- and high-coherence interferometry. The common part in both techniques is the arrangement at the measurement point, where the measured distance acts as a path imbalance (difference) of the two-beam interferometer. The difference between these two methods is on the receiving side.

The intensity of the combined signal of a two-beam interferometer  $I_p$  is equal:

$$I = I_1 + I_2 + 2\sqrt{I_1}\sqrt{I_2} |\gamma_{11}(\Delta L_{12})| \cos(2k\Delta L_{12}) \quad (1)$$

where  $I_1$  and  $I_2$  are the intensities of two beams,  $k$  is the wavenumber,  $\Delta L_{12}$  is the path difference and  $\gamma_{11}$  is the light source coherence degree. The product  $2k\Delta L_{12}$  is the optical path difference of the interferometer.

When the measuring interferometer is illuminated by a high coherence source, i.e. if  $|\gamma_{11}(\Delta L_{12})| \approx 1$ , the detection is made by a simple intensity detector. The path difference (i.e. the position) can be measured with a very high precision, especially in the vicinity of the midway between the top and the bottom of the cosine waveform. In order to cover the whole range of one cosine period, more complicated schemes can be used [5-7]. These are mainly based on generation of so called quadrature signals. For instance, one of these methods employs a 3x3 fiber-optic directional coupler [7]. However, in all these cases, the periodicity of the cosine function causes ambiguity in the absolute position determination within the quarter-wavelength period. It can be overcome by the ordinary

fringe counting technique, but the initialization problem still remains.

On the other hand, when the measuring interferometer is illuminated by a low coherence source, i.e. when  $\Delta L_{12}$  is large enough that  $\gamma_{11}(\Delta L_{12}) \approx 0$ , finding the path difference is more complicated. A second interferometer on the receiving side, the so-called receiving interferometer, should be used. In this way the absolute position can be determined using some of the techniques for finding the center of the coherence zone [12].

In this paper we employ both techniques at the same time, using the same measuring interferometer. On the receiving side, we should be able to separate the signals belonging to the high- and the low-coherence light source. It can be achieved using different wavelengths for two sources, or by fast light switching so that the only one is emitting at one moment. To avoid transient and temperature effects, it is the best practice to utilize fiber optic switches.

We can determine the phase angle of the measuring interferometer  $\varphi_{HC}$  at some instant, starting from the high-coherence signal value and knowing the signal history. The knowledge on the history of the signal changes is necessary because we should always know the interferometric maximum and minimum, in order to determine the inverse function of (1). The measured distance  $D_{HC}$  is directly proportional to the phase angle  $\varphi_{HC}$  by

$$D_{HC} = \varphi_{HC} \cdot \frac{\lambda_{HC}}{4\pi} \quad (2)$$

where  $\lambda_{HC}$  is the wavelength of the high-coherence light source. An additional complication arises from the fact that the cosine function has an additional ambiguity inside the full angle of  $2\pi$  radians: an angle  $\alpha$  and an angle  $(2\pi - \alpha)$  produce the same photodetector signal. Thus, the periodicity of the distance measured by a high-coherence signal, using a single photodetector, equals to a quarter of the employed wavelength.

The position obtained using a low-coherence source is represented by a continuously changing variable, which corresponds to the maximum of the Gaussian envelope of the interferometric signal maxima. This signal is produced by either a spatial pattern, usually a set of parallel fringes, detected by a CCD sensor, or by a photodiode signal in systems employing mechanical scanning. Generally, mechanical scanning techniques have some drawbacks such as low speed and mechanical instabilities which we avoided in this paper. The best choice by far for the receiving interferometer, capable to overcome the aforementioned drawbacks, is a glass wedge, suitable positioned and firmly fixed to the CCD linear array. If the wedge angle is  $\theta$ , the intensity along the CCD line in the  $x$  direction is

$$I = I_1 + I_2 + 2\sqrt{I_1}\sqrt{I_2} |\gamma_{11}(\Delta L_{12} + x \sin \theta)| \cos(2k(\Delta L_{12} + x \sin \theta)) \quad (3)$$

The coherence degree reaches its maximum of unity when its argument is equal to zero; the corresponding position along the CCD array is  $Xc$ :

$$\Delta L_{12} + x n_W \sin \theta = 0 \rightarrow x = \frac{-\Delta L_{12}}{n_W \sin \theta} \equiv X_C \quad (4)$$

where  $\theta$  is the wedge angle and  $n_W$  is the index of refraction of the wedge glass.

It is evident from (4) that the optical path difference  $\Delta L_{12}$  can be determined from the position along CCD where the interferometric fringes have the maximal contrast,  $X_C$ . Moreover, the exact position of  $X_C$  is the local maximum of intensity, because of the cosine member in (3).

Let us suppose now that we are continuously changing the optical path difference, causing that the center of the low-coherence interferogram is moving along the CCD line, while we are at the same time monitoring the high-coherence phase angle  $\varphi_{HC}$ . In this way, we can establish the list of successive positions  $X_C = X_1, X_2, \dots, X_N$ , where the phase angle  $\varphi_{HC}$  abruptly changes its value from  $\pi$  to zero. This procedure is illustrated in Fig.1.

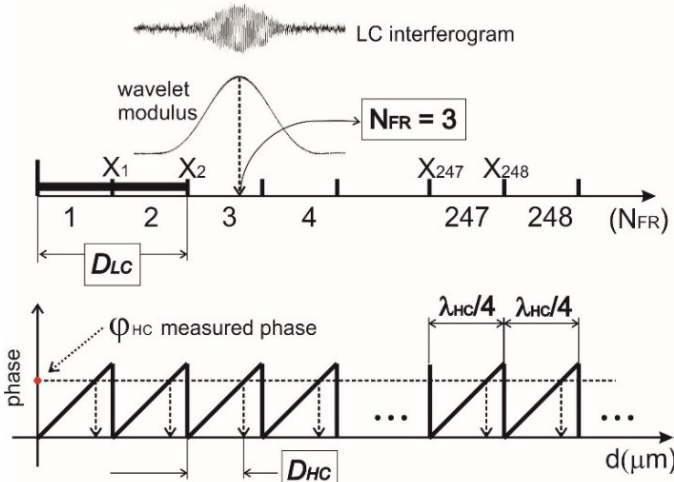


Fig. 1. Principle of interferometric measurement of distance simultaneously using low and high coherence light sources

We now define a set of successive intervals along the CCD array; the intervals are limited by the list members in such a manner that, for instance, the interval  $N_{FR}=247$  is between  $X_{248}$  and  $X_{249}$ , see Fig. 1 top.

In the measurement method we are proposing here, we firstly find the so-called low-coherence part of the measured distance  $D_{LC}$ . Then, employing suitable signal processing, we calculate the position of the interferogram maximum –  $X_C$ . Further, the serial number of the CCD interval, corresponding to  $X_C$  is determined. This number –  $N_{FR}$ , corresponds to the number of the whole high-coherence interferometric fringes from the system zero point. The low-coherence part  $D_{LC}$  is equal to

$$D_{LC} = (N_{FR} - 1) \cdot \frac{\lambda_{HC}}{4} \quad (5)$$

Finally, the measured distance  $D$  is equal to the sum of the distances determined from the low- and the high-coherence interferometric signals:

$$D = D_{LC} + D_{HC} = \frac{\lambda_{HC}}{4} \cdot (N_{FR} - 1 + \frac{\varphi_{HC}}{\pi}) \quad (6)$$

Thus, as seen from (6), we need to determine the two values: one from the low-coherence interferogram –  $N_{FR}$ , and another, from the high-coherence interferogram –  $\varphi_{HC}$ .

The first one assures a very large dynamic range of measurement. The range depends primarily on the CCD length and the receiving interferometer wedge angle.

The second value, the high-coherence phase angle, brings high precision to the measurement, limited mostly by the signal-to-noise ratio of the high-coherence interferogram.

The total accuracy depends essentially on our ability to accurately find the true serial number of the interval, i.e. on the signal-to-noise ratio of the low-coherence interferogram and the coherence length of the low-coherence source. It is obviously required that the uncertainty of finding the position of low-coherence interferogram maximum must be far better than a quarter of high-coherence wavelength.

### III. EXPERIMENT

In Fig. 2 we present a block scheme of the main sensing configuration, based on a Fizeau interferometer illuminated by two light sources of different degrees of coherence. These two sources, one of which emits low-coherence light and the other high-coherence, have also different wavelengths. A pigtailed low-coherence source LCS (superluminescent diode at 850 nm) is connected via two 1x2 fiber-optic couplers (FOC1, FOC3) to one of the input arms of the central 2x2 fiber-optic coupler (FOC4). The silicon photodiode Pd1 is used to monitor the optical power of LCS, using a part of the radiation taken from LCS by FOC1. In the same manner, a high-coherence light source HCS (solid-state laser coupled to the single mode 4/125μm fiber, at 1064 nm) is connected to the same input arm of the FOC4 coupler via a pair of 2x1 couplers. An InGaAs photodiode Pd2 is used to monitor the optical power of HCS, through FOC2. The high- and the low-coherence radiation is combined using the third 2x1 coupler FOC3.

One output arm of FOC4 is directed toward the mirror M which acts as a movable target. The second output arm of FOC4 is immersed in the index-matching gel (MG), in order to suppress back-reflection from the free fiber end. The sensing interferometer of Fizeau type is formed from the fiber end and the mirror M. The gap between these two surfaces –  $\Delta L$  is the distance we want to measure in this experiment.

The low- and the high-coherence light signal are backreflected at the same time, along the same path, from the fiber end and the mirror. The four reflected waves are combined in the coupler FOC4 and outputted at its second “input” arm. This arm is connected to FOC5, another 1x2 fiber-optic coupler, which splits the four combined beams into two halves.

Since we want to separate the high- and the low-coherence signals, which have different wavelengths, ideally FOC5 should be a wavelength-division-multiplexer (WDM) coupler. However, to be detectable by an ordinary CCD detector, the wavelength of LCS has to be around 850nm. Since the laser is at 1064 nm, and could be at 1310 nm or 1550 nm, this kind of single-mode WDM couplers is not readily available.

In the detection part of the system, another InGaAs photodiode Pd3 is employed for the detection of high-coherence radiation. The low-coherence part of radiation, being at a shorter wavelength, is eliminated by an optical highpass or bandpass filter (LPF) placed in the front of the photodetector. The other arm of FOC5 is directed towards the optical stack intended for low-coherence interferometric demodulation. The stack is composed of a lens, an optical wedge and a linear CCD array. The lens is used to collimate the cone of radiation emerging from the fiber end. The optical wedge is acting as a receiving interferometer of Fizeau type. The CCD array should have as many pixels as possible, those itself should be as small as possible. We used the Panavision CCD linear image sensor ELIS-1024, with 1024 pixels of effective size  $7.8 \mu\text{m} \times 125 \mu\text{m}$ . There has been no need for a lowpass optical filter in front of the CCD, because the CCD silicon material is insensitive to wavelengths longer than  $1 \mu\text{m}$ .

We fabricated a series of glass wedges, with different wedge angles, lengths and thicknesses, as custom designed components with Casix [13]. The wedge angles of  $0.5^\circ$ ,  $1^\circ$  and  $2^\circ$  were manufactured, with lengths of 10 and 25 mm, and with widths of 3 mm and 0.5 mm. The starting thickness, at the wedge, was generally made as small as possible (about  $100 \mu\text{m}$ ). All experiments have been performed by the fiber-optic sensing configuration depicted in Fig. 2, using a wedge with an angle of  $0.5^\circ$  as the receiving interferometer.

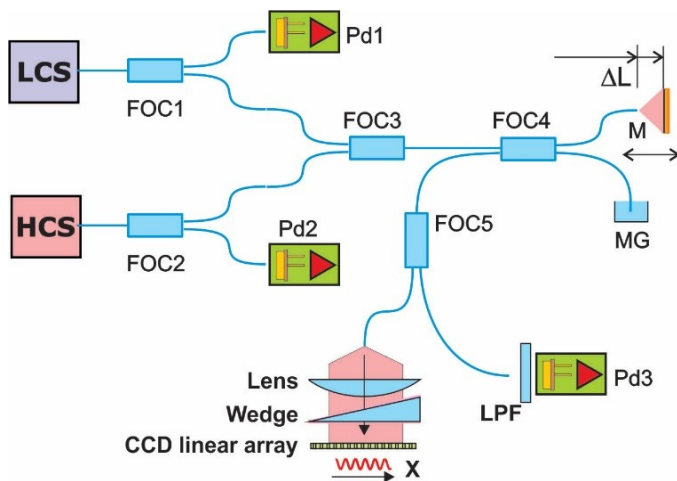


Fig. 2. Experimental configuration for interferometric distance measurement: HCS-high-coherence source, LCS low-coherence source, FOC1-5 – fiber-optic couplers, Pd1-3 photodiodes, LPF-high-pass filter, MG-index matching gel, M-movable mirror acting as target.

We have been using arc splicing to connect all couplers, in order to suppress the phenomenon of back-reflection noise from possible fiber gaps.

An overall view of the sensing part of the measuring set up is presented in Fig. 3. It is composed of a linear DC motorized stage – a Thorlabs production, equipped with an encoder for the position reading with resolution of about 40 nm (not accuracy!). The DC motor is driven by a PI (Physical Instruments) PCI card and software. A PZT transducer with a

dynamic range of about  $10 \mu\text{m}$  is firmly fixed to the mechanical stage. The PZT transducer is driven by a high voltage amplifier, in order to produce small AC displacements for phase angle reading calibration. An aluminum mirror of 5 mm in diameter was glued to the tip of the PZT transducer. The sensing fiber end was firmly fixed by a standard fiber-optic cannula made of brass in front of the mirror. Measured value was the fiber-optic end vs. mirror distance.

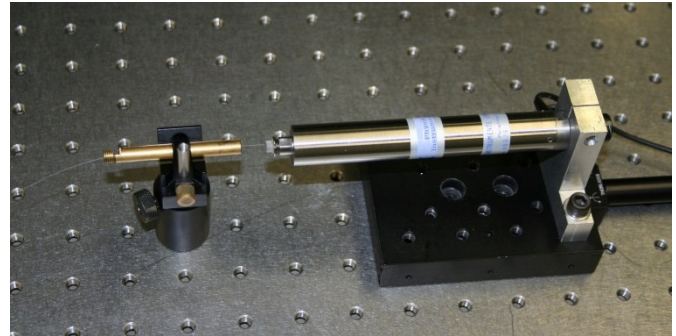


Fig. 3. The sensing Fizeau interferometer: the sensing fiber arm (left) in the brass cannula positioned against Al mirror, mounted on the PZT transducer and DC motorized stage (right)

Large displacements, in the range of  $100 \mu\text{m}$ , were performed by the DC stage. The signal showing the stage position and other signals from photodiodes and CCD array were captured by a National Instruments acquisition card.

The high-coherence signal has continuously been capturing during all measurement time. The low-coherence signal, i.e. particular linear images, has been captured at the discrete moments, after moving the sensing mirror to the new measurement position. The low- and the high-coherence signal acquisition was strictly synchronized in time.

The experiments showed that it was not too difficult to align the parts; the interferometric signals were substantially stable and relatively immune to external vibrations and acoustic disturbances. Temperature effects were also negligible, providing that the joint between the glass wedge and the CCD device was made without any glue (we used the mechanical parts made of MACOR ceramic).

The glass window that covers the CCD surface is factory-assembled and cannot be easily removed. Consequently, it was impossible to bring the glass wedge into a closer contact with the CCD surface, as required for a high visibility of the interferometric fringes. It caused a relatively poor signal-to-noise ratio of the low-coherence signal, increasing the processing time and the measurement uncertainty.

The most important conditions for maintaining a reliable connection between the high- and low-coherence parts of the measurement are simultaneous detection and mechanical stability of all receiving interferometer parts, especially between the glass wedge and the CCD detection array.

#### IV. RESULTS AND DISCUSSION

In Fig. 4 we present a screenshot of a typical raw low-coherence signal, recorded in one particular mirror position. This signal has a characteristic shape of interferometric low-

coherence Gaussian-enveloped pattern, superimposed upon a quasi-DC signal, reflecting the light intensity distribution over the CCD array. In a single experiment, we usually acquired about 20-40 interferometric patterns like this one. Every CCD pattern has been digitized as a set of 1024 12-bit values.

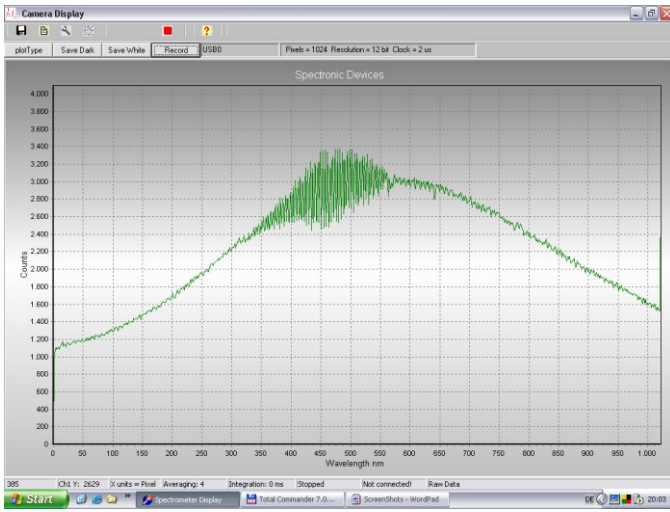


Fig. 4. Screen shot of a typical low-coherence signal captured by 1D CCD EPLIS 1024 sensor array

The raw high-coherence signal, captured by the InGaAs photodiode, is presented in Fig. 5. The shape of the signal clearly reveals a set of discrete positions of the moving mirror during the experiment. These signal portions are bounded by sudden phase changes, caused by the mirror shifts. The mirror has been moved using DC motorized stage, shifting in discrete steps of 4  $\mu\text{m}$ , over the range of about 90  $\mu\text{m}$ .

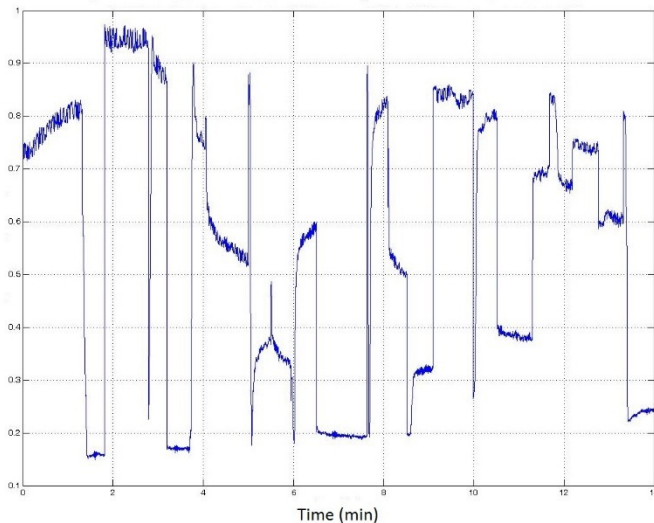


Fig. 5. Raw high-coherence signal during 23 mirror shifts by 4  $\mu\text{m}$ , captured continuously in time of the experiment.

The signal processing of the low coherence signal, performed off-line using Matlab software packet [14], starts with normalization using the CCD signal obtained from the non-interferometric pattern. In this way the influence of non-uniform distribution of optical intensity across the sensing line is eliminated. Then, we applied wavelet transformation, using

the complex Morlet 6-10 continuous wavelet [15], which corresponds to the shape of the low-coherence interferogram. The modulus of the appropriate transformation scale was fitted by Gauss function, where the fitting parameter was the position of the center. The half-width and the maximum of Gauss function, being dependent on the low-coherence source coherence length and power, are invariable in the measuring system and known. The best-fit Gauss center is our low coherence position  $X_C$ , from (4). The values obtained in this way, transformed according to (4), from  $X_C$  to low-coherence positions, are presented and labeled on the right side of the graph in Fig. 6. These positions show a linear trend over the whole 90  $\mu\text{m}$  range, reflecting the way of the real movement of the mirror in the sensing interferometer.

The high-coherence signal was transformed to a phase angle using the usual interferometry inverse-cosine transformation, based on (1), where the maximum and minimum of the high-coherence signals are unchangeable and known. The calculated phase angle walks in the frame of about 250 nm, corresponding to 1/4 of the laser source wavelength. These values, taken in discrete time moments, are shown and labeled on the left side of the graph in Fig. 6.

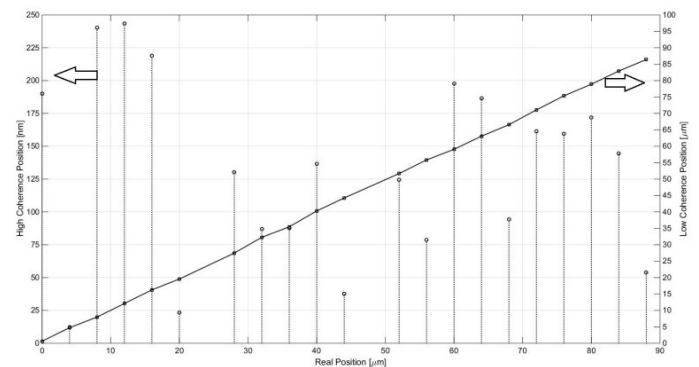


Fig. 6. Combined processed high- and low-coherence signal in the complete measurement range, from zero to 90  $\mu\text{m}$ . The high-coherence signal is calculated from the phase angle taken at moments of capturing the low-coherence signal.

The exact measured position can be calculated by adding the path difference belonging to this phase angle  $\varphi_{HC}$  to the bottom of  $\lambda_{LC}/4$  ruler, obtained from the low-coherence position  $X_C$ , as explained in Section II. A comparison of calculated and the settled position is not shown here because the accuracy of reading the DC motor position was not good enough for this purpose. This part of method verification is left for the experiments based on a specially prepared step-target, characterized in advance by a profilometer.

The ultimate request for the accuracy of the method is the determination of unambiguity of the absolute target (mirror) position out of the low-coherence signal. For this purpose we recorded the low-coherence signal during about eight minutes, while the mirror was steady in a certain position. The pixel position of center of coherence zone, calculated by fitting using Gauss function, for 41 successive measurements is shown in Fig. 7. The pixel number is not a counting number because the fitting output is a continuous value.

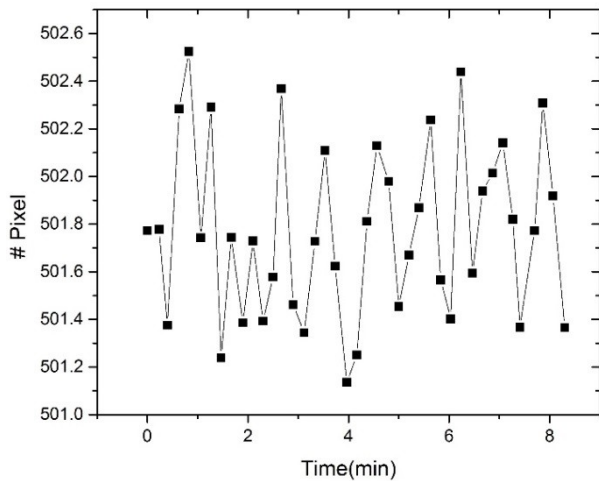


Fig. 7. Change of position of the coherence zone center on CCD, obtained by wavelet signal processing, during about 8 minutes in steady state condition. The position is given in the pixels numbers, used as continuous variable in Gaussian fitting.

The connection between the pixel number value and the real position can be found from the slope of the low-coherence curve in Fig. 6, or from (4). The slope in this experiment was about 100 nm/pixel. The histogram of deviations from the steady position, calculated from 8-minutes data shown in Fig. 7, is presented in Fig. 8.

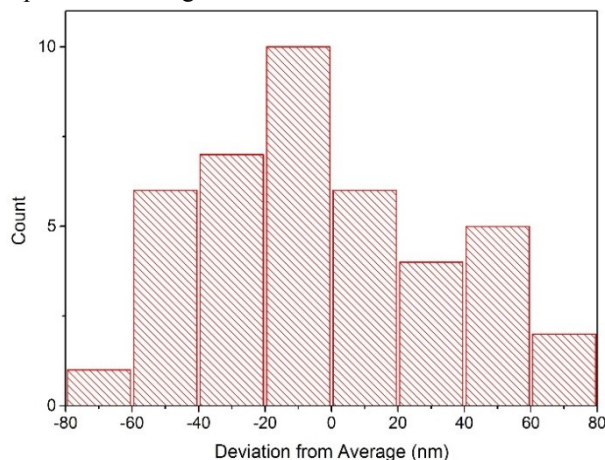


Fig. 8. Histogram of data from Fig.7. transformed into distance units, using the pixel/distance slope found from the low coherence scan presented in Fig.6, Short term repeatability of measurement, indicating the precision of low coherence measurement is about 44 nm (standard deviation).

The standard deviation from the steady – average position is calculated from the data shown in Fig. 8. The deviation is about 44 nm, which means that the probability of misreading the serial number of  $\lambda_{HC}/4$  interval is about 0.0065. This result is obtained for a 1064 nm high-coherence wavelength and for a position in the middle of  $\lambda_{HC}/4$  interval. The probability of wrong determination of the interval number rises as the calculated low-coherence position approaches the edge of interval, until the unacceptable value of 0.5 is encountered at its very edge. The proximity of the edge can also be recognized if the high-coherence phase angle is close to zero or  $\pi$ . In these cases, additional attention should be paid and the process of determination of the interval serial number should take into account the signal continuity.

## V. CONCLUSION

A new technique for position/displacement measurement has been proposed. The technique simultaneously uses fiber-optic low- and high-coherence interferometry in the same sensing configuration without any scanning mechanism on the receiving side. In this way a nanometer scale accuracy of about  $\pm 1$  nm and an absolute measurement of target position in a wide dynamic range of about 100  $\mu\text{m}$  is assured and experimentally confirmed. Hence, the technique provides more than 100,000 measuring points in the examined configuration, although much more can be achieved, even more than one million, using a CCD array with a larger number of pixels and a longer glass wedge.

## ACKNOWLEDGMENT

This work was financially supported by the Austrian Science Fund (FWF) within the framework of the Project L139-N02 “Nanoscale measurement of physical parameters” and ACMIT GmbH.

## REFERENCES

- [1] K.T.V. Grattan, T. Sun, “Fiber optic sensor technology: an overview”, *Sensors and Actuators*, vol. 82, pp. 40-61, May 2000
- [2] E. Udd, An overview of fiber-optic sensors, *Rev. Sci. Instrum.*, vol. 66, pp. 4415-4030, Aug. 1995
- [3] J. G. Fujimoto, J. M. Schmitt, E. A. Swanson, I.-K. Jang, “The development of OCT”, in *Cardiovascular OCT imaging*, I.-K. Jang Ed. New York: Springer 2015, pp. 1-21
- [4] J. M. Schmitt, “Optical coherence tomography (OCT): a review, *IEEE Journal of Selected Topics in Quantum Electronics*, vol. 5, pp.1205-1215, Jul./Aug.1999
- [5] A.D. Kersey, A. Dandridge, W. K. Burns, “Two-wavelength fiber gyroscope with wide dynamic range”, *Electron. Lett.*, vol. 22, pp. 935-937, Aug. 1986
- [6] H. Kikuta, K. Iwata, R. Nagata, “Distance measurement by the wavelength shift of laser diode light”, *Appl. Opt.*, vol. 25, pp. 2976-2980, Sep. 1986
- [7] D. A. Brown, C. B. Cameron, R. M. Keolian, D. L. Gardner, S. L. Garrett, “A symmetric 3x3 coupler based demodulator for fiber optic interferometric sensors”, *SPIE 1584, Fiber Optic and Laser Sensors IX*, 1991, pp. 328-335
- [8] Y.-J. Rao, D. A. Jackson, “Recent progress in fibre optic low-coherence interferometry”, *Measurement Science and Technology*, vol. 7, pp. 981-999, Jul. 1996
- [9] M. A. Choma, C. Yang, J. A. Izatt, “Instantaneous quadrature low-coherence interferometry with 3 3 3 fiber-optic couplers”, vol. 28, pp. 2162-2164, Nov.2003
- [10] K. Zhao, F. Xie, S. Ma, Y. Wang, L. Chen, “A novel absolute displacement measurement technology based on wavenumber resolved low coherence interferometry”, *Optics & Laser Technology*, vol. 75, pp. 34-39, Dec. 2015
- [11] Y. Wang, F. Xie, S. Ma, L. Chen, “Remote and high precision step height measurement with an optical fiber multiplexing interferometric system”, *Optics and Lasers in Engineering*, vol. 66, pp. 52-57, Mar. 2015
- [12] M. C. Tomic, J. M. Elazar, Z. V. Djinic, “Low-coherence interferometric method for measurement of displacement on a 3x3 fiber-optic directional coupler”, *J. Opt. A: Pure Appl. Opt.*, vol. 4, pp. S381-S386, Nov. 2002
- [13] <http://www.casix.com/> (assessed 08.11.2015)
- [14] MATLAB and Statistics Toolbox Release, The MathWorks, Inc., Natick, Massachusetts, United States, 2012
- [15] A. Teolis, “Computational signal processing with wavelets”, Birkhauser, Boston, 1998, pp.65-66

# Improving the methodology of main power equipment choice for the gas turbine plants

Evgeny Lisin, Wadim Strielkowski, Ivan Komarov, Ivan Garanin

**Abstract** - Our paper considers the problem of economic substantiation of the choice of the main power equipment at the stage of functional studies of investment projects in conditions of uncertainty and incompleteness of initial data. As a solution to the designated problem we suggest using the method of the best equipment for gas turbine power plant choice. The method is based on an optimality criterion of power equipment choice which allows us to determine the best solution for the gas turbine from the perspective of capital and operating costs minimizing.

**Index Terms** - Gas Turbine Power Plant, Main Power Equipment, Investment Project, Statistical Analysis, Capital Cost, Operating Cost.

*Original Research Paper*  
DOI: 10.7251/ELSI1519080L

## I. INTRODUCTION

THE investment project in the energy sector can be defined as an endeavor focused on creation, development of power facilities, representing a system of objectives, resources, organizational and managerial activities for their implementation. The life cycle of a typical investment project in the energy sector (IEP) consists of 3 main stages: pre-investment, investment, and operation.

The pre-investment stage is a preparatory stage of IEP, during which the investor gets detailed information about the feasibility and economic efficiency of the energy project. According to the results of pre-investment studies, the decision

on expediency of the project realization is made. The key document of pre-investment studies is a feasibility study (FS).

Feasibility study represents the document containing reliable information about technical, financial, commercial, social, environmental assumptions of the investment project implementation, as well as evaluating the viability and economic efficiency of the project. The feasibility study is typically composed of 10 chapters. Each Chapter focuses on critical aspects of the project without consideration of which the answers to key questions, including the feasibility and economic viability of the project will not be received. Some of the most important aspects of the project, which are analyzed in the feasibility study of the IEP can be highlighted:

- power sales: electricity supply planning, forecasting the dynamics of changes in tariffs for electricity supply, the study of the possibility of the station connection to the power grids, a preliminary production schedule;
- fuel supply: determination of the possible volume of fuel and lubricants, forecasting fuel prices, the study of the possibility of generation facilities connection to the fuel source;
- description of the selected energy technologies: defining technical and economic parameters of equipment, estimating costs associated with the equipment operation, evaluation of the required volume of investments for the acquisition, installation and commissioning of the equipment;
- description of the location of the object: determination of the environmental situation at the construction site of the power plant, estimation of costs related with the preparation of the construction area;
- human resources: an analysis of the possibility of attracting qualified staff for the operation of power station, determination of the wages level in the region, assessing the costs of salary fund;
- preparation of investment and operational plans of the project;
- financial analysis and economic evaluation of investment.

According to guidelines for the development of industrial feasibility study prepared by the United Nations Industrial Development Organization (UNIDO), the accuracy of the estimates given in the feasibility study should not be below 10% [1, 2]. It is not possible to obtain such precise estimates without significant labor and financial resources costs.

According to UNIDO, the share of costs for development of feasibility study of the total cost of the investment project may

Manuscript received 13 August 2014. Received in revised form 26 May 2015. Accepted for publication 8 September 2015.

The paper was partially supported by the Ministry of Education and Science of the Russian Federation, research project №26.1795.2014/K.

Evgeny Lisin is with the Department of the Economics and Management of Enterprises, National Research University "Moscow Power Engineering Institute", Krasnokazarmennaya 14, Moscow, Russian Federation (e-mail: lisinym@mpei.ru)

Wadim Strielkowski is with the Faculty of Social Sciences, Charles University in Prague, Smetanovo nabrezi 6, 110 01, Praha 1, Prague, Czech Republic (Corresponding author, Phone: + 420 603 508 627; e-mail: strielkowski@fsv.cuni.cz).

Ivan Komarov is with the Department of the Economics and Management of Enterprises, National Research University "Moscow Power Engineering Institute", Krasnokazarmennaya 14, Moscow, Russian Federation (e-mail: komarovii@mpei.ru).

Ivan Garanin is with the Department of the Thermal Power Plants, National Research University "Moscow Power Engineering Institute", Krasnokazarmennaya 14, Moscow, Russian Federation (e-mail: garaniniv@mpei.ru).

be 1-3% [1, 2]. At an average cost of 6 MW gas turbine power plant of 4.4 million euros, the investor will need at least 0.44 million euros to conduct the feasibility study.

If the feasibility study shows that the investment project will not provide the expected return to the investor according to its rate of return or the payback period is too large, then the investor will have to make adjustments to an existing project or to develop a new project. A negative result obtained by the results of the feasibility study, is aggravated by the fact that the feasibility study is conducted at the stage of investment feasibility study, which is preceded by a significant number of costly stages of preparation of the investment project.

In order to reduce the cost of preparing the investment project, it is necessary to conduct justification of the choice of the best initial parameters for the investment object that requires the solution of optimization problem. [3]

Final economic assessment of IEP is formed from two sides:

- assessment of the external environment of the project;
- assessment of the internal parameters of the project.

The assessment of the external environment of the project includes macroeconomic indicators, indicators of electric power market, the level of life of population, characteristics of tax and environmental legislation.

Assessment of internal parameters of the project is carried out from the perspective of the following factors:

- feasibility: the efficiency of the main equipment, the cost of equipment, fuel consumption, the level of automation of the production process, the cost of electricity for its own needs, the life of the equipment;
- environmental: the choice of flue gas cleaning system, the choice of work of the equipment (open or closed loop);
- financial: the use of the cheapest sources of financing, the choice of the financing scheme, the selection of reliable partners (project participants);
- geographic: selection of the most successful location of the object in terms of proximity to the fuel source, proximity to the point of generation object technological connection and sufficient distance from residential areas [1, 2].

In contrast with the external factors which are given and characterize the economic environment of the project, the internal parameters of the IEP are determined at the stage of pre-investment studies. The cost of investment planning and future economic effect depend on their optimal choice.

Technical and economic parameters of the project are largely determined by the choice of the main power equipment from the position of operational and capital costs minimum. [4]

There are many varieties of gas turbines which differ both in terms of efficiency and cost. Fuel component of gas turbine power plants costs ranges from 65 to 75% of the cost of electricity, the value of the specific fuel consumption is a function of the efficiency of gas turbines [6]. Assessment of the fuel component in the cost can be obtained from the following dependence [4]:

$$C^{FC} = K_n N_T G_{ic} P^{FC} \frac{1}{\eta_{GTU} Q^{FC}}, \quad (1)$$

$C^{FC}$  - the value of fuel costs;

$P^{FC}$  - the price per cubic meter of natural gas;

$Q^{FC}$  - heat of combustion of natural gas (kJ/m<sup>3</sup>);

$G_{ic}$  - installed generation capacity (KW);

$\eta_{GTU}$  - gas turbine efficiency, %;

$K_n$  - conversion factor of units of electrical energy (KWh) into units of heat of combustion (kJ);

$N_T$  - the number of working hours in a year.

It should be noted that, in general, the lower the cost of installation is, the less perfect the technology of production and larger specific fuel consumption per 1 KWh of electric energy are, the cost of electricity production increases. However, the production cost of energy products is also affected by the cost of the installation through the depreciation of the main power equipment [5, 6, and 7]. Optimization problem of selection of generating equipment from the perspective of capital and operating costs minimizing occurs.

Based on the above, one can draw some conclusions and formulate requirements to the method of the equipment choice, which would allow us to justify the choice of the main power equipment at the stage of pre-investment studies:

- choice of the best options for power equipment should be conducted prior to the formation of a feasibility study for the project in order to reduce the cost of preparation of the investment project;
- choice of power equipment must be a solution of the optimization problem according to the principle of minimizing capital and operational costs;
- versatility, sufficient simplicity of the calculations and the possibility of their automation, low time costs should be peculiarities of the methodology.

## II. THE CHOICE OF THE MAIN POWER EQUIPMENT FOR THE GAS TURBINE POWER PLANT

Gas turbine power plant (GTPP) is a high-tech generation object that allows to produce electricity and heat. Gas turbine power plant may have an electric capacity of twenty KW to hundreds of MW. A variant of GTPP, which provide combined heat and power, is called GTPP-CHP (combined heat and power). GTPP-CHP differs from GTPP via gas-water heat exchanger (GWHE) and additional pumps for pumping the water. Hereinafter, we will consider only the power plant with electric power, due to the complication of development of a selection methodology for the GTPP-CHP equipment due to the enlargement of the power equipment.

Gas turbine power plants use natural gas and operate on the basis of thermodynamic Brayton cycle. As part of the gas turbine, typically runs one unit of the main power equipment - gas-turbine unit (GTU), which, in turn, comprises a compressor, a combustion chamber, a gas turbine and an electric power generator. A gas turbine (GT) plant is based on Brighton's open thermodynamic cycle. For normal operation

of the main power equipment GTPP includes additional (auxiliary) equipment [6]:

- electrical equipment unit;
- booster compressor for fuel;
- automated process control system (APCS);
- integrated air-cleaning device;
- Emergency Power Supply Unit;
- firefighting unit;
- ventilation unit of GTU container.

According to the calculations made by the software package PEACE, total capital cost on ancillary equipment does not exceed 12% of GTPP total capital costs. Tables 1 and 2 show the estimates of the cost of GTPP based on GTU of different manufacturers and capacities.

**Table 1: Estimates of the cost of GTPP based on GTU of different capacities**

GTU	Capacity, MW	Efficiency	GTU price, mln \$	The cost of auxiliary equipment, mln. \$	Cost of installation and commissioning work, mln. \$	GTPP total cost, mln. \$
Alstom TB 5000	3,809	25,2	2,4	0,41	0,75	3,56
Siemens SGT-200-IS	6,25	30,3	3,6	0,62	1,13	5,35
Mitsubishi MF 111A	12,83	30,6	6,2	1,13	1,96	9,29
GE LM2000	17,64	34,9	7,9	1,35	2,48	11,73
Siemens SGT-700	29,06	36	11,9	2,03	3,73	17,66
GE 6561B	40,34	32,4	14,2	2,43	4,45	21,08
Siemens SGT-800-50	50,5	38,3	18	3,07	5,64	26,71
RR TRENT 60 WLE	64	41	22,5	3,85	7,05	33,4

**Table 2: Consolidated cost structure at GTPP of different capacities**

GTU	GTU, %	GTPP auxiliary equipment, %	Installation and commissioning work, %
Alstom TB 5000	67,42%	11,52%	21,07%
Siemens SGT-200-IS	67,29%	11,59%	21,12%
Mitsubishi MF 111A	66,74%	12,16%	21,10%
GE LM2000	67,35%	11,51%	21,14%
Siemens SGT-700	67,38%	11,49%	21,12%
GE 6561B	67,36%	11,53%	21,11%
Siemens SGT-800-50	67,39%	11,49%	21,12%
RR TRENT 60 WLE	67,37%	11,53%	21,11%
Average	67,29%	11,60%	21,11%

From the tables above one can conclude that the most of the capital costs of GTPP is the main power equipment (67,3%). It should also be noted that the share of expenses for ancillary equipment, construction, installation and commissioning does not depend on the manufacturer and GTP capacity. This fact is an important feature as it will allow us to ensure comparability condition of the results of the selected power equipment using the developed methodology.

The most common way of comparing two gas turbines with each other in order to solve the problem of choosing the main power equipment is to conduct identical feasibility studies for

different GTU. This approach assumes that a change in the brand and the model of the equipment may affect not only the capital cost of the gas turbine, but other articles of the forecasted cost. However, according to the data shown in the Table 2, the cost structure of units of different manufacturers remains unchanged. Therefore, free choice of equipment will not distort a comparative assessment of equipment.

The second important aspect is the operational efficiency. Operational efficiency is the difference in operating costs arising as a result of the choice of the more efficient equipment.

Selection of equipment for the procedure of comparison should be made from the power equipment of comparable installed capacity. The desire of the investor to build a GTPP of a certain power is based on the analysis of the electricity market and the load schedule. The project power should be required, and the equipment should be loaded. Equipment of comparable capacity will be served by the same number of industrial production personnel (IPP). The number of IPP for GTPP of 12 to 150 MW capacity can be defined according to the regulations of the number of industrial production personnel [2, 8] The feature of the standards is quite a big step in power, within which the number of employees remains the same. The step size is from 10 to 30 MW. This implies that the permissible range of values of GTP capacities should be less than a given range.

As it was shown above, other costs also do not actually change when one changes the brand of comparable capacity equipment. In assessing the cost of energy products other costs are determined by the regulatory method. Other costs are usually 5-7% of the total cost of electricity.

As for the repair costs, then it is necessary to start with two basic parameters of repair of the equipment: the duration of the interval between repairs and the cost of repairs. The analysis of GTU revealed that the installation of similar capacity have identical service life and require the same number of repairs which means that regardless of the choice of equipment repairs will be carried out in a comparable time. This can be explained mainly by corrosion processes in the metal caused by high gas temperatures inside the plant – a property shared by all gas turbine designs. The common term “oxidation” refers to high-temperature oxidation of rotor vanes. The cost of repair of GTU doesn't differ greatly. The fact is that manufacturers of gas turbine equipment operate on the world market in conditions of tough competition. As the power equipment is largely identical, increasing the cost of repairs by the manufacturer leads to lower competitiveness [9, 11].

The remaining cost items - fuel costs and depreciation - characterize operational efficiency. Each installation of the selected capacity interval has different costs depending on efficiency and specific fuel consumption. In turn, the cost of the equipment affects the production cost of energy products through depreciation.

Next, let us make the selection criterion of the main power equipment for GTPP on the basis of parametric functions, characterizing the cost of equipment and its operational efficiency.

### III. DEVELOPMENT OF SELECTION CRITERIA OF THE MAIN POWER EQUIPMENT FOR GTPP

In order to develop methods of choice of the main power equipment statistical analysis of technical and economic characteristics of GTU included in the database CAD Thermoflex was performed in program Statistica. The database consists of 232 units with the capacity from 0.5 to 60 MW (the most common power GTPP in Russian Federation). The study was conducted for the following parameters of power equipment: power, efficiency, shaft speed, compression of air in the compressor, the temperature difference in the turbine, air flow. The correlation analysis has allowed to reduce the number of variables and to establish the main cost factors of this type of power equipment: capacity and the number of shaft revolutions.

After normalization [10] the function of the cost parameter takes the following form:

$$CC'_{GTU} = CC_{GTU} \frac{1}{\sigma}, \quad (2)$$

$CC'_{GTU}$  - capital costs parameter,

$CC_{GTU}$  - GTU cost of the selected interval capacity,

$\sigma = 6,3082$  mln \$ - standard deviation of cost GTU, calculated for a sample of the database Thermoflex.

To obtain the operational efficiency parameter function we will analyze expression 1. Most of the parameters of this function when changing GTU to unit of another manufacturer will remain unchanged. Installed capacity utilization rate, the price of fuel, calorific value, conversion coefficients, the number of work days do not depend on the main power equipment, so equipment changes are not reflected. Only two parameters will change - capacity (within a given interval) and efficiency. Changing the capacity in this case is not important, because it is assumed that the unit will work with a given load, which was originally founded in the IEP as an input. Efficiency remains. It will characterize the change of the fuel component of costs compared to other GTU. Hence, the function of the operational efficiency parameter determination can be written as follows:

$$C'_{GTU} = \frac{1}{\eta_{GTU}}, \quad (3)$$

On the basis of the given parametric functions will form the selection criteria of the best equipment:

$$Z = \mu CC'_{GTU} (C'_{GTU} + \mu CC'_{GTU}) \rightarrow \min, \quad (4)$$

$C'_{GTU}$  - GTU efficiency parameter,

$\mu$  - the share of depreciation,

The criterion of selection of the best equipment consists of two factors: the first factor characterizes the amount of GTU capital costs, the second characterizes operational efficiency of GTU in comparison with other units, taking into account the relationship between the cost of GTU and operating costs through depreciation.

The proposed method for choosing the best power equipment involves cost and operational efficiency calculations, finding the optimization criteria for power equipment of given capacity selection. Equipment with minimum value of the optimization criterion will be economically feasible. To expand the sample in order to compare maneuverable energy equipment, it is proposed to produce calculation on interval data at a given capacity range:

$$[G_{nom}; 1,25G_{nom}] \quad (5)$$

$G_{nom}$  - required nominal generation capacity of the plant.

This range assumes that GTU, the capacity of which can exceed the nominal value for 25%, can provide the required capacity. It is also considered that at 80% the load of the nominal capacity and efficiency does not change. This assumption is partly justified by high maneuverability of GTU, which may reduce the capacity up to 60% of the nominal value without significant losses [11].

For units operating at decreased power, lower GT unit efficiency will translate into a higher operational savings factor which in turn will increase the Z parameter. A higher Z will automatically push the GT unit away from the optimum equipment choice frontier in a specific investment project. Thus, in order to make the primary power plant equipment selection technique more relevant, the operational savings parameter will have to be adjusted to reflect GT unit operating mode. An addendum to the described technique to account for GT utilization pattern is laid out in Chapter 4 of this article.

Nevertheless, the described technique can still be applied successfully without the above-mentioned adjustment. Unadjusted for equipment utilization pattern, the error margin of the resulting estimate will suffer. One should keep in mind however that this wider error margin is only an issue if the output power of a particular unit lies near the right-side boundary of the sample. In this case, the parameter Z will be skewed to the maximum when the output power of GT unit is higher than required. We carried out computations for choosing the optimum power plant equipment design in line with the proposed technique using a test sample of equipment. Our computations did not include an adjustment for GT utilization pattern. Table 3 summarizes findings from these computations.

Based on findings from computations and considering the proposed optimality criterion, the best choice of an equipment unit would be RR 501-KH5, a gas turbine produced by Allison Rolls-Royce, a power systems manufacturer from the UK. One should keep in mind that the electrical power of this GT unit is just 1,64% above the design power. Moreover, it should be understood that RR 501-KH5 is well ahead of its closest competitors in terms of Z. This means that, given the case at hand, the power-generating equipment manufactured by Allison Rolls-Royce is indeed the best choice from the standpoint of TCO minimization and considering that the final result would not be significantly altered if utilization patterns were accounted for. Nevertheless, the adjustment for utilization patterns of power plant equipment making up the sample may become crucial in less obvious cases.

**Table 3: The results of application of the developed method of the main power equipment optimal choice**

GTU	Capacity, KW	Efficiency, %	Costs, mln. \$	Operational efficiency parameter	Cost parameter	Z
Taurus 65-8400	6000	33,1	3,5	3,02114	0,554851	0,17070
RR 501-KH5	6100	38,1	3,4	2,62467	0,5389981	0,14437
RR 501-KB7S	6180	32,4	3,5	3,08642	0,554851	0,17432
SGT-200-1S	6249	30,3	3,6	3,30033	0,5707039	0,19160
Taurus 65-8400	6290	32,7	3,6	3,05810	0,5707039	0,17778
Taurus 70	6295	31,6	3,6	3,16455	0,5707039	0,18386
Taurus 65-8401S	6300	32,9	3,6	3,03951	0,5707039	0,17672
GT6	6 630	32,7	3,7	3,05810	0,5865568	0,18281
SGT-200-1S	6726	31,9	3,8	3,13479	0,6024096	0,19247
GPB70D	6 744	30,6	3,7	3,26797	0,5865568	0,19512
SGT-200-1S	6745	31,3	3,7	3,19488	0,5865568	0,19083
Taurus 70	6844	32,9	3,7	3,03951	0,5865568	0,18172
GPB70	6 930	30,7	3,8	3,25732	0,6024096	0,19985
GPB70	6 930	30,8	3,8	3,24675	0,6024096	0,19921
Taurus 70	7250	32,8	4	3,04878	0,6341154	0,19734
Taurus 70-T10302S	7305	33,5	3,9	2,98507	0,6182625	0,18837
GPB80D	7 410	32,9	4	3,03951	0,6341154	0,19676
URAL 6000	6 000	27,3	3,75	3,66300	0,5944832	0,22129

#### IV. ACCOUNTING FOR EQUIPMENT UTILIZATION PATTERN IN THE TECHNIQUE FOR OPTIMUM SELECTION OF MAIN POWER PLANT EQUIPMENT

As a means of ensuring optimum equipment choice from the standpoint of TCO minimization, the technique described in this article assumes that the sample will be limited to GT units with output power greater than the rated power. This approach covers the entire range of GT unit models that can be fitted technically into a specific investment project. Nevertheless, as already pointed out earlier, efficiency will decline when an oversized GT stays underutilized. The shape of the efficiency-load dependency curve depends on the control mode in place at the GT unit.

Two GT unit control methods available generally are known as qualitative and quantitative. Power is defined as the flow rate of working medium multiplied by useful work:

$$N = GH, \quad (6)$$

G - gas turbine gas flow rate (kg/sec);

H - disposable heat drop in a gas turbine (kJ/kg).

With qualitative control, power is decreased by reducing fuel supply to the combustion chamber (CC) so that useful work (H) also decreases. This control mechanism generally has the side-effect of increasing air flow rate by a certain amount. How much it increases depends on the flow-rate performance of the compressor. The qualitative method is least economical as it entails a significant decline in thermodynamic efficiency due to lower heat input temperature in the cycle.

With the quantitative method, control is achieved by reducing working medium flow within the GT unit (G). This method is implemented technically by installing special devices at compressor inlet to alter the shape of its flow-through part – the guide vane assembly (GVA) and the turning

vane assembly (TVA). The use of GVA alone brings down the flow rate by 30% to 40% relative to the design flow rate.

Fig. 1 shows the fundamental relationship between relative GT unit parameters and changes in output power. Within the range 1 (100% down to 80% of rated load) the GVA closes partially and quantitative control takes effect.

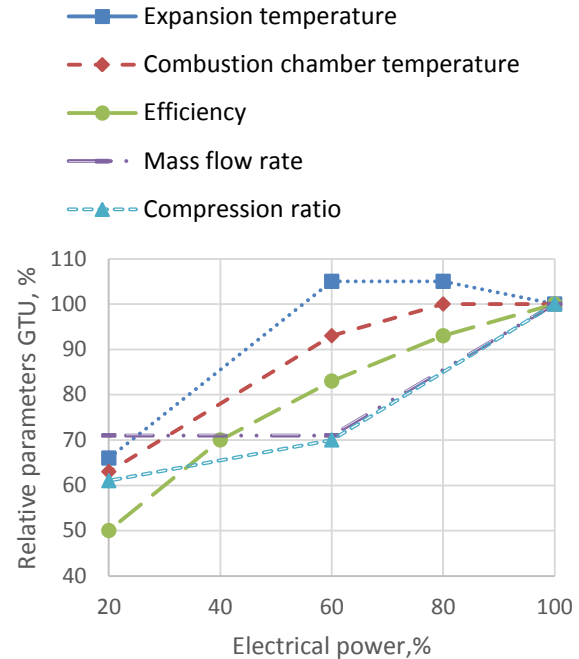


Fig. 1. Relative GT unit parameters as a function of load

Within the range 2 (80% down to 60% of rated load), fuel supply to the combustion chamber is reduced. Combined qualitative and quantitative control takes effect. Finally, within the range 3 (20% to 60% of rated load) the GVA is fully open, fuel supply reduction is used exclusively to achieve reduced output power.

As Fig. 1 illustrates, the decline in GT unit efficiency is least steep within the range 1 where quantitative control applies.

It should also be noted that qualitative control causes the thermal state of hot turbine parts to fluctuate, thereby shortening turbine life, requiring more frequent downtimes and ultimately increasing repair costs for the installation. These two circumstances define the range of GT unit output power which is used for generating the sample. If the output power range were expanded, increased repair expenses within the 20% to 80% control range would invalidate the comparability condition for evaluating individual power plant designs vis-à-vis each other. It is similarly impractical to base design on GT unit operating at efficiencies significantly below the rated value due to significant underutilization of plant capacity.

Let us examine the cause of declining efficiency with quantitative control in greater detail.

The drop in GT unit efficiency with quantitative decrease of output power is caused by a combination of thermodynamic

cycle alterations and a drop in internal efficiency of compressor and gas turbine. Fig. 2 shows the thermodynamic cycle for rated and non-rated output modes.

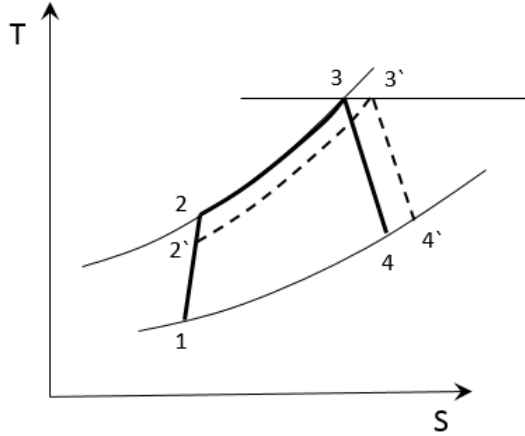


Fig. 2. Quantitative representation of GT unit thermodynamic cycle in rated and non-rated output modes

In Fig. 2 the line 1-2 corresponds to the air compression process in the compressor at full rated output power while 1-2' corresponds to the same process in non-rated output mode. Heat input in the combustion chamber is shown as curve 2-3 and expansion of gases in the turbine corresponds to the line 3-4.

As the air flow rate decreases, the factor  $\pi$  of air compression in the compressor declines following the approximate Stodola-Flügel equation for GT unit:

$$\frac{G}{G_0} = \sqrt{\frac{T_{10}}{T_1}} \sqrt{\frac{\lambda_1^2 \pi^2}{\lambda_{10}^2 \pi_0^2} \frac{1}{1}}, \quad (7)$$

$G, G_0$  - flow rates of the working medium for the rated and derated output modes,

$T_1, T_{10}$  - temperatures of working medium in the rated and non-rated output modes, respectively,

$\lambda$  - hydraulic loss factor,

$\pi$  - compression ratio.

Assuming a fixed temperature at GT inlet, the start of expansion then shifts toward the higher entropy area, leading to increased exhaust temperatures. Heat transfer to the cold source grows per formula (8) while the thermal efficiency of the cycle deteriorates.

$$\eta_t = 1 - \frac{Q_{cs}}{Q_{hs}}, \quad (8)$$

$\eta_t$  - thermal efficiency of the cycle,

$Q_{cs}$  - the amount of heat transferred to a cold source,

$Q_{hs}$  - the amount of heat transferred to the hot source.

Compressor and gas turbine designs have a significant impact on the severity of efficiency drop experienced by these units. Within the assumed non-rating range (100% down to 80% of rated load), the reduction in GT unit efficiency is

explained mainly by thermodynamic factors. Any decline in internal GT and compressor efficiencies would be insignificant in this area, and its contribution to overall decline of GT unit efficiency is marginal [12, 13]. Therefore any further adjustments of the operational savings parameter for GT unit utilization will be based solely on thermodynamic assumptions.

The nature of relationship between GT unit load and its efficiency must be determined prior to augmenting the proposed adjustment technique with an operational savings factor accounting for GT power plant utilization pattern. It would be convenient to use the following relative quantities for clarity reasons: relative efficiency ( $\eta_{rel}$ ) and relative load  $N_{rel}$ . These values can be determined using the formulas (9) and (10):

$$\eta_{rel} = \frac{\eta}{\eta_{rated}}, \quad (9)$$

$$N_{rel} = \frac{N}{N_{rated}}, \quad (10)$$

$N_{rated}, \eta_{rated}$  - output power and efficiency, respectively, in the rated output mode.

Computations with GE Gate Cycle software have been performed to determine the nature of relationship  $\eta_{rel} = f(N_{rel})$ . Gas turbine plant with rated output power within the design range of 6 to 7.5 MW have been selected for computations. The following units have been investigated: Taurus 60 SC, Siemens SGT-200, Taurus 70 SC, Siemens SGT-100 MD. For each of these units, relative efficiency values have been obtained with relative output power non-rated from 1 to 0.8. The resulting data was then used to construct single-factor regression models for every unit under study to describe the drop in relative efficiency caused by a corresponding reduction of relative output power. Fig. 3 shows the results.



Fig. 3. Plot of relative GT unit efficiency as a function of changing relative output power

Fig. 3 shows that the efficiency of these units drops at different rates. This scatter of relative GT unit efficiency values at relative output power of 0.8 can be explained by differences among GT units at hand in technical parameters such as air compression rate in the compressor  $\pi_c$  and gas temperature upstream of the gas turbine  $T_{comb}$ . Table 4 details some technical parameters of GT units considered above.

**Table 4: Selected technical parameters of GT units under study**

GT unit model	Compression rate $\pi_c$	Temperature $T_{comb}$ , °C	GT unit efficiency, %
Siemens SGT-100 MD	14.4	1110	30.3
Siemens SGT-200	12.1	1024	31.3
Taurus 60 SC	12.3	1093	31.5
Taurus 70 SC	15	1121	32.8

Considering that the function for adjusting GT unit efficiency to its load is expected to be applied at an early stage of pre-investment surveys when the feasibility study is ridden with multiple uncertainties, such a function can be obtained by averaging across four functions for the GT units selected above. The obvious drawback of this approach is that the resulting adjustment will be less accurate, however this inaccuracy is minor relative to the general uncertainty of estimates in the feasibility study. Therefore this simplification may be considered well-justified.

Fig. 4 shows the final plot of the function linking relative GT unit efficiency to relative output power for units within the output power range of 5.5 to 7.5 MW.

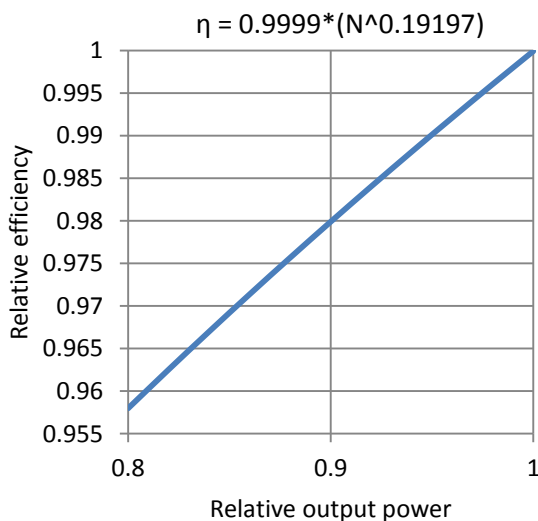


Fig. 4. A plot of relative efficiency as a function of relative output power

The resulting equation makes it possible to integrate utilization pattern considerations in the proposed primary

power plant selection technique and to adjust the function for determining the operational savings factor (11):

$$C'_{gtu} = \frac{1}{\eta_{gtu} \cdot 0.9999 \cdot N_{rel}^{0.19197}} \quad (11)$$

## V. CONCLUSIONS

Our study was concerned with the problem of justifying the choice of primary power plant equipment for investment projects suffering from uncertainty and incompleteness of input data. It has been shown that there is no significant correlation of CAPEX structure with either the output power of GT power plant or the make and model of its primary equipment. We have provided proof that economically sound choice of primary power plant equipment is indeed possible without a full-scale feasibility study, calling just a few economical and technical parameters of equipment into comparison.

Based on our statistical analysis of technical and cost aspects of GT power plant, a technique was proposed for ensuring optimum selection of equipment at functional design study stage of gas-turbine power plant projects. Our technique is grounded in the criterion for assessing the optimality of power plant equipment choice with the goal of arriving at the best GT design solution from the standpoint of CAPEX and OPEX minimization. The technique accounts for uneven utilization patterns of primary power plant equipment.

## ACKNOWLEDGMENTS

The paper was partially supported by the Ministry of Education and Science of the Russian Federation, research project No.26.1795.2014/K.

## LIST OF ABBREVIATIONS AND SYMBOLS

APCS – automated process control system,  
 CAPEX – capital expenditures,  
 CC – combustion chamber,  
 FS – feasibility study of pre-investment stage,  
 IEP – investment project in the energy sector,  
 IPP – industrial production personnel,  
 GT – gas turbine,  
 GTPP – gas turbine power plant,  
 GTPP-CHP – gas turbine power plant combined heat and power,  
 GTU – gas turbine unit,  
 GVA – guide vane assembly,  
 GWHE – gas-water heat exchanger,  
 OPEX – operating expenditures,  
 TVA – turning vane assembly,  
 $C^{FC}$ , \$ – the value of fuel costs,  
 $C'_{GTU}$  – GTU efficiency parameter,

$CC_{GTU}$ , mln \$ – GTU cost of the selected interval capacity,  
 $CC'_{GTU}$  – capital costs parameter,  
 $G$ , kg/sec – gas turbine gas flow rate,  
 $G_{ic}$ , KW – installed generation capacity,  
 $G_{nom}$ , KW – required nominal generation capacity of the plant,  
 $H$ , kJ/kg – disposable heat drop in a gas turbine, and non-rated output modes,  
 $K_n$  – conversion factor of units of electrical energy (KWh) into units of heat of combustion (kJ),  
 $N_{rated}$ , KW – output power, respectively, in the rated output mode,  
 $N_T$ , hour – the number of working hours in a year,  
 $P^{FC}$ , \$ – the price per cubic meter of natural gas,  
 $Q^{FC}$ , kJ/m<sup>3</sup> – heat of combustion of natural gas,  
 $Q_{cs}$ , kJ/kg – the amount of heat transferred to a cold source,  
 $Q_{hs}$ , kJ/kg – the amount of heat transferred to the hot source,  
 $T_1, T_{10}$ , K – temperatures of working medium in the rated and  
 $\eta_{GTU}$ , % – gas turbine efficiency,  
 $\eta_{rated}$ , % – output efficiency, respectively, in the rated output mode,  
 $\eta_t$ , % – thermal efficiency of the cycle,  
 $\lambda$  – hydraulic loss factor,

$\mu$  – the share of depreciation,  
 $\pi$  – compression ratio,  
 $\sigma$ , mln \$ – standard deviation,

## REFERENCES

- [1] Behrens, W., Hawranek, P. "Manual for the Preparation of Industrial Feasibility Studies". United Nations Industrial Development Organization, Vienna, 361 p., 1991
- [2] Sharpe, W., Gordon, A., Bailey, J. "Investments" (6th ed.). Prentice Hall, Inc., New Jersey, 962 p., 1999
- [3] Khatib, Hisham. Economic evaluation of projects in the electricity supply industry. No. 44. IET, 2003
- [4] Biezma, M. V., and J. R. San Cristobal. "Investment criteria for the selection of cogeneration plants—a state of the art review." Applied Thermal Engineering 26.5 (2006): 583-588
- [5] Kehlhofer, Rolf, et al. Combined-cycle gas & steam turbine power plants. Pennwell Books, 2009
- [6] Konova O., Komarov I., Lisin E. "The Relevance of Power Generating Capacities Based on the Combined Cycle Power Plants of High Power". Czech Journal of Social Sciences, Business and Economics. Vol. 1, Issue 1, pp. 101-110, 2012
- [7] Stoft, S. "Power System Economics: Designing Markets for Electricity". IEEE Press, Hoboken, New Jersey, 460 p., 2002
- [8] Labor Standards in the Power Engineering Projects (Gas-turbine Power Plant with 12-150 MW). Approved by RAO "UES of Russia" 03.12.2004
- [9] Colpier, U., Comland, D. "The Economics of the Combined Cycle Gas Turbine - an Experience Curve Analysis". Energy Policy, Vol. 30, No. 4, pp. 309-316, 2002
- [10] Huck, S. "Reading Statistics and Research" (6th ed.). Pearson Education, Inc., Boston, 593 p., 2012
- [11] Boyce, M. "Gas Turbine Engineering Handbook". Elsevier, Inc., Oxford, 950 p., 2011
- [12] Tsoutsanis, E., Li, Y., Pilidis, P., Newby, M. "Part-load Performance of Gas Turbines-Part II: Multi-point Adaptation with Compressor Map Generation And GA Optimization". Proceedings of the ASME 2012 Gas Turbine India Conference GTINDIA2012, 2012
- [13] Kim, J. H., Song, T. W., Kim, T. S. "Dynamic Simulation of Full Start-up Procedure of Heavy Duty Gas Turbines". Proceedings of ASME Turbo Expo 2001, 2001

# Application and Control Method of Electromagnetic Synchronizer for Double Rotor Motor Power Coupling System

Jiang Kejun, He Ren, and Zhang Lanchun

**Abstract**—On the double rotor motor power coupling system existing now, electromagnetic coupling of the inner motor is the only way to transmit engine power to drive axle. And this leads to the low transmission efficiency when the vehicle is driven by the engine. Aiming at this issue, this paper proposes the improvement measure, which is to add the electromagnetic synchronizer between the input shaft and the output shaft. According to the thinking of this measure, the paper analyzes the operating process of the electromagnetic synchronizer. Then using quadratic optimal control theory, the optimal PID control method is designed to control the duty ratio of the electromagnetic synchronizer driving voltage. In order to test the validity of the method, the paper builds the simulation model in Matlab/Simulink software. The simulation results indicate that the optimal PID control method can effectively control the work process of electromagnetic synchronizer. It can achieve the balance between frictional work and longitudinal jerk, and decrease the impact reasonably when the electromagnetic synchronizer switching its state.

**Index Terms**—Double rotor motor power coupling system, Electromagnetic synchronizer, Optimal control, Simulation and analysis

*Original Research Paper*  
DOI: 10.7251/ELS1519088K

## I. INTRODUCTION

DOUBLE rotor motor power coupling system was invited first by Martin Hoeijmaker in 2002[1], who was a professor at the Delft University of Technology. As a new-type power coupling system, it attracts more and more people's attentions now, and it has been considered as another new

Manuscript received 15 Jan 2015. Received in revised form 20 July 2015.

This research was supported by the Jiangsu Province Key Laboratory of Automotive Engineering (QC201301), the Natural Science Foundation of the Jiangsu Higher Education Institutions of China (13KJB580004), the National Science Foundation for Key Project of the Jiangsu Higher Education Institutions of China (13KJA580001), the National Natural Science Foundation of China (51305175), the Post-graduate Innovative Fund Project of Jiangsu Province (CXZZ13\_0661) and University research fund of Jiangsu University of Technology (KYY14008).

Jiang Kejun is with the School of Automobile and Traffic Engineering, Jiangsu University, Zhenjiang, China. (e-mail: applekj@163.com). He is also with Jiangsu University of Technology, Changzhou, China.

He Ren is with Jiangsu University, Zhenjiang, China. (e-mail: Heren@ujs.edu.cn).

Zhang Lanchun is with Jiangsu University of Technology, Changzhou, China. (e-mail: zlc@jstu.edu.cn).

effective solutions for the hybrid electric vehicle[2-4]. Double rotor motor power coupling system is a non contact dynamic coupling system, and its structure and principle are shown in Fig.1[5-6]. This system mainly consists of the double rotor motor, the inverter/rectifier, the internal- combustion engine, the battery and the control unit. The double rotor motor can be divided again into the inner motor and the outer motor. The outer motor can drive the vehicle directly, and can change into a generator to convert the kinetic energy into electrical energy. Of course, the generator can provide the resisting moment to brake the vehicle. The inner motor can transmit engine power to drive axle by using the electromagnetic coupling effect. If necessary, it can change into the generator, and turn engine power into electricity.

According to the recent studies, this system has the advantages of simple structure, easy maintenance, no wear, and multiple operating modes[7-8].

According to the technical proposal of Professor Martin Hoeijmaker, the input shaft of the double rotor motor connects with the output shaft of the engine, and the output shaft connects with the drive axle. Electromagnetic coupling effect of the inner motor is the only way to transmit engine power to drive axle, and the electromagnetic torque of inner motor is the only load on the engine. This arrangement makes the engine working more freely, and can achieve the optimal control more easily.

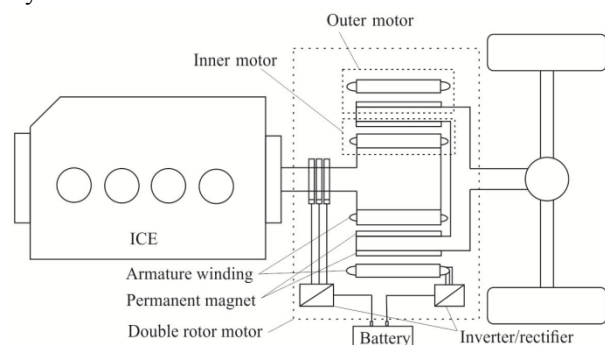
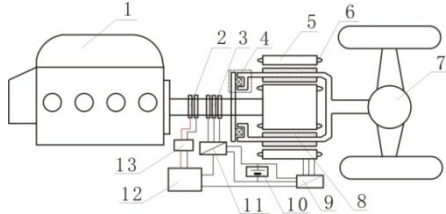


Fig.1 Schematic of double rotor motor power coupling system

Objectively speaking, the transmission efficiency of electromagnetic coupling is lower than mechanical transmission. This influences the comprehensive efficiency of the whole system. But if we use the electromagnetic synchronizer to connect the input shaft and the output shaft directly, as showed in Fig.2, we can overcome the shortcoming,

and realize the no-power-loss transmission. The result is improving the comprehensive fuel economy of the vehicle. On the same time, the mechanical joining can reduce the working temperature of the double rotor motor.

This article starts from the structure and principle of the electromagnetic synchronizer. Using the optimal control method to control the duty ratio of the electromagnetic synchronizer's driving voltage accurately. This paper will achieve good switch from electromagnetic drive to mechanical and direct transmission.



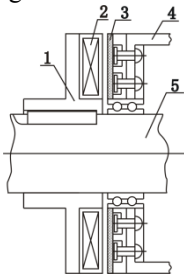
1-engine 2-power slip ring of electromagnetic synchronizer 3-power slip ring of inner rotor 4-electromagnetic synchronizer 5-stator coil 6-outer permanent magnet of outer rotor 7-drive axle 8- inner permanent magnet of outer rotor 9- inverter/ rectifier of outer motor 10-battery 11-inverter/ rectifier of inner motor 12-control unit 13-driving amplifier

Fig.2 Installation diagram of electromagnetic synchronizer

## II. PRINCIPLE AND OPERATION PROCESS OF THE ELECTROMAGNETIC SYNCHRONIZER

### A. Structure and Principle

The electromagnetic synchronizer makes the power transmission skip the double rotor motor, and it can transfer engine torque to the drive axle directly with the static friction effect. Similar to electromagnetic clutch[9], the electromagnetic synchronizer is consist of electromagnetic coil, active part, driven part, and armature iron, etc. The whole structure is shown in Fig.3.



1-active part 2-electromagnetic coil 3-armature iron 4-driven part (to the drive axle) 5-output shaft of engine

Fig.3 Structure diagram of electromagnetic synchronizer

According to the structure of the electromagnetic synchronizer, we can see the operation principle is as followed.

The electromagnetic coil produces the attractive force when energized, then the attractive force makes the armature iron move to the active part. The armature iron connects to the driven part by rivets, and the armature iron has a friction layer, which can rub on the active part when the armature iron touches the active part. The active part links to the output shaft of the engine by key joint. If the dynamic friction appears, the dynamic frictional force will be generated. And from this time, the active part turns the driven part by the dynamic frictional force. When the driven part turns as fast as the active part, the

synchronizing process is achieved. Now the dynamic friction changes into static friction which becomes the main factor in transmission, and the power of the engine can be transferred to the drive axle by the static friction force.

### B. Operation Process

According to the principle of electromagnetic synchronizer, the operation process of the electromagnetic synchronizer can be divided into four phases (as shown in Fig. 4). The first is gap-elimination phase (T1), in which the duty is to eliminate the gap between the electromagnetic coil and the armature iron, so general requirements of this phase are action rapidly and shortening time. The second phase is sliding and friction stage (T2), in which the driven part has touched the active part, the dynamic friction begins to produce effects, and power driven part turning faster. When the driven part synchronizes with the active part, the second phase ends. This phase asks for shorter action time, smaller impact and less friction work. The third phase is static friction stage (T3). In this phase, friction changes into static from dynamic, the driven part and the active part begin to turn together at the same speed. The third phase asks for no skid and complete synchronization. The last phase is synchronization end stage (T4). This phase needs the rapid separation of the driven part and the active part.

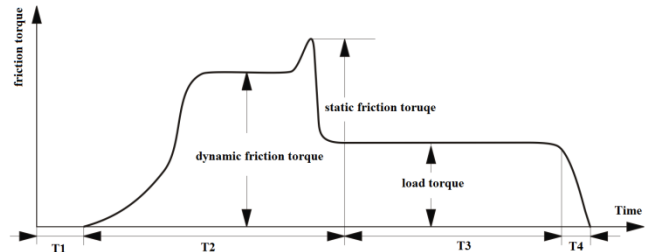


Fig.4 Characteristic curve in working process of electromagnetic synchronizer

## III. CONTROL STRATEGY OF SYNCHRONIZATION PROCESS

### A. Performance Indicators of Synchronization Process

The aim of this paper is to reduce the vibration and impact when the electromagnetic synchronizer switches its state. According to the performance evaluation method of the electromagnetic synchronizer [10], this paper lists synchronization time, friction work and longitudinal jerk as performance indicators.

(1) Synchronization time. Synchronization time is the time from acceptance of synchronization command to the achievement of synchronization. From the Fig.4, we can see the synchronization time is the time of T1 and T2. From Fig.3, we can see the gap between the electromagnetic coil and armature iron is very small. So we can ignore the T1 phase, and let synchronization time equal to the time of T2.

(2) Friction work. Friction work refers to the work produced by the slid and friction between the active part and the driven part. Friction work mainly occurs in phase T2, and it can directly affect the service life of the electromagnetic synchronizer, and it is the main reason for the temperature rise. Friction work can be calculated by the formula (1).

$$W = \int T(t) |\omega_c(t) - \omega_d(t)| dt \quad (1)$$

Where  $\omega_e(t)$  is the speed of the active part,  $\omega_c(t)$  is the speed of the driven part,  $T(t)$  is the working torque of the electromagnetic synchronizer.

According to the dynamic mechanical analysis of the electromagnetic synchronizer, the dynamic movement of the active part can be expressed as the formula (2).

$$\omega_e(t) I_e = T_e - T(t) \quad (2)$$

Where  $T_e$  is the output torque of the engine,  $I_e$  is the rotational inertia of the active part.

For the driven part, the movement can be described as follows:

$$\omega_c(t) I_c = T(t) \quad (3)$$

Where  $I_c$  is the rotational inertia of the driven part.

(3) Longitudinal jerk. Longitudinal jerk is the evaluation indicator of the electromagnetic synchronizer when state switching, its expression is as follow:

$$J = \frac{dV^2}{dt^2} = \frac{r}{i} \omega_c(t) = \frac{r}{i I_c} \frac{d(T(t))}{dt} \quad (4)$$

Where,  $r$  is the effective radius of the wheel, and  $i$  is final gear ratio of drive axle,  $V$  is the speed of the vehicle.

Longitudinal jerk directly affects ride comfort of the vehicle and service life of the power transmission system. According to the relevant laws, the value of truck's longitudinal jerk should be less than  $10\text{m/s}^2$ , and the longitudinal jerk of passenger car should be less than  $5\text{m/s}^2$ . So in order to control the value of the longitudinal jerk, the key is to control the change of electromagnetic torque. That means the electromagnetic torque should change smoothly in the friction stage.

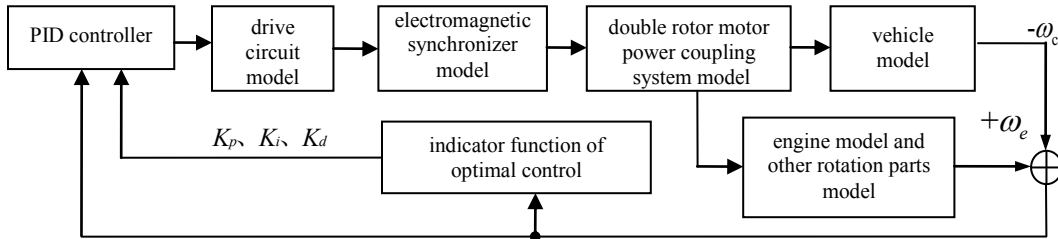


Fig.5 Control model of the optimal PID

### C. Design of the Optimal Control

In the Synchronization, the frictional work and the longitudinal jerk are opposing. If the frictional work reduces, the time of state switching will shorten inevitably, the result is the longitudinal jerk increases, and the converse is also true. So in the design of the optimal control, we need to balance the two performance indicators.

Choose  $x_1 = \omega_{ec}(t)$ ,  $x_2 = T(t)$  as the state variables, choose  $u = \frac{d(T(t))}{dt}$  as the controlled variable, based on the quadratic optimal control theory, the formula (1)-(4) can be changed in state space equation as follow.

### B. Control Strategy of Electromagnetic Synchronizer

When design control strategy of electromagnetic synchronizer, we need to consider the working process and the performance characteristic of the electromagnetic synchronizer. This paper adopts the sectional control method as follows[11].

(1) In the T1 phase, the working torque is zero, so the drive current of the electromagnetic synchronizer should be as big as possible to shorten the time of gap elimination.

(2) In the T2 phase, the main objective is to reduce the friction work, so we choose the optimal PID control method. This method has parameter self-tuning function, and has the advantages of high reliability and robustness. Select speed difference  $\omega_{ec}(t) (\omega_{ec}(t) = \omega_e(t) - \omega_c(t))$  as detection object, select angular acceleration change rate function of the driven part as restricted object, and select the friction work and longitudinal jerk as optimization object, we design the feedback control method as shown in Fig.5.

(3) In the T3 phase, the control target is static friction torque. The maximum value of static friction torque must be bigger than working torque to make sure there is no slipping between the driven part and the active part. To reduce the electrical energy consumption, and maintain static friction state, the target value of the static friction force can be determined by the product of transfer torque and its fluctuation coefficient.

(4) In the T4 phase, the aim is the driven part separates rapidly from the active part. In this phase, we can use the switch control.

According to the thinking of sectional control method, we think the controls of the T1, T3 and T4 phase are relatively simple. While the control of the T2 phase is complicated. So we choose the control of the T2 phase as the main study object, and design an optimal PID control method[12]. The flowchart of this method is shown in Fig.5.

$$\dot{x} = AX + BU + C \quad (5)$$

Here,  $X = \begin{bmatrix} x_1 \\ x_2 \end{bmatrix}$ , the state matrix  $A = \begin{bmatrix} 0 & \frac{I_c + I_e}{I_e I_c} \\ 0 & 0 \end{bmatrix}$ , the

state matrix  $B = \begin{bmatrix} 0 \\ 1 \end{bmatrix}$ , the disturbance matrix  $C = \begin{bmatrix} \frac{T_e}{I_e} \\ 0 \end{bmatrix}$ , the

control matrix  $U = [u]$ .

From these, the frictional work can be expressed as follow:

$$W = \int x_1 x_2 dt \quad (6)$$

And the longitudinal jerk can be expressed as follow:

$$J = \frac{r}{iI_c} u \quad (7)$$

Consider the balance of the frictional work and the longitudinal jerk, we choose the quadratic performance functional of the optimal control system as follow:

$$\begin{aligned} L &= \frac{1}{2} \int (x^T Q x + \eta u^2) \frac{d^2 \omega}{dt^2} \\ &= \frac{1}{2} \int (x_1 x_2 + \eta u^2) dt \end{aligned} \quad (8)$$

Where, the state weight matrix  $Q = \begin{bmatrix} 0 & 0.5 \\ 0.5 & 0 \end{bmatrix}$ ,  $\eta$  is the

weight proportion of the longitudinal jerk, its value range is between 0 and 1 in theory.

Refer to the formula (6)-(8), and use the solution of the Riccati matrix differential equation[13], we can get the optimal control locus of  $u$ . Then build the dynamics models of electromagnetic synchronizer and its drive circuit, we can calculate the value of the control electrical signal.

#### IV. BUILDING MODEL

##### A. Kinetic Model of the Electromagnetic Synchronizer

The main performance parameter of the electromagnetic synchronizer is the maximum transmission torque. According to the operation principle of the electromagnetic synchronizer which belongs to frictional synchronizer, we can know that the maximum transmission torque can be expressed as follow[14]:

$$T = \frac{1}{2} \mu R F m \quad (9)$$

Where,  $T$  is the maximum transmission torque,  $\mu$  is the friction coefficient. In static friction process,  $\mu$  is static friction coefficient. And when in dynamic friction,  $\mu$  is dynamic friction coefficient. Besides,  $R$  is the effective radius of the annular friction surface,  $F$  is the pressing force, it is equal to the electromagnetic force of electromagnetic coil. And  $m$  is the number of annular friction surface.

In the static friction and dynamic friction stage, the calculation methods of  $R$  are different. When in the static friction,  $R$  can be calculated by formula (10), and when in the dynamic friction,  $R$  can be calculated by formula (11).

$$R = \frac{2(R_o^3 - R_i^3)}{3(R_o^2 - R_i^2)} \quad (10)$$

$$R = \frac{1}{2}(R_o - R_i) \quad (11)$$

Here,  $R_o$  is the excircle radius of friction torus, and  $R_i$  is the inner circle radius of friction torus.

According to the Maxwell equations, the electromagnetic force can be expressed as the formula (12) [15-16].

$$F = \frac{\phi^2}{2\mu_0 S} = \frac{B^2 S}{8\pi} \times 10^7 \quad (12)$$

Here,  $\phi$  is the magnetic flux,  $S$  is the effective area of the armature iron,  $\mu_0$  is vacuum magnetic permeability, its value is  $4\pi \times 10^{-7}$  Wb/(Am), and  $B$  is magnetic induction intensity of electromagnetic coil, which can be calculated by the formula (13)[16].

$$B = \frac{NI}{K\delta} \times \mu_0 \quad (13)$$

Here,  $N$  is the turns number of the electromagnetic coil,  $I$  is the current of the electromagnetic coil,  $\delta$  is the air gap between the electromagnetic coil and armature iron, and  $K$  is magnetic flux leakage factors.

##### B. Drive Circuit Model

According to the formula (9) - (13), we can know the main control parameter of the electromagnetic synchronizer is the driving current. This paper adopts the PWM method to adjust the effective driving voltage of the electromagnetic synchronizer[17], and then to control the driving current. The structure of the circuit is shown in Fig. 6.

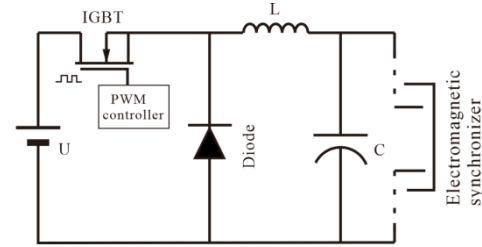


Fig.6 Drive circuit structure of electromagnetic synchronizer

Hypotheses:

- (1) IGBT is the ideal element. It has the ideal performance characteristics. So its switch lag time, inductive reactance, capacitive reactance, and voltage drop will be ignored.
- (2) Voltage source is ideal, and its internal resistance is zero.
- (3) Electromagnetic synchronizer can be equivalent to a resistance load. Its inductance characteristic can be ignored.

According to Kirchoff's laws, the circuit in Fig.6 can be described as follows:

$$\square x_i = \begin{bmatrix} 0 & -\frac{1}{L} \\ \frac{1}{C} & -\frac{1}{R_s C} \end{bmatrix} \begin{bmatrix} x_i \\ x_u \end{bmatrix} + \begin{bmatrix} \frac{1}{L} \\ 0 \end{bmatrix} PU \quad (14)$$

$$\square x_u = \begin{bmatrix} -\frac{1}{L} & 0 \\ \frac{1}{C} & -\frac{1}{R_s C} \end{bmatrix} \begin{bmatrix} x_i \\ x_u \end{bmatrix} \quad (15)$$

Where,  $U$  is the supply voltage,  $x_i$  is the current of the electromagnetic synchronizer,  $R_s$  is the equivalent resistance of electromagnetic synchronizer, and  $x_u$  is the voltage of the

electromagnetic synchronizer. Besides, C, L, P are the capacitor, the inductor and the duty cycle respectively.

## V. TEST RESULT AND ANALYSIS

When we use quadratic optimal control theory to evaluate the duty ratio of the driving voltage, the value of  $\eta$  is the critical factor. In this paper,  $\eta$  is set to 0.5. This means the friction work and the longitudinal jerk have the same weight in the optimal control.

Referring to the formula above, we set up the simulation model all in Matlab/Simulink software[18]. Then execute the simulation, we can get the duty cycle's curve of the driving voltage in the whole working cycle, which is shown as Fig.7. Here, the time of T3 phase is set to 0.8s.

From the Fig.7, we can see the optimal PID control method demonstrates the four working process of the electromagnetic synchronizer wholly. In the whole working cycle, the gap eliminating time (T1) is 0.17s, the sliding time (T2) is 0.81s, and the time of ending synchronization (T4) is 0.09s.

From the Fig.7, we also can see the gap eliminating time and the ending synchronization time are both very short, and the ultimate control parameter (P) can effectively track the target value with the control of the optimal control method. On the same time the state switching process is relatively stable, the overshoot, the attenuation ratio and the recovery time are all in a good state.

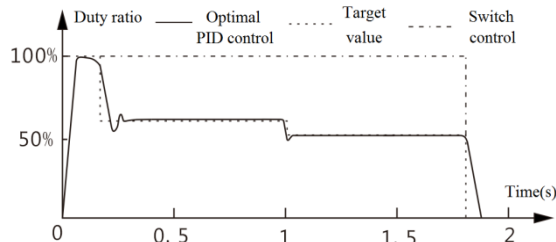


Fig.7 Control voltage duty ratio curve of electromagnetic synchronizer

From these results above, we can think the control method designed in this paper has realized the anticipated effect entirely.

Fig.8 is the speed curve of the active part (inner-rotor) and the driven part (outer-rotor). From this curve, we can see the rotating speed fluctuations of the active part and the driven part is mainly in the T2 stage. Compared with the switch control method (referring to the switch control curve in the Fig.7), the friction time of the optimal PID control method is about 0.16s longer. But rotating speed of the active part and the driven part under the control of the optimal PID is more stable, and its fluctuations is smaller.

Fig.9 is the curve of the longitudinal jerk. From this curve, we can see the maximum value of the longitudinal jerk under switch control is  $6.8\text{m/s}^2$ , and the fluctuation amplitude is larger. But under the optimal PID control, the maximum value is  $4.3\text{m/s}^2$ , a big drop of 37%. Furthermore, under the optimal PID control, the maximum value of the longitudinal jerk appears at the primary stage of the sliding and friction stage, and afterward, the longitudinal jerk is small.

Conversely, under the switch control, the longitudinal jerk has no obvious decrease in the first half time, only in the end of the sliding and friction stage, the longitudinal jerk begins to converge.

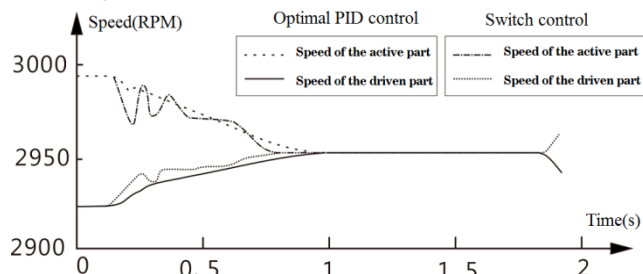


Fig.8 Speed curve of the driven part and the active part

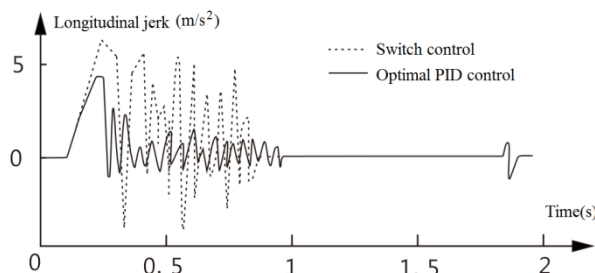


Fig.9 Curve of longitudinal jerk

Fig.10 is the friction work curve of the whole work cycle. From the figure, we can see the friction work under the optimal PID control increases by about 0.2KJ compared with the switch control method. This means the optimal PID control method can effectively balance two warring performance indicators: the frictional work and the longitudinal jerk.

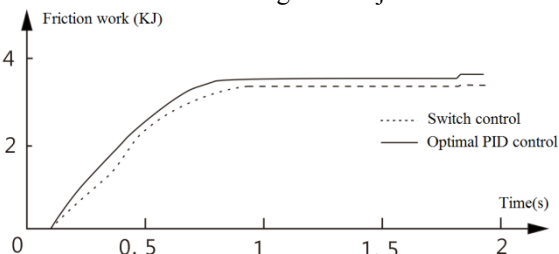


Fig.10 Curve of friction work

As was mentioned above, we can think the optimal PID control method designed in this paper is successful. And by this method, the electromagnetic synchronizer can do its job well in the double rotor motor power coupling system. It can improve the ride comfort and transmission efficiency of the hybrid electric vehicle.

## VI. CONCLUSION

(1) This paper bases on the structure and principle of the double rotor motor power coupling system, proposes the improvement measure: add electromagnetic synchronizer between the input shaft and the output shaft. With the help of the electromagnetic synchronizer, the inner rotor and the outer rotor are connected rigidly, and the double rotor motor power coupling system can realize mechanical direct transmission. At this time, engine power can be transmitted

to the drive axle with direct mechanical joining, jumping over the electromagnetic coupling transmission of the double rotor motor power coupling system. This can improve transmission efficiency obviously.

(2) Considering the structure features and the working process of the electromagnetic synchronizer, this paper proposes the think and strategy of the sectional control method for electromagnetic synchronizer. After analysis of each stage working characteristics to the electromagnetic synchronizer, the sliding and friction phase is chosen as the main study object. Then using the two quadratic optimal control theory, we select friction work and the longitudinal jerk as the performance indicator, and set up the quadratic performance functional. From these, the optimal PID control method is designed.

(3) This paper builds the mathematical models of the electromagnetic synchronous and its control circuit. Using the models and the optimal PID control method, we simulate the working process of the electromagnetic synchronous. The simulation results show the optimal PID control method can effectively control the working process of electromagnetic synchronizer. It can balance the friction work and the longitudinal jerk, and reduce the impact when the electromagnetic synchronizer switches its state. In conclusion, to the double rotor motor power coupling system, electromagnetic synchronizer can play a significant role in efficiency improvement and the ride comfort when the vehicle is at economical speed.

#### REFERENCES

- [1] M. J. Hoeijmakers, "Electromechanical Converter (Patent type)," WO Patent 03 075437 A1, December 9, 2003.
- [2] Shi Guangkui, Zhao Hang, and Feng Qi, "A Study on Hybrid PowerSystem with Double RotorMotor," *Automotive Engineering*, vol. 29, no. 2, pp. 97-100, Feb.2007.
- [3] Mo Lihong, Quan Li, Zhu Xiaoyong, and et al, "An overview of dual-rotor motor and its application to hybrid electric vehicle," *Engineering Journal of Wuhan University*, vol. 45, no. 5, pp. 510-515, May. 2012.
- [4] E. Vinot, R. Trigui, and et al, "Improvement of an EVT-Based HEV Using Dynamic Programming," *IEEE Transactions on Vehicular Technology*, vol. 63, no.1, pp.40-50.
- [5] M. J. Hoeijmakers, M. Rondel, "The Electrical Variable Transmission in a City Bus (Published Conference Proceedings style)," in *35th IEEE Power Electronics Specialist Conference*, Aachen, Germany, 2004, pp.2273-2278.
- [6] M. J. Hoeijmakers, J. A. Ferreira, "The Electrical Variable Transmission," in *Proc. 39th Annual Meeting. IEEE Industry Applications Conference*, Seattle, Washington US, 2004, pp.2770-2777.
- [7] M. Wilke, R. Goraj, and et al, "Numerical Calculations of a Hybrid Power Train for Motor Vehicles," in *the 18th International Conference on Electrical Machines*, Vilamoura, Algarve, Portugal, 2008, pp.1-4.
- [8] Backx P. W, "Prototype Testing of the Electric Variable Transmission," Eindhoven, 2008. [Online]. Available: <http://www.mate.tue.nl/mate/pdfs/9093.pdf>.
- [9] Gu Qingchang, "The Magnetic Field Analysis and The Characteristics Research of Magnetic-Electromagnetic Clutch (dissertation style)," Hefei University of Technology, 2008.
- [10] Li Yong, Yu Jiang, Cui You, and et al, "Principle and Dynamic characteristics control of a two steady state electromagnetic clutch," *Journal of Harbin Institute of Technology*, vol. 39, no. 9, pp.1407-1410, Sep.2007.
- [11] Yan Yiquan, Song Jian, and Li Liang, "Multi-section Optimization Shift Control Method of Dry Dual Clutch Transmission," *Transactions of the Chinese Society for Agricultural Machinery*, vol. 45, no.5, pp.30-36, May.2014.
- [12] Liu Jinkun, *MATLAB simulation of advanced PID control (Third Edition)* (Book style). Beijing, CA: Publishing House of Electronics Industry,2011, pp.240-265.
- [13] Xue Dingyu, *The control system simulation and computer aided design* (Book style). Beijing, CA: Machinery Industry Press, 2011, pp.218-221.
- [14] Zhou Wu, "Comprehensive Calculating Method of Friction Moment for Circle Disc Frictional Cultch," *Journal of Shaanxi Institute of Technology*, vol. 20, no. 4, pp.4-11, Apr.2004.
- [15] Mei Liang, Liu Jinglin, and Fu Zhaoyang, "Calculation of Electromagnet Attractive Force and Simulation Analysis," *Micromotors*, vol. 45, no. 6, pp.6-9, Jun. 2012.
- [16] Lou Luliang, Wang Haizhou, "Methods of Electromagnetic Force calculation for Engineering Application," *Missile And Space Vehilce*, pp.40-45, Jan. 2007.
- [17] Li Shuiliang, Du Yinghui, and Yan Shoucheng, "Bonding Strength Controlling system of Electromagnetic Clutch Based on HCS Single-chip PWM," *Journal of Chongqin Institute of Technology (Natural Science)*, vol. 23, no. 11, pp.11-12, Nov. 2009.
- [18] Yu Qun, Cao Na, *MATLAB/Simulink Modeling and Simulation of power system*[Book style]. Beijing, CA: China Machine Press, 2011.

# Single DD-DXCCII based quadrature oscillator with simultaneous current and voltage outputs

B. Chaturvedi and J. Mohan

**Abstract**—In this paper, a versatile quadrature oscillator using single Differential Difference Second Generation Dual-X Current Conveyor (DD-DXCCII) as an active element, two grounded capacitors and three grounded resistors is presented. The proposed oscillator provides two current outputs and three voltage outputs in quadrature relationship simultaneously so named as versatile quadrature oscillator. The proposed versatile quadrature oscillator exhibits the feature of orthogonal control over the frequency of oscillation and condition of oscillation. Effects of non-idealities along with sensitivity analysis are also analyzed. The proposed circuit has low active and passive sensitivities. Parasitic study is further explored. The simulation results with 0.18 $\mu$ m CMOS process parameters using PSPICE are also given. Possible realization of proposed oscillator using AD-844 and LM13600 along with some simulation results are also given for completeness sake.

**Index Terms**—Current Conveyors, Quadrature Oscillators, AD-844.

Original Research Paper  
DOI: 10.7251/ELS1519094C

## I. INTRODUCTION

ONE of the noteworthy things about quadrature oscillators, as in various communication applications, is a requirement of sinusoid signals that are 90° phase in difference [1]. In the literature a number of quadrature oscillators based on different active elements are reported [3-25] and the references cited therein. The quadrature oscillators in [3-5, 7-8, 24-25] produced voltage-mode signals and the ones in [9-17, 23] produced current-mode signals. Although some of the quadrature oscillators in [6, 18-22] generated both voltage-mode as well as current-mode signals. Moreover, few of them are based on single active element [9, 10, 12, 13, 16, 19, 23]. A comparison study with existing oscillators has been given in Table 1.

Manuscript received 15 March 2015. Received in revised form 23 July 2015.

B. Chaturvedi is with the Department of Electronics and Communication Engineering, Jaypee Institute of Information Technology, Noida-201304 (India)

J. Mohan is with the department of electronics and communication engineering, jaypee institute of information technology, Noida-201304, (India); phone: +91-120-24195865; e-mail: jitendramv2000@rediffmail.com.

This paper presents a novel circuit of versatile quadrature oscillator using a single DD-DXCCII along with two grounded capacitors and three grounded resistor. The proposed circuit enjoys the use of single active element and use of grounded components. The proposed circuit of versatile quadrature oscillator contains orthogonal control of frequency of oscillation and condition of oscillation. The proposed versatile quadrature oscillator provides quadrature current-mode outputs and voltage-mode outputs simultaneously.

## II. CIRCUIT DESCRIPTION

### A. DD-DXCCII

The advantages of the Differential Difference Current Conveyor (DDCC) [2] and the Dual-X Second Generation Current Conveyor DXCCII [14] are combined and hence re-named as DD-DXCCII [26, 27]. Keeping this in consideration, the port relationships of DD-DXCCII are now characterized as:

$$\begin{bmatrix} I_{Y1} \\ I_{Y2} \\ I_{Y3} \\ V_{X+} \\ V_{X-} \\ I_{Z+} \\ I_{Z-} \end{bmatrix} = \begin{bmatrix} 0 & 0 & 0 & 0 & 0 & 0 & 0 \\ 0 & 0 & 0 & 0 & 0 & 0 & 0 \\ 0 & 0 & 0 & 0 & 0 & 0 & 0 \\ 1 & -1 & 1 & 0 & 0 & 0 & 0 \\ -1 & 1 & -1 & 0 & 0 & 0 & 0 \\ 0 & 0 & 0 & 1 & 0 & 0 & 0 \\ 0 & 0 & 0 & 0 & 1 & 0 & 0 \end{bmatrix} \begin{bmatrix} V_{Y1} \\ V_{Y2} \\ V_{Y3} \\ I_{X+} \\ I_{X-} \\ V_{Z+} \\ V_{Z-} \end{bmatrix} \quad (1)$$

The symbol and CMOS implementation of DD-DXCCII is shown in Fig. 1. The CMOS implementation of DD-DXCCII is a combination of DDCC ( $M_{25} - M_{34}$ ) with unemployed Z-stages and DXCCII ( $M_1 - M_{24}$ ). In the CMOS implementation of DD-DXCCII, the X-terminal (gate of  $M_{30}$ ) of DDCC drives the Y-terminal (gate of  $M_2$ ) of the DXCCII. The Z+ and Z-stages are realized from the drain of  $M_{11}$  and  $M_{16}$  transistors. The difference of the  $Y_1$  and  $Y_2$  terminal voltages in addition with the voltage at  $Y_3$  terminal is conveyed to the X+ terminal; the current at the X+ terminal is conveyed to the Z+ terminal and The difference of the  $Y_2$  and  $Y_1$  terminal voltages in subtraction with the voltage at  $Y_3$  terminal is conveyed to the X-terminal; the current at the X- terminal is conveyed to the Z- terminal. In a DD-DXCCII, terminals  $Y_1$ ,  $Y_2$  and  $Y_3$  exhibit high input impedance. Thus, no current flows in terminals  $Y_1$ ,  $Y_2$  and  $Y_3$ . The terminal X+ and X- exhibit low input impedance and the terminals Z+ and Z- have high output impedance.

TABLE I  
COMPARISON WITH OTHER PREVIOUSLY KNOWN OSCILLATOR

Refs.	Single Active Element	Type of Active Element	No. of Resistors	No. of Capacitors	All Grounded Passive Components	No. of Current Outputs	No. of Voltage Outputs	Orthogonal/ Independent controlling	Designed Frequency of Oscillation
3	No	CC	2G	2G	Yes	-	2	NA	-
4	No	OTA	-	2F, 1G	No	-	2	No	300KHz
5	No	OTA	-	2G	Yes	-	4	Yes	10KHz
6	No	CCII	3G	2G	Yes	1	2	Yes	159KHz
7	No	OTA	-	3G	Yes	-	1	Yes	2MHz
8	No	DDCC	3G	2G	Yes	-	2	No	10.61MHz
9	Yes	FTFN	3F, 2G	3G	No	1	-	Yes	NA
10	Yes	CF+	3F	3G	No	2	-	No	NA
11	No	OA & OTA	-	-	-	2	-	No	1MHz
12	Yes	FTFN	2F, 1G	2F, 1G	NO	2	-	Yes	NA
13	Yes	FTFN	2	5	No	1	-	Yes	28KHz
15	No	MOCCH	2G	2G	Yes	8	-	No	358KHz
16	Yes	ZC-CDTA	2F	2G	No	1	-	Yes	59.77KHz
17	No	DVCC	3G	2G	Yes	4	-	Yes	1MHz
18	No	CCCII	-	2G	Yes	4	2	Yes	140KHz
19	Yes	FDCCII	3G	2G	Yes	2	2	No	7.9KHz
20	No	DXCCII	2G	3G	Yes	3	3	Yes	1.7MHz
21	No	ZC-CG-CDBA	3F	2G	No	2	2	Yes	2.75MHz
22	No	DVCC	2G	2G	Yes	3	2	No	4.15MHz
23	Yes	FTFN	3F, 2G	2G	No	2	-	Yes	6.9KHz
24	No	DXCCII	1F, 1G	1F, 1G	No	-	2	No	24.93MHz
25	No	DVCC	3F	3G	NO	-	4	Yes	2.5MHz
Proposed	Yes	DD-DXCCII	3G	2G	Yes	2	2	Yes	26.54MHz

**Abbreviations:** CC: Current Conveyor, OTA: Operational Transconductance Amplifier, CCII: Second Generation Current Conveyor, DDCC: Differential Difference Current Conveyor, FTFN: Four-Terminal Floating Nullor, CF+: Positive Current Follower, OA: Operational Amplifier, MO-CCII: Multi-Output Second Generation Current Conveyor, ZC-CDTA: Z-Copy Current Differencing Transconductance Amplifier, DVCC: Differential Voltage Current Conveyor, CCCII: Current Controlled Second Generation Current Conveyor, FDCCII: Fully Differential Second Generation Current Conveyor, DXCCII: Dual-X Second Generation Current Conveyor, ZC-CG-CDBA: Z-Copy Controlled Gain Current Differencing Buffered Amplifier, DD-DXCCII: Differential Difference Second Generation Dual-X Current Conveyor, NA: Not Available, F: Floating, G: Grounded.

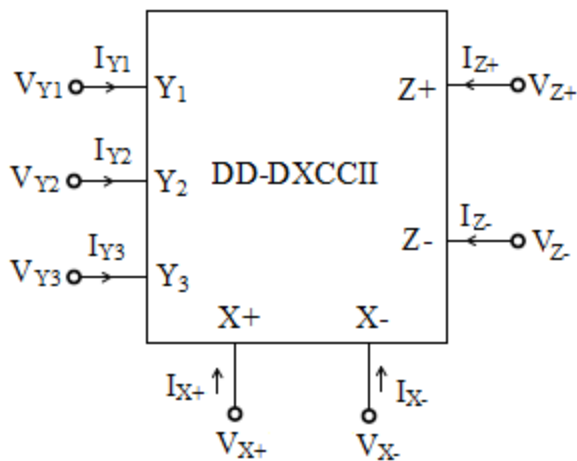


Fig. 1(a). Symbol of DD-DXCCII [26, 27]

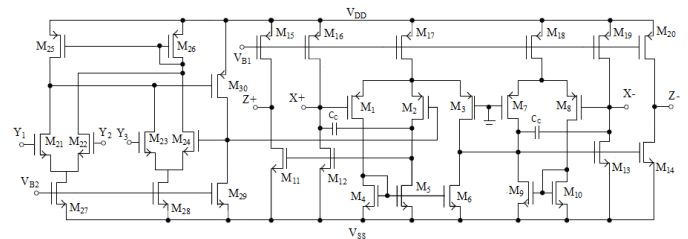


Fig. 1(b). CMOS implementation of DD-DXCCII [26, 27]

### B. The Proposed Versatile Quadrature Oscillator

The proposed versatile quadrature oscillator circuit is shown in Fig. 2. Routine analysis of the proposed oscillator using equation (1) yields the following characteristic equation

$$s^2 + s \left( \frac{1}{C_1 R_1} + \frac{1}{C_2 R_3} - \frac{1}{C_1 R_2} \right) + \frac{1}{C_1 C_2 R_1 R_3} = 0 \quad (2)$$

From equation (2), the frequency of oscillation (FO) and condition of oscillation (CO) are given as

$$\text{FO: } \omega_o = \sqrt{\frac{1}{C_1 C_2 R_1 R_3}} \quad (3)$$

$$\text{CO: } \frac{1}{C_1 R_1} + \frac{1}{C_2 R_3} \geq \frac{1}{C_1 R_2} \quad (4)$$

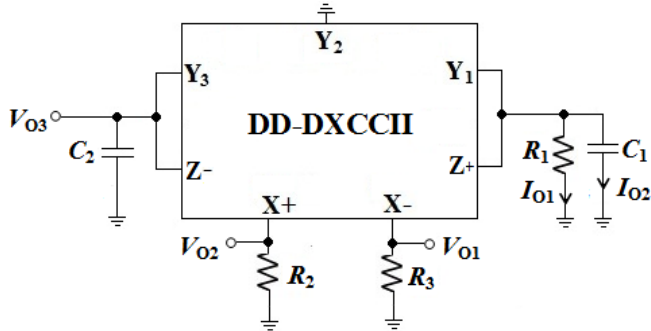


Fig. 2. Proposed versatile quadrature oscillator

It is to be noted from equation (3) and equation (4) that the FO and CO are orthogonally controlled.

The two currents outputs ( $I_{O1}$  and  $I_{O2}$ ) and three voltage outputs ( $V_{O1}$ ,  $V_{O2}$  and  $V_{O3}$ ) of the proposed versatile quadrature oscillator, shown in Fig. 3 are related as

$$I_{O2} = j\omega C_1 R_1 I_{O1} \quad (5)$$

$$V_{O1} = j\omega C_2 R_2 V_{O3} \quad (6)$$

$$V_{O1} = -V_{O2} \quad (7)$$

Thus, the proposed circuit provides two quadrature current outputs ( $I_{O1}$  and  $I_{O2}$ ) and three quadrature voltage outputs ( $V_{O1}$ ,  $V_{O2}$  and  $V_{O3}$ ) simultaneously.

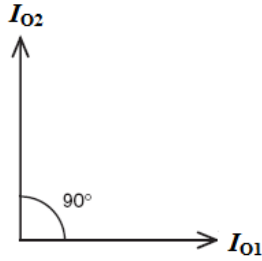


Fig. 3(a). Phasor diagram depicting quadrature current outputs

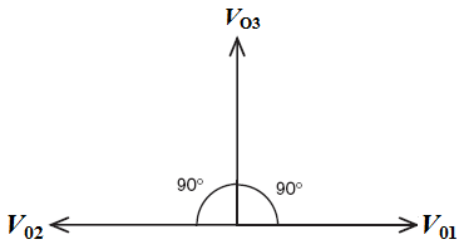


Fig. 3(b). Phasor diagram depicting quadrature voltage outputs

### C. Sensitivity Analysis

The detailed analysis of sensitivity shows a vital index of the performance of any active system. The proper definition of sensitivity is given as follows:

$$S_Y^X = \frac{Y}{X} \frac{\partial X}{\partial Y} \quad (8)$$

where, X represents the circuit performance parameters and Y represents the value of the passive elements. Using the above definition, the passive sensitivities with respect to one of the circuit performance parameters i.e. FO ( $\omega_o$ ) are given as below

$$S_{C_1}^{\omega_o} = S_{C_2}^{\omega_o} = S_{R_1}^{\omega_o} = S_{R_3}^{\omega_o} = -\frac{1}{2} \quad (9)$$

It is to be noted from equation (6) that all the passive sensitivities are less than unity in magnitude and hence the proposed circuit exhibits a good sensitivity performance.

## III. NON-IDEAL AND PARASITIC STUDY

### A. Non-ideal Study

The proposed circuit is reanalyzed for the DD-DXCCII non-idealities [27], namely voltage transfer gains ( $\beta_i$ , where  $i = 1, 2, 3, 4, 5, 6$ ) and current transfer gains ( $\alpha_j$ , where  $j = 1, 2$ ). The relationship of the terminal voltages and currents can be rewritten as:

$$\begin{bmatrix} I_{Y1} \\ I_{Y2} \\ I_{Y3} \\ V_{X+} \\ V_{X-} \\ I_{Z+} \\ I_{Z-} \end{bmatrix} = \begin{bmatrix} 0 & 0 & 0 & 0 & 0 & 0 & 0 \\ 0 & 0 & 0 & 0 & 0 & 0 & 0 \\ 0 & 0 & 0 & 0 & 0 & 0 & 0 \\ \beta_1 & -\beta_2 & \beta_3 & 0 & 0 & 0 & 0 \\ -\beta_4 & \beta_5 & -\beta_6 & 0 & 0 & 0 & 0 \\ 0 & 0 & 0 & \alpha_1 & 0 & 0 & 0 \\ 0 & 0 & 0 & 0 & \alpha_2 & 0 & 0 \end{bmatrix} \begin{bmatrix} V_{Y1} \\ V_{Y2} \\ V_{Y3} \\ I_{X+} \\ I_{X-} \\ V_{Z+} \\ V_{Z-} \end{bmatrix} \quad (10)$$

The proposed versatile quadrature oscillator circuit of Fig. 2 is reanalyzed using equation (10) and the non-ideal characteristic equation is found as

$$s^2 + s \left[ \frac{1}{C_1 R_1} + \frac{\alpha_2 \beta_6}{C_2 R_3} - \frac{\alpha_1 \beta_1}{C_1 R_2} \right] + \frac{\alpha_2 (\alpha_1 \beta_3 \beta_4 R_1 + \beta_6 R_2 - \alpha_1 \beta_1 \beta_6 R_1)}{C_1 C_2 R_1 R_2 R_3} = 0 \quad (11)$$

From equation (11), the non-ideal FO and CO become as follows

$$\text{FO: } \omega_o = \sqrt{\frac{\alpha_2 (\alpha_1 \beta_3 \beta_4 R_1 + \beta_6 R_2 - \alpha_1 \beta_1 \beta_6 R_1)}{C_1 C_2 R_1 R_2 R_3}} \quad (12)$$

$$\text{CO: } \frac{1}{C_1 R_1} + \frac{\alpha_2 \beta_6}{C_2 R_3} \geq \frac{\alpha_1 \beta_1}{C_1 R_2} \quad (13)$$

Furthermore, by using equation (8), the sensitivities of active ( $\beta_i$ , where  $i = 1, 2, 3, 4, 5, 6$  and  $\alpha_j$ , where  $j = 1, 2$ ) and passive components ( $R_1, R_2, R_3, C_1$  and  $C_2$ ) with respect to  $\omega_o$  are again analyzed and given as follows:

$$S_{R_1}^{\omega_o} = -\frac{1}{2} \left[ \frac{\alpha_1 \beta_1 \beta_6 R_1 + \alpha_2 \beta_6 R_2 - \alpha_1 \alpha_2 \beta_1 \beta_6 R_1}{\alpha_2 [\alpha_1 \beta_3 \beta_4 R_1 + \beta_6 R_2 - \alpha_1 \beta_1 \beta_6 R_1]} \right] \quad (14)$$

$$S_{R_2}^{\omega_o} = \frac{1}{2} \left[ \frac{\alpha_1 \alpha_2 \beta_1 \beta_6 R_1 - \alpha_1 \alpha_2 \beta_3 \beta_4 R_1}{\alpha_2 [\alpha_1 \beta_3 \beta_4 R_1 + \beta_6 R_2 - \alpha_1 \beta_1 \beta_6 R_1]} \right] \quad (15)$$

$$S_{\alpha_1}^{\omega_o} = \frac{1}{2} \left[ \frac{\alpha_1 \alpha_2 \beta_3 \beta_4 R_1 - \alpha_1 \alpha_2 \beta_1 \beta_6 R_1}{\alpha_2 [\alpha_1 \beta_3 \beta_4 R_1 + \beta_6 R_2 - \alpha_1 \beta_1 \beta_6 R_1]} \right] \quad (16)$$

$$S_{\beta_1}^{\omega_o} = -\frac{1}{2} \left[ \frac{\alpha_1 \alpha_2 \beta_1 \beta_6 R_1}{\alpha_2 [\alpha_1 \beta_3 \beta_4 R_1 + \beta_6 R_2 - \alpha_1 \beta_1 \beta_6 R_1]} \right] \quad (17)$$

$$S_{\beta_3}^{\omega_o} = \frac{1}{2} \left[ \frac{\alpha_1 \alpha_2 \beta_3 \beta_4 R_1}{\alpha_2 [\alpha_1 \beta_3 \beta_4 R_1 + \beta_6 R_2 - \alpha_1 \beta_1 \beta_6 R_1]} \right] \quad (18)$$

$$S_{\beta_4}^{\omega_o} = \frac{1}{2} \left[ \frac{\alpha_1 \alpha_2 \beta_3 \beta_4 R_1}{\alpha_2 [\alpha_1 \beta_3 \beta_4 R_1 + \beta_6 R_2 - \alpha_1 \beta_1 \beta_6 R_1]} \right] \quad (19)$$

$$S_{\beta_6}^{\omega_o} = \frac{1}{2} \left[ \frac{\alpha_2 \beta_6 R_2 - \alpha_1 \alpha_2 \beta_1 \beta_6 R_1}{\alpha_2 [\alpha_1 \beta_3 \beta_4 R_1 + \beta_6 R_2 - \alpha_1 \beta_1 \beta_6 R_1]} \right] \quad (20)$$

$$S_{C_1}^{\omega_o} = S_{C_2}^{\omega_o} = S_{R_3}^{\omega_o} = -S_{\alpha_2}^{\omega_o} = -\frac{1}{2} \quad (21)$$

For unity values of current and voltage transfer gains and equal capacitor and resistor design, it is evident from equations (14) – (21) that active and passive sensitivities of  $\omega_o$  are less than unity in magnitude and hence the circuit exhibits a good sensitivity performance.

### B. Parasitic Study

The influence of DD-DXCCII parasitic on the performance of novel quadrature oscillator is further studied. The various ports of DD-DXCCII are characterized by parasitic resistances ( $R_{Y1}$ ,  $R_{Y2}$ ,  $R_{Y3}$ ,  $R_{X+}$ ,  $R_{X-}$ ,  $R_{Z+}$  and  $R_{Z-}$ ) and parasitic capacitances ( $C_{Y1}$ ,  $C_{Y2}$ ,  $C_{Y3}$ ,  $C_{Z+}$  and  $C_{Z-}$ ) as shown in Fig. 4. From the proposed circuit of versatile quadrature oscillator, it can be seen that two external resistors are connected at X+ and X- terminals. It is to be noted that current conveyors with resistive termination at X port is appropriate with a view to absorb X-terminal parasitic resistances i.e.  $R_{X+}$  and  $R_{X-}$ . It is also worth mentioning that the parasitic resistances and capacitances appearing at the high input impedance terminals ( $Y_1$ ,  $Y_2$  and  $Y_3$ ) and high output impedance terminals ( $Z+$  and  $Z-$ ) are absorbed into the external resistors and capacitors as they are shunt with them. The modified characteristic equation with parasitic effects is given below

$$s^2 + s \left( \frac{1}{C_1 R_1'} + \frac{1}{C_1 R_3'} - \frac{1}{C_1 R_2'} \right) + \frac{1}{C_1 C_1' R_1' R_3'} = 0 \quad (22)$$

The modified frequency of oscillation is given as

$$\omega_o = \sqrt{\frac{1}{C_1 C_1' R_1' R_3'}} \quad (23)$$

where,

$$R_1' = R_1 // R_{Y1} // R_{Y3} // R_{Z-}$$

$$C_1' = C_1 + C_{Y1} + C_{Y3} + C_{Z-}$$

$$R_2' = R_2 + R_{X+}$$

$$R_3' = R_3 + R_{X-}$$

$$C' = C_2 // R' =$$

$$(C_2 + C_{Y2} + C_{Z+}) // (R_{Y2} // R_{Z+})$$

where,  $R_{Y1}$ ,  $R_{Y2}$  and  $R_{Y3}$  are the parasitic resistances and  $C_{Y1}$ ,  $C_{Y2}$  and  $C_{Y3}$  are the parasitic capacitances at the  $Y_1$ ,  $Y_2$  and  $Y_3$  terminals, respectively,  $R_{Z+}$  and  $R_{Z-}$  are the parasitic resistances and  $C_{Z+}$  and  $C_{Z-}$  are the parasitic capacitances at the  $Z+$  and  $Z-$  terminals, respectively, and  $R_{X+}$  and  $R_{X-}$  represent the parasitic resistances appearing at the X+ and X- terminals, respectively.

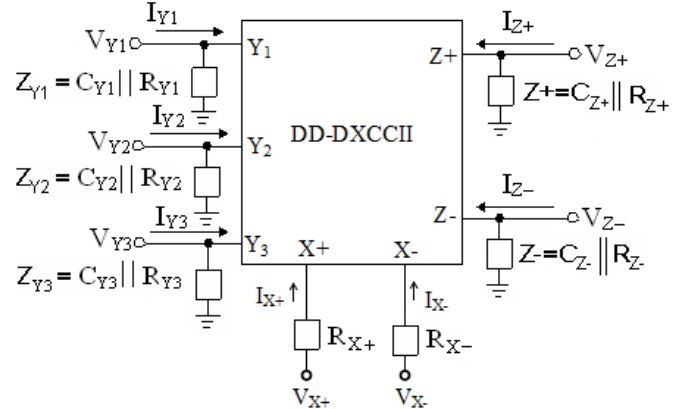


Fig. 4. Parasitic Model of DD-DXCCII

## IV. SIMULATION RESULTS

The performance of the proposed quadrature oscillator is verified using PSPICE with 0.18 $\mu$ m process parameters. The proposed circuit is designed with the frequency of oscillation at 26.54MHz by considering the passive component values as  $C_1 = C_2 = 3\text{pF}$ ,  $R_1 = R_3 = 2\text{k}\Omega$ ,  $R_2 = 1\text{k}\Omega$ . The CMOS implementation of DD-DXCCII as shown in Fig. 1 (b) is used. The list of aspect ratios is shown in Table 2. The supply voltages are taken as  $V_{DD} = -V_{SS} = 1\text{V}$  and the biasing voltage as  $V_{BB} = -0.65\text{V}$ . The simulated FO for the proposed oscillator is found to be 26.18MHz, which is very close to the theoretical value. The two current outputs along with their Fourier spectrum are shown in Fig. 5 and Fig. 6, respectively. Similarly, three voltage outputs and their Fourier spectrum are shown in Fig. 7 and Fig. 8, respectively. The THD for the current and voltage outputs is found to be within 2%, which is low, keeping in view the frequency of operation.

TABLE II:

ASPECT RATIOS (W/L) USED IN Fig. 1 (b)

Transistors	W ( $\mu\text{m}$ ) / L ( $\mu\text{m}$ )
M <sub>1</sub> -M <sub>4</sub> , M <sub>15</sub> -M <sub>20</sub> , M <sub>25</sub> -M <sub>26</sub>	1.44/0.18
M <sub>11</sub> -M <sub>14</sub>	11.51/0.18
M <sub>3</sub> , M <sub>6</sub> -M <sub>10</sub>	2.88/0.18
M <sub>21</sub> -M <sub>24</sub>	0.29/0.18
M <sub>29</sub>	16.19/0.18
M <sub>27</sub> -M <sub>28</sub>	5.22/0.18
M <sub>30</sub>	3.6/0.18

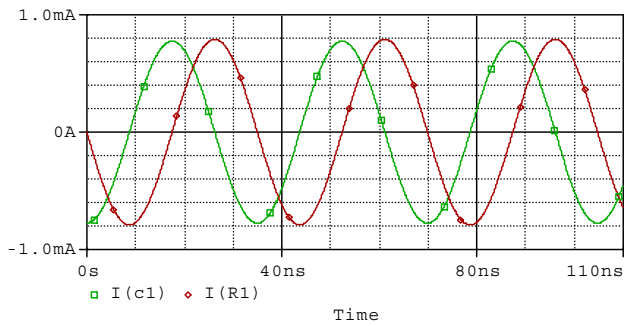


Fig. 5. Two quadrature current outputs at 26.54MHz

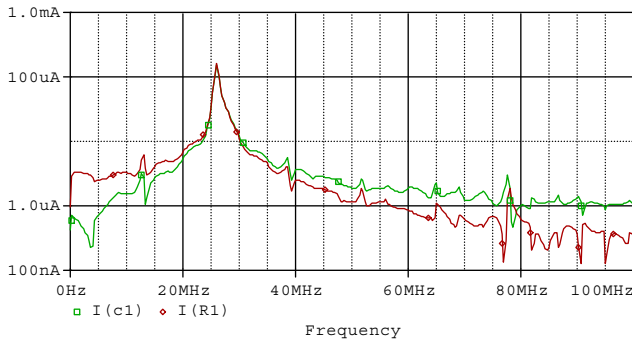


Fig. 6. Fourier spectrum of two current outputs

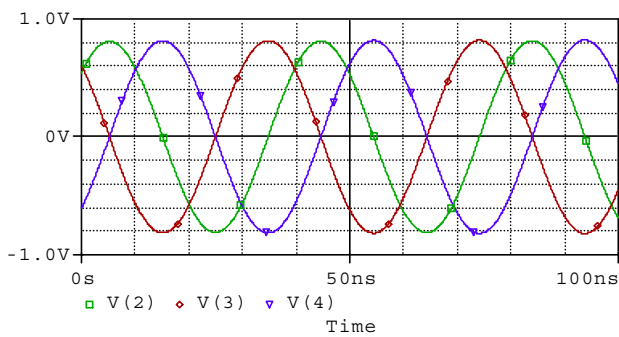


Fig. 7. Three quadrature voltage outputs at 26.54MHz

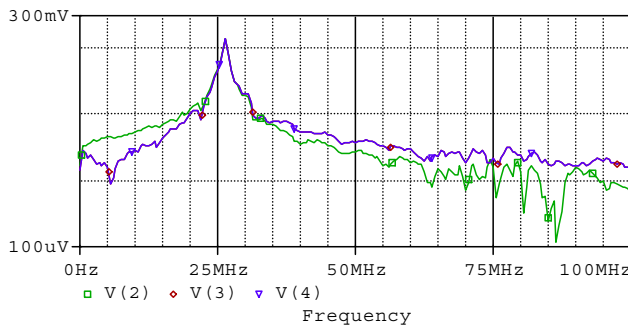


Fig. 8. Fourier spectrum of three voltage outputs

V. PRACTICAL ASPECTS

A. Possible Experimental Setup

The current mode active elements along with DD-DXCCII (at which the new proposed circuit is based on) are not commercially available. The catalogue of such type of

active elements is exhaustive, ranging from CCI, CCII, CCIII, CCCII, DVCC, DDCC, DXCCII etc. However, such active elements have been successfully realized using commercially available integrated circuits (ICs) for instance, LM13600, AD844s [24, 25, 28, 29]. This may apply equally well to DD-DXCCII and its possible realization using commercially available ICs, like LM13600 and AD844s is shown in Fig. 9. It is well known that an AD844 can realize a second generation current conveyor with additional buffered Z output and LM13600 is the standard single-output operational transconductance amplifier (OTA). Moreover, it does provide a possible solution to the need of experimental setups. After verifying the proposed circuit of quadrature oscillator by its CMOS implementation, its verification with OTAs and AD844 realization was also carried out. The supply voltages used were  $\pm 10V$ . The bias current  $I_B$  used is  $500\mu A$ . The circuit was tested with  $C_1 = C_2 = 100pF$ ,  $R_1 = R_3 = 2k\Omega$ ,  $R_2 = 1k\Omega$ . The quadrature voltage and current outputs are shown in Fig. 10 and Fig. 11, respectively. The measured oscillation frequency is 794KHz which is quite near to the designed value of 796.17KHz.

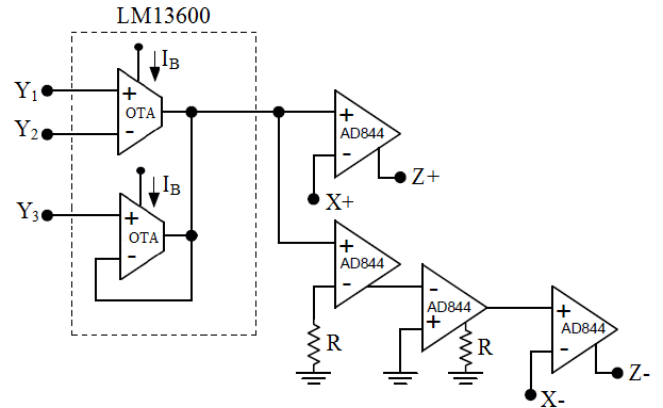


Fig. 9. Possible realization of proposed quadrature oscillator using AD844 and LM13600

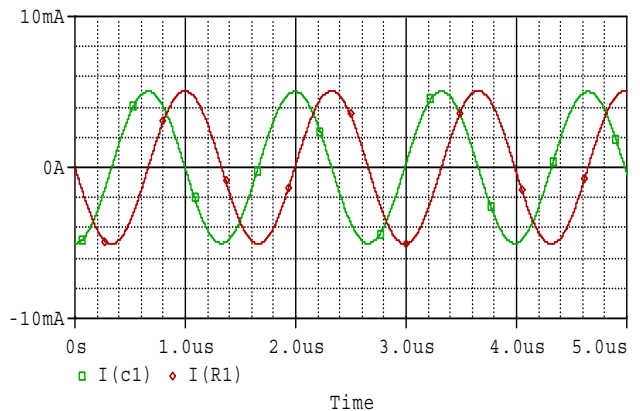


Fig. 10. Two quadrature current outputs at 794KHz

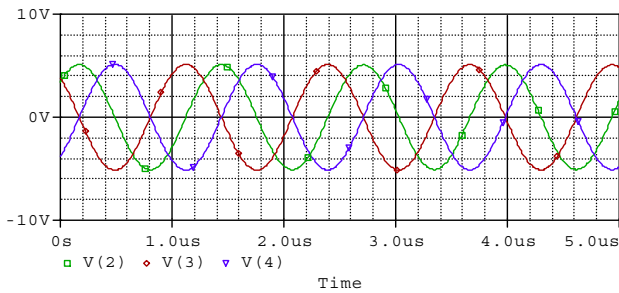


Fig. 11. Three quadrature voltage outputs at 794KHz

### B. Output current sensing

It may further be noted that the output currents are through passive elements. Moreover, the impedance level may also not be desirable and even frequency dependent (where the output is through a capacitor). The purpose may be fulfilled with additional current sensing elements in form of current followers. It is a well known fact that current conveyor itself can be used to realize an accurate current follower. This will lead to high impedance current output but at the cost of ungrounded passive components. All these concerns are quite obvious, but keeping in view the simplicity and other advantages of the proposed circuit, this may not be seen as a drawback of the proposed work. Other available work also suffers from similar current sensing problems [10, 12, 13, 22, 23] as compared to many others which actually show high impedance current output(s) [6, 9, 11, 15-21]. However, the use of current follower would make the passive elements virtually grounded instead of being physically grounded.

## VI. CONCLUSION

In this paper, a new versatile quadrature oscillator is proposed. The proposed circuit is very simple and contains only single DD-DXCCII as active element. It employs all grounded passive components, which is ideal for IC implementation. The proposed circuit provides two quadrature current outputs and three quadrature voltage outputs simultaneously from the same configuration. The proposed circuit enjoys good active and passive sensitivities. However, due to a variety of features along with circuit simplicity, FO and CO is not independently adjustable. Non-ideal and parasitic study is also discussed. Simulations results are further given to confirm the presented theory. Possible experimental setup for DD-DXCCII using commercial available ICs is further discussed.

## REFERENCES

- [1] B. Wilson, "Recent developments in current conveyors and current mode circuits", *IEE Proceeding G*, vol. 137, pp. 61-77, 1990.
- [2] W. Chiu, S. I. Liu, H. W. Tsao, J. J. Chen, "CMOS differential difference current conveyors and their applications", *IEE Proceeding Circuits Devices and Systems*, vol. 143, pp. 91-96, 1996.
- [3] A. M. Soliman, "Simple sinusoidal RC oscillators using current conveyors", *International Journal of Electronics*, vol. 42, pp. 309-311, 1975.
- [4] M. T. Ahmed, I. A. Khan, and N. Minhaj, "On transconductance-C quadrature oscillators", *International Journal of Electronics*, vol. 83, pp. 201-208, 1997.
- [5] I. A. Khan and S. Khwaja, "An integrable gm-c quadrature oscillator", *International Journal of Electronics*, vol. 87, pp. 1353-1357, 2000.
- [6] A. M. Soliman, "Synthesis of grounded capacitor and grounded resistor oscillators", *Journal of Franklin Institute*, vol. 336, pp. 735-746, 1999.
- [7] P. Prommee and K. Dejhan, "An integrable electronic-controlled quadrature sinusoidal oscillator using CMOS operational transconductance amplifier", *International Journal of Electronics*, vol. 89, pp. 365-379, 2002.
- [8] J. Mohan, B. Chaturvedi, and S. Maheshwari, "Grounded components based voltage-mode quadrature oscillators", *International Conference on Multimedia, Signal Processing and Communication Technologies-2013*, pp. 241-245, 2013.
- [9] M. T. Abuelma'atti, H. A. Al-Zaher, "Current-mode sinusoidal oscillators using single FTFN", *IEEE Transactions on Circuits and Systems-II*, vol. 46, pp. 69-74, 1999.
- [10] M. T. Abuelma'atti, "Grounded capacitor current-mode oscillator using single current follower", *IEEE Transactions on Circuits and Systems-I: Fundamental Theory and Applications*, vol. 39, pp. 1018-1020, 1992.
- [11] S. Minaei and O. Cicekoglul, "New current-mode integrator, all-pass section and quadrature oscillator using only active elements", *International Conference on Circuits and Systems for Communications*, vol. 26-28, pp.70-73, 2002.
- [12] M. T. Abuelma'atti, H. A. Al-Zaher, "Current-mode quadrature sinusoidal oscillators using two FTFNs", *Frequenz*, vol. 53, pp. 27-30A, 1999.
- [13] U. Cam, A. Toker, O. Cicekoglul, H. Kuntman, "Current-mode high output impedance sinusoidal oscillator configuration employing single FTFN", *Analog Integrated Circuits and Signal Processing*, vol. 24, pp. 231-238, 2000.
- [14] A. Zeki and A. Toker, "The dual-X current conveyor (DXCCII): a new active device for tunable continuous-time filters", *International Journal of Electronics*, vol. 89, pp. 913-923, 2002.
- [15] I. A. Khan, P. Beg, M. T. Ahmad, "First order current-mode filters and multiphase oscillators using CMOS MOCCIs", *Arabian Journal for Science and Engineering*, vol. 32, pp. 117-126, 2007.
- [16] D. Birolek, A.U. Keskin, V. Biolkova, "Grounded capacitor current mode single resistance-controlled oscillator using single modified current differencing transconductance amplifier", *IET Circuits, Devices and Systems*, vol. 4, pp. 496-502, 2010.
- [17] S. Maheshwari and B. Chaturvedi, "High output impedance CMQO using DVCCs and grounded components", *International Journal of Circuit Theory and Application*, vol. 39, pp. 427-435, 2011.
- [18] S. Maheshwari, I. A. Khan, "Mixed mode quadrature oscillator using translinear conveyors and grounded components", *International Conference on Multimedia Signal Processing and Communication Technologies-2011*, pp. 153-155, 2011.
- [19] J. Mohan, S. Maheshwari and I. A. Khan, "Mixed-mode quadrature oscillators using single FDCCII", *Journal of Active and Passive Electronic Devices*, vol. 2, pp. 227-234, 2007.
- [20] P. Beg, M. S. Ansari, M. A. Siddiqi, "DXCC-II based mixed-mode three phase oscillator", *International Conference on Multimedia Signal Processing and Communication Technologies-2011*, pp. 9-11, 2011.
- [21] D. Birolek, A. Lahiri, W. Jaikla, M. Siripruchyanun, J. Bajer "Realization of electronically tunable voltage-mode/current-mode quadrature sinusoidal oscillator using ZC-CG-CDBA", *Microelectronics Journal*, vol. 42, pp. 1116-1123, 2011.
- [22] B. Chaturvedi, S. Maheshwari, "Second order mixed mode quadrature oscillator using dvccs and grounded components", *International Journal of Computer Applications*, vol. 58, pp. 42-45, 2012.
- [23] S. I. Liu, Y. H. Liao, "Current-mode quadrature sinusoidal oscillator using single FTFN", *International Journal of Electronics*, vol. 81, pp. 171-175, 1996.
- [24] S. Maheshwari, B. Chaturvedi, "High-input low-output impedance all-pass filters using one active element", *IET Circuits, Devices & Systems*, vol. 6, pp. 103-110, 2012.
- [25] S. Maheshwari, "Analogue signal processing applications using a new circuit topology", *IET Circuits, Devices & Systems*, vol. 3, pp. 106-115, 2009.
- [26] S. Yamacli and H. Kuntman, "A new active circuit building block Dual-X Differential Difference Current Conveyor (DXDDCC)", in *Proceedings of the IEEE 12th Signal Processing and Communications Applications Conference Istanbul Tech. Univ., Turkey*, pp. 383-386, 2004.

- [28] P. Beg, "Realization of analog signal processing modules using current conveyors", Department of Electronics Engineering, Aligarh Muslim University, 2013 (Ph.D Thesis).
- [29] S. Maheshwari, M. S. Ansari, "Catalog of Realizations for DXCCII using Commercially Available ICs and Applications", Radioengineering, vol. 21, 2012
- [30] M. Somdunyanok, M. Kumngern, "Commercially available ICs-based DDCC practical implementation", International Conference on Electrical Engineering/ Electronics Computer Telecommunications and Information Technology (ECTI-CON), pp. 402 – 404, 2010.

# Elevator Safety Monitoring and Early Warning System Based on Directional antenna transmission technology

Ying Huang, Weijia Yu

**Abstract**—In order to solve problems of the absence of security protection and the lack of early warning mechanism in the current elevator operation process, elevator safety monitoring and early warning system based on directional antenna transmission technology was proposed. The system includes sensor module circuit, microcontroller module circuit, display module, directional antenna transmission module, remote server and data monitoring system. Design ideas of hardware development, remote server and data monitoring system are introduced. Two version monitoring software are written, one for PC monitor, the other one for mobile phone monitoring. In order to improve data transmission distance, transmission rate and transmission quality, automatic antenna alignment system is designed, which combines the advantages of directional antennas and omnidirectional antennas transmission technique. To overcome problems such as instability of the alignment process, delay and other factors, DMC (Dynamic Matrix Control) algorithm should be used in the system and optimal control of the antenna angular alignment will be achieved. The system can continuously transmit real-time elevator's working status information and environmental information, and it also send commands to notify elevator company managers once an abnormal conditions occur in the elevator, so that people can take urgent measures and maintenance measures. This system can be applied to real-time warning of all-types elevators.

**Index Terms**—wireless sensor technology; safety monitoring; early warning system

*Original Research Paper*  
DOI: 10.7251/ELS1519101H

## I. INTRODUCTION

ELEVATOR has become an indispensable equipment in our daily life, and plays an important role in our life. China has a lot of elevator and maintains a rapid growth rate, but a large number of elevator is running in poor condition [1]. Elevator

accidents caused by lack of maintenance, lack of safe operating condition monitoring and emergency measures which affected the lives and safety of the people happened frequently. Therefore, the design of elevator safety monitoring and early warning system has practical significance [2]. At present, three methods are mainly used for elevator safety monitoring, they are embedded chip, Zigbee technology and GPRS/GSM technology. Embedded chips monitoring via ethernet cabling has disadvantages such as routing complexity, high power consumption, and difficulty to completely realize different information acquisition. Zigbee technology has advantages of low cost, low power consumption and fast data transfer, etc., but only can be applied in short distance communication. GPRS/GSM technology supported by server with slightly higher cost, is widely applied to various practical fields due to prevalence of cell phone signal [3].

In the wireless transmission process, the transmission speed, transmission distance and transmission quality are limited due to installation location and affected by obstacles. In order to improve data transmission distance, transmission rate and transmission quality, directional antenna transmission techniques is adopted in the system.

A directional antenna is an antenna which radiates greater power in one or several specified directions allowing for increased performance on transmit and receive and reduced interference from unwanted sources [4]. Directional antenna has advantages of far communication distance, strong directional anti-interference ability, which can increase the transmission distance and the transfer speed, reduce the signal transmission delay and power consumption of the node, improve the spatial reuse and high spatial multiplexing rate [5-6]. Far communication distance can be achieved by additional gain, and then improve the WSN network throughput, enhanced reliability and reduce latency [7].

Elevator safety monitoring and early warning system based on directional antenna technology could be applied to monitor working state and environmental parameters of elevators. The data acquired from sensors modules are sent to the receiver module via directional antenna, and then data are sent to a remote server by GPRS technology. Monitoring systems process all data and display it[8].

This research reported in the paper is supported by Guangxi university research project (2015), research project of Liuzhou Railway Vocational Technical College (2014), the project of outstanding young teachers' training in higher education institutions of Guangxi.

Ying Huang is with Liuzhou Railway Vocational Technical College, Liuzhou, Guangxi, CHINA (e-mail: 18978225815@163.com).

Weijia Yu was with Liuzhou Railway Vocational Technical College, Liuzhou Railway Vocational Technical College, (corresponding author to provide phone: +86-18978225815; fax: +86-07723698062; e-mail: 76241456@qq.com).

## II. SYSTEM STRUCTURE

Elevator should have not only comfortable environment, but also operate reliably, detect faults quickly as soon as possible and shorten the fault repair time [9-10]. Therefore, it is important to monitor working state and environmental parameters of elevators. These data include voltage, current, acceleration, temperature, humidity, smoke, flames, body sensors and toxic gases, etc. The system is composed of sensor module circuit, microcontroller module circuits, display module, directional antenna module and power module. Software is mainly composed of server systems and data monitoring systems. Various data are collected from Sensor terminal, processed by SCM module circuit and sent to server system by directional antenna module. When server receives a command to read the data, it forwarded the data saved in the database. Data monitoring system processes the data, and notifies elevator company managers once the data is abnormal. The display module is used to display the data collected from Sensor terminal circuit. And the power supply module is provided power to each module. System structure is shown in Figure 1. For easy installation, modular design is adopted in the system, a node is used to detect the elevator working status parameters, another node for detecting elevator environmental parameters. All data are sent by 3G module which embedded TCP / IP protocol stack[11].

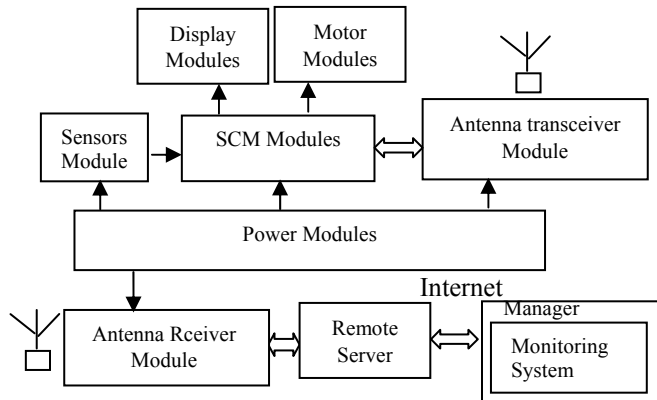


Fig.1. System structure

## III. HARDWARE DESIGN

### A. Data Acquisition Module

Data acquisition is divided into two categories: one is working state of the operating elevator, such as voltage, current, acceleration etc., and another is environmental parameters inside the elevator, such as temperature and humidity, fire, toxic gases, sensors and body sensors. Current detection module uses ACS712 current sensor module. Voltage detector uses a Hall sensor with UART serial transmission interface. Acceleration module uses three-axis accelerometer ADXL345 module. Flame used in infrared detection module. Smoke detector uses a MQ-2 smoke sensor module. Using temperature and humidity sensor DHT11 module. SCM is used STC89C52 processor.

### B. Directional Antenna Module

The nRF905 RF module is chosen as wireless communication module. Its working frequency is 433 ~ 915 MHz. nRF905 RF module has strong anti-interference ability and long transmission distance [6]. Because of distant installation and tall obstacles obstruction, sending node should install gain module to transmit information over longer distances.

### C. Directional Antenna Elevation and Azimuth Calculation

Suppose that  $(x_1, y_1, z_1)$  is geographic coordinates of elevator antenna, and  $(x_2, y_2, z_2)$  is geographic coordinates of server node. They are obtained by GPS module, so the elevation( $\lambda$ ) and azimuth( $\alpha$ ) is calculated by the following formulas[12].

$$\lambda = \arctan \frac{z_2 - z_1}{\sqrt{(y_2 - y_1)^2 + (x_2 - x_1)^2}} \quad (1)$$

$$\alpha = \arctan \frac{y_2 - y_1}{x_2 - x_1} \quad (2)$$

In addition, Seen as the axis of rotation axis of the antenna, as the starting point to the geographic North Pole, so the antenna azimuth is defined as the axis which clockwise rotation to a predetermined angle. The angle rotation. Assumed that the antenna node and the server node antenna coordinates are  $(\lambda_1, \alpha_1)$ 、 $(\lambda_2, \alpha_2)$ , so the azimuth of antenna is calculated by formula (3) [13].

$$\gamma = \arctan \frac{\phi_1 \times \cos \alpha_2}{\phi_2} \quad (3)$$

$$\text{Which } \phi_1 = |\lambda_1 - \lambda_2|, \quad \phi_2 = |\alpha_1 - \alpha_2|^\circ$$

## IV. SOFTWARE DESIGN

### A. Processor Program Design

Server sends the location and height of the elevator which getting from GPS module, by omnidirectional antenna at 360 angle, and then enters data receive mode after receiving the acknowledgment signal of all the nodes of the elevators. Antenna node rotates at a constant speed and stops after receives the position and height sent from server, and then sends a confirmation signal to the server. Elevation and azimuth of the antenna is calculated with the position and height sent from server and its position and height. Antenna alignment is achieved by driving the stepper motor according to elevation and azimuth.

In order to achieve better elevation and azimuth, angle sensor is installed on controller and taken as feedback, and dynamic matrix control algorithm (DMC) is adopted to adjust optimal antenna elevation and azimuth. When power-up, data are collected after the completion of the initialization successfully and antenna alignment is completed. The data including voltage, current, acceleration, temperature, humidity, smoke, flames, body sensors and toxic gases, etc., will be transferred into the appropriate format and then send to receiving module through a directional antenna.

Server receives the data and determines the accuracy of the data format, and then saves it to the database and displays on the screen. The data format is shown as following:

cs1:00;cs2:00;cs3:0.00;cs4:0.00;cs5:000;cs6:0;cs7:0;cs8:0;

The parameters are described in Table I.

Meanwhile, text messages are sent to notify managers as soon as possible when data collected exceeds the set limit.

### B. Antenna Angle Adjustment Algorithm

In order to improve data transmission distance, transmission rate and transmission quality, automatic antenna alignment system is designed, which combines the advantages of directional antennas and omnidirectional antennas transmission

TABLE I  
SCM DATA FORMAT MEANING AND VALUE

Sring	Meaning	Value
cs1	Temperature	Specific values
cs2	Humidity	Specific values
cs3	Voltage	Specific values
cs4	Current	Specific values
cs5	Acceleration	Specific values
cs6	Human Detection	1 or 0
cs7	Smoke	1 or 0
cs8	flames	1 or 0

technique. To overcome the instability of the alignment process, the delay and other factors of system, DMC (Dynamic Matrix Control) algorithm can be used in the system and optimal control of the antenna angular alignment will be achieved.

The angle value of angle sensor output is used as feedback correction parameters, and scroll to optimize the current angle value and the back control amount, and then the expected output angle meets the requirements, adjustment process is shown in Figure 2.

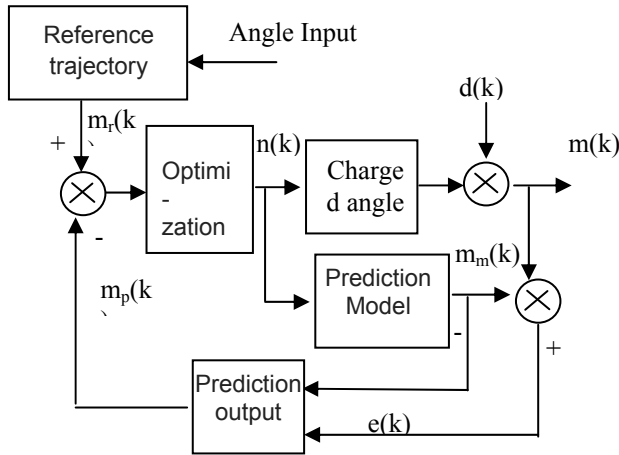


Fig.2. Angle Control Block Diagram

Angle control specific steps as following [14]:

First step: measured angle values of angle sensor, and then discrete sampling data of unit step response is obtained. The discrete sampling data is used as predictive model parameters and combined with the default input control increment, so that angle predicted output values are achieved.

$$\min J(k) = \sum_{i=1}^n q_i [w(k+i) - \hat{y}_M(k+i/k)]^2 + \sum_{j=1}^M r_j \Delta u^2(k+j-1) \quad (4)$$

Second, the control amount of the N sampling periods is determined using optimization criterion, and then output value of next M time was closer to the expected output value, which calculated by the calculation value of the angle.

Third step is data feedback correction. For each acquisition time, the actual angle is collected with angle sensor is corrected by prediction model. This process is continuous cycle, and then the final result is closer to the calculated values.

For the actual system functional requirements, in order to achieve the best output and ensure the accuracy of the antenna alignment, DMC algorithm parameters were repeatedly tested.

### C. PC Monitoring Software Design

Monitoring software is used to achieve lift working conditions and environmental status data, which includes network connectivity, data start and stop functions, data display and curve drawing composition. Monitoring software designed by VB software, connects to remote server using Winsock control and exchanges data via UDP/TCP protocol.

Considering the portability of the system, mobile client monitoring software is also designed to achieve the data based on the Android platform, which sends and receives data through Socket. It is necessary to know the host IP address of the server (IP must be a public address) in order to make sure that the application software communicate properly.

## V. EXPERIMENT RESULTS

After the completion of the system design, each sensor is attached to the specified location inside the elevator car. The data transfer accuracy rate and packet loss rate of 6 sets of samples were tested. Each sensor node periodically sends data to the server, and the data received by the server were stored in the database. PC monitoring software periodically reads data from the server and displays.

Assumed that sensor sends packets every 30 minutes and 10 packets per time, so total of packets is 480 per day. The systems were constantly monitored for 3 days, Therefore, the cumulative total data packet is 1440. The data transfer accuracy rate and packet loss rate of the system is shown in Table II.

TABLE II  
DATA TRANSFER ANALYSIS TABLE

NO.	Send data packets	Received data packets	Data transfer accuracy rate	Packet loss rate
1	1440	1344	93.3%	6.7%
2	1440	1333	92.6%	7.4%
3	1440	1236	85.8%	14.2%
4	1440	1404	97.5%	2.5%
5	1440	1420	98.6%	1.4%
6	1440	978	67.9%	32.1%

As shown in Table II, Data transfer accuracy rate of No.3 and No.6 is 85.8% and 67.9%, and the other's were higher than 90%. Affected by factors of GPRS network, natural environment, antenna interference and transmission loss, etc., the data transfer accuracy rate can not achieve 100% accuracy. Analysis show that the data transfer accuracy rate of No.3 is relatively low just because of Poor mounting position of

directional antenna and imperfect of antenna rotation angle. After calibration, the data transfer accuracy rate of No.3 can reach more than 90%; GPRS network dropped since the telephone charge is overdue, so The data transmission is affected. That is why the data transfer accuracy rate of No.6 is low.

Open the PC monitoring software, PC monitoring software can properly receive and display data, as shown in Table III.

TABLE III  
SENSOR DATA ACQUISITION TABLE

data	time	Humidity /%RH	Temp /°C	Voltage /V	Current /A
2014/6/5	7:42:35	60	31	223.36	74.11
2014/6/5	7:42:51	61	31	223.36	73.88
2014/6/5	7:43:07	61	31	223.36	73.98
2014/6/5	7:43:22	62	31	223.36	74.07
2014/6/5	7:43:38	62	31	223.36	73.98
2014/6/5	7:43:54	63	31	223.36	74.01
2014/6/5	7:44:10	63	31	223.92	74.07
2014/6/5	7:44:25	64	31	223.28	74.05
2014/6/5	7:44:42	64	31	223.36	73.98

data	time	infrared	smoke	flame
2014/6/5	7:42:35	1	0	0
2014/6/5	7:42:51	1	0	0
2014/6/5	7:43:07	1	0	0
2014/6/5	7:43:22	0	0	1
2014/6/5	7:43:38	0	0	0
2014/6/5	7:43:54	1	0	0
2014/6/5	7:44:10	1	0	1
2014/6/5	7:44:25	0	0	0
2014/6/5	7:44:42	1	0	1

In the Table III, when the value of infrared, smoke and flame is 1, a text message is sent to elevator company managers to notify that an abnormal conditions occur in the elevator, infrared value indicates that someone in the elevator, smoke value indicates that there is smoke in the elevator and the flame value indicates that there is flame in the elevator. If the range of voltage, current, temperature and humidity are set, a text message also sent to elevator company managers when the value collected from sensor module exceeds the range.

Data acquisition is consistent with the work of running the elevator data and environmental data. As shown in Table III, data is correct, errors-free, communication smooth and stable.

## VI. CONCLUSION

Monitoring of working state and environmental parameters of elevator can be achieved real-timely by directional antenna

technology. Exception or failure can be responded in time and notification can be sent to manager rapidly. The system can ensure the normal functioning of the elevator to the maximum extent more scientifically and effectively. The system has many advantages such as simple line installation, easy maintenance, scalability, easy construction and so on. Phone-based monitoring method eliminates time and place restrictions and provides more human-based management for staff. The system has practical significance and it can be applied to a variety of elevator monitoring, highlights the social and economic benefits.

## REFERENCES

- [1] Chen Jiayan, Hong Tao, Liu Ganghai, etc.. Research of elevator safety monitoring system based on internet of things technology[J]. Journal of china University of Metrology, 2013, 24(3).
- [2] Zhang Qingpeng, Liu Fangting. The Instruction and Application of ADIASYSTEM[J]. CHINA INSTRUMENTATION, 2009(4):83-86.
- [3] Diao Sha, Chang Xiaoqing, Lu Rong, etc. Elevator Wireless Early Warning System Based on ZigBee[J]. Microcomputer Applications , 2012, 28(12):12-15.
- [4] Xie Yucheng. Study on the deployment of wireless mesh network with directional antennas[D]. Guangxi University, 2013.
- [5] ZHENG Shao-xiong, WANG Wei-xing, SUN Bao-xia, etc.. Humiture monitoring system in paddy field based on directional antenna WSNs[J]. Transducer and Microsystem Technologies, 2014, 33(1):92-96
- [6] ZHENG Shao-xiong . Key technologies on WSN routing based on directional antenna. Electronics World, 2014(1):4-5.
- [7] LUO Hai-yan, ZHENG Shu-li, LI Shao-lin. An improved protocol based on directed diffusion for WSN[J]. JOURNAL OF H EFUI UNIVERSITY OF TECHNOLOGY, 2010, 33(6):851-854.
- [8] Bu Feng, Li Chuanjiang, Li Huan, etc.. Design and implementation of vehicle remote monitoring system based on GPS/GPRS[J]. Computer measurement & control, 2014, 22(1): 79-81.
- [9] YI Xin. Design of elevator online monitoring system based on GPRS[J]. Internet of Things Technologies, 2013, (3):40-41+44.
- [10] LAI Qing-min; HU He-juan. The Remote Call System of Elevator's Various Types of Faults Based on GPRS[J]. Journal of Henan Institute of Education ( Natural Science Edition), 2013, 22(3): 1-4.
- [11] Yang Pan, Zeng Cheng, Wu Pinghui. Network Access Solution of Smart Meter Based on 3G Technology[J]. Computer measurement & control, 2014, 22(1):212-214
- [12] FAN Qiong-jian, GAO Xiang, DING Ji. Research of Stable Tracking System for the Directional Antenna of UAV[J]. Journal of Sichuan Ordnance, 2014, 33(4):84-86
- [13] Wang Di, Liu Fasheng, He Kezhong. Design of Vehicle Directional Antenna Platform Servo System [J]. Design & Application, 2008, (11):77-78.
- [14] Zhang Rinan, Zhang Jiugen, Wei Shaochong. Temperature of air-conditioning control based on dynamic matrix predicative fuzzy pid control algorithm [J]. Computer measurement & control, 2014, 22(4):1073-1075

# Some examples of photorefractive oscillators

Zoran Ljuboje

**Abstract**—The photorefractive effect presents a periodical change of the refractive index of an optical environment under the influence of a coherent light. An interesting phenomenon which occurs at this effect is optical phase conjugation (PC). Photorefractive oscillators, that is photorefractive mirrors present important decides in photorefractive optics and their function is based on photorefractive effect. In these oscillators, a phase-conjugated light beam occurs. The basic characteristics of photorefractive oscillators, such as reflectivity, the existence of the oscillation threshold and the threshold of the coupling strength are explained by the so-called grating-action method. This is analysed on a ring oscillator, semilinear mirror and linear mirror.

**Index terms**—fotorefractive oscillators, grating-action method, ring oscillator, semilinear mirror, linear mirror.

Original Research Paper

DOI: 10.7251/ELS1519105L

## I. INTRODUCTION

THE paper will analyse photorefractive oscillators [1] whose operation is based on the photorefractive effect.

The photorefractive effect is based on the four-wave mixing of laser light beams (4TM) in some crystals [2]. In this effect, a periodical change of refraction index of an optic environment occurs under the activity of light. During the illumination of some crystals by coherent light, carriers of free charge are created by the transfer of the donor atom electrons to the conduction zone. The number of electron transfers is proportional to the number of donor atoms and the light intensity. Carriers diffuse to the place with lower light intensity, and the opposite sign charges remain in their positions, so-called holes. As the consequence of this rearrangement of charge, an internal electric field occurs, i.e. the phenomenon of change in local refraction index occurs, that is, a diffraction grating is formed in the crystal at which additional incident beams can be scattered (Figure 1).

An interesting effect which causes light in a photorefractive environment is optical phase conjugation (PC). In this situation a simultaneous rotation of the phase and the direction of the light beam wave propagation. So, the crystal is illuminated with three laser beams: two oppositely directed pumps whose amplitudes are  $A_1$  and  $A_2$  and an amplitude signal  $A_4$ . As the result, the fourth wave occurs, with the amplitude  $A_3$  which presents a phase-conjugated copy of the beam  $A_4$ . Unlike the known law of reflection of light in geometrical optics, the reflected beam  $A_3$  returns by the same path of the incident beam  $A_4$ . A PC beam is interesting because of great opportunities for its practical application.

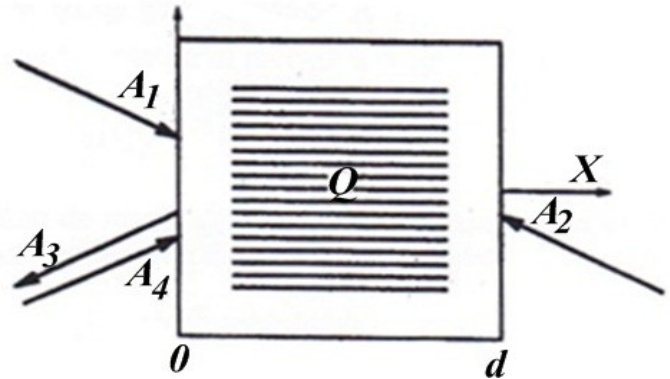


Fig. 1. Four-wave mixing in photorefractive crystals.

The basic equations which describe the process are [3]:

$$\frac{dA_1}{dx} = QA_4 - \alpha A_1, \quad \frac{dA_4^*}{dx} = -QA_1^* - \alpha A_4^*, \quad (1)$$

$$\frac{dA_2^*}{dx} = -QA_3^* + \alpha A_2^*, \quad \frac{dA_3}{dx} = QA_2 + \alpha A_3. \quad (2)$$

In the named equations,  $A$  denotes the amplitudes of waves,  $\alpha$  is the absorption coefficient,  $Q$  presents the so-called amplitude of the transmission diffraction grating, and the “asterisk” denotes the conjugated-complex units. The amplitude of the transmission diffraction grating satisfies the following equation:

Manuscript received 1 September 2015. Received in revised form 1 December 2015.

Zoran Ljuboje is with the Faculty of Electrical Engineering, University of East Sarajevo, Bosnia and Herzegovina  
e-mail: zoran.ljuboje@etf.unssa.rs.ba).

$$\tau \frac{dQ}{dt} + \varepsilon Q = \frac{\gamma}{I} (A_1 A_4^* + A_2^* A_3), \quad (3)$$

where  $\tau$  is the relaxation time,  $I$  is the total intensity of waves  $I = \sum |A_i|^2$ , while  $\varepsilon$  and  $\gamma$  are the parameters which depend on the electric fields formed in the crystal [4]. The solving of these equations is performed numerically and may lead to numerical instabilities, but that is not going to be discussed in this paper [5], [6].

## II. PHOTOREFRACTIVE OSCILLATORS

The most important devices in photorefractive optics are photorefractive oscillators, that is, mirrors. Their operation is based on the photorefractive effect. Photorefractive oscillators are formed when photorefractive crystals are illuminated with one or two laser beams. In that, a diffraction grating is formed in the crystal, on which the diffraction of laser beams occurs. The most interesting ones are the configurations of oscillators which create the phase-conjugated beams of incident signals. Photorefractive oscillators with one incident beam are: linear, semilinear, ring and “cat” oscillators. A *Cat* oscillator has two internal interference regions, and each of the other oscillators has one. In the others, external mirrors are used, and *cat* oscillators use internal total reflection.

Photorefractive oscillators with two incident beams are: double PC mirror, mutually incoherent beam-coupler, and the so-called *bird* and *frog* oscillators.

In this paper, the oscillators with one incident beam will be analyzed: ring, semilinear and linear photorefractive oscillator.

An oscillator operation analysis can be explained efficiently by the grating-action method [7]. On the basis of this method, the relations of laser beam connections at the entrance ( $0$ ) and exit of a crystal ( $d$ ) are given by the expressions:

$$\begin{bmatrix} A_{1d} \\ A_{4d} \end{bmatrix} = \tau(u) \begin{bmatrix} A_{10} \\ A_{40} \end{bmatrix}, \quad \begin{bmatrix} A_{30} \\ A_{20} \end{bmatrix} = \tau(u) \begin{bmatrix} A_{3d} \\ A_{2d} \end{bmatrix}, \quad (4)$$

where the matrix  $\tau(u)$ :

$$\tau(u) = \begin{bmatrix} \cos u & -\sin u \\ \sin u & \cos u \end{bmatrix} \quad (5)$$

where  $u$  is the total grating action and calculated from the expression:

$$\tan u = \frac{A_{10} A_{40}^* + A_{2d}^* A_{3d}}{aI \coth(ayd/2) + I_{40} - I_{3d} + I_{2d} - I_{10}}, \quad (6)$$

where  $a$  is the constant calculated from boundary conditions,  $\gamma$  is the coupling strength of the crystal,  $d$  is the thickness of the crystal, and  $I$  denotes the intensities of light beams. On the basis of this method, it is possible to construct an adequate photorefractive circuit which, in a general case, corresponds to the 4TM process (Figure 2).

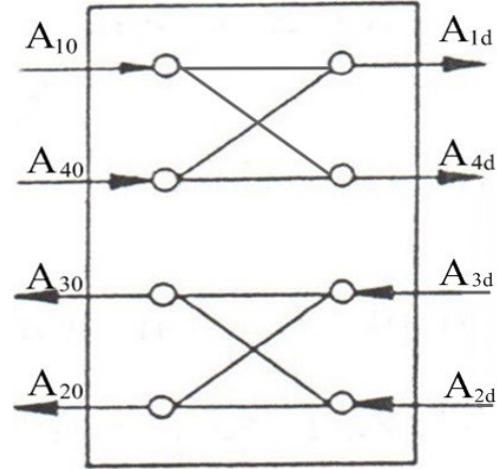


Fig. 2. Optical processor representation of the 4TM process.

## III. RING OSCILLATOR

A ring oscillator has the possibility of self-starting at the oscillation threshold. This oscillator has two ordinary mirrors outside the crystal and one interaction region in the crystal (Figure 3.)

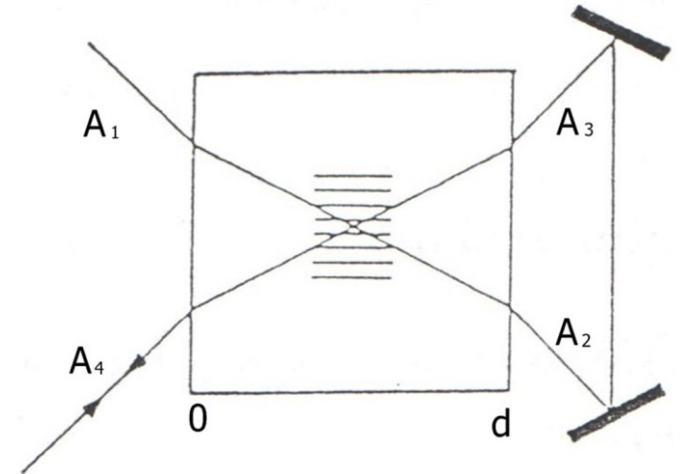


Fig. 3. Photorefractive ring mirror.

The analysis of operation of this oscillator can be efficiently explained by the mentioned grating-action method. Figure 4 shows an adequate photorefractive circuit of this oscillator. By applying the expressions (4) and (5), for a ring oscillator is  $A_{10} = 0$  so it follows that the test signal  $P = A_{40}$ , among the others, generates the output signal  $S = A_{30}$ , i.e.

$$A_{30} = -\sqrt{M} A_{40} \sin 2u, \quad (7)$$

where  $M$  is the product of reflectivity of external ordinary mirrors.

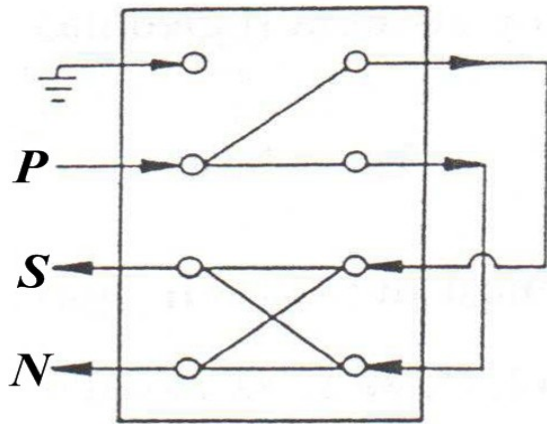


Fig. 4. Photorefractive circuits related to the ring mirror.

The reflectivity of beam in this oscillator is given by the expression  $R = I_{30} / I_{40} = A_{30}^2 / A_{40}^2$ , so, from (7) it follows:

$$R = M \sin^2 2u, \quad (8)$$

while the action  $u$  is calculated from (6) and given by the expression:

$$\cos^2 u = \frac{M - 1 - (1 + M)a \coth(a\gamma d / 2)}{4M} \quad (9)$$

Figure 5 presents the solutions which follow from (8) and (9), defining the dependence of the oscillator reflection in the function of the coupling parameter, where  $M$  is given as a parameter, and  $d = 1$ .

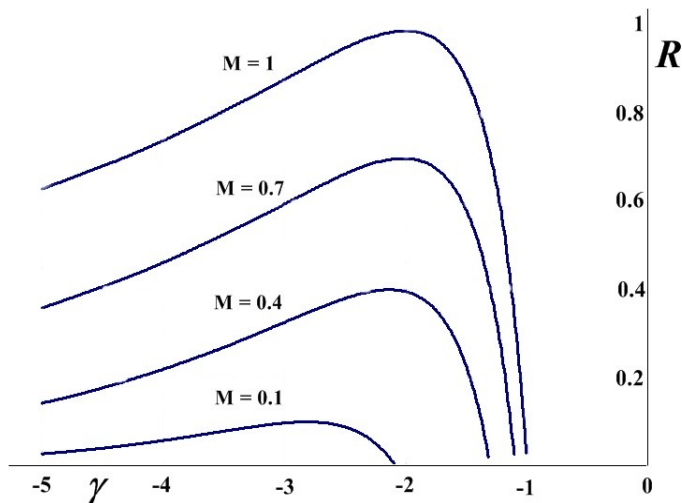


Fig. 5. Oscillator reflection in the function of coupling constant.

Threshold of the coupling strength  $\gamma_{th}$  is calculated from (9) (for  $u \rightarrow 0$ ) and from that it follows:

$$\tanh(a\gamma_{th}d / 2) = \frac{M - 1}{3M + 1}, \quad (10)$$

what is equivalent to the results in [8] but obtained in a simpler way. It is obvious that the coupling threshold has the value  $\gamma_{th}d \rightarrow -1$ , when  $M \rightarrow 1$  (Figure 6).

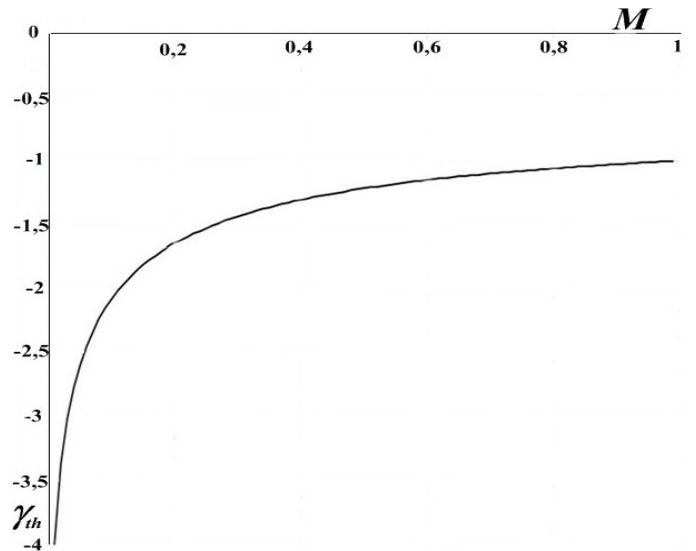


Fig. 6. Threshold of the coupling strength in the function of reflectivity  $M$ .

At the oscillation threshold, it is  $a = (1 - M) / (1 + M)$  and from that, on the basis of (10) it follows that the relation between the threshold of the coupling strength and the parameter  $a$  given by the expression;

$$\gamma_{th}d = \frac{1}{a} \ln(1 - a), \quad (11)$$

what is presented in Figure 7 (for  $d = 1$ ).

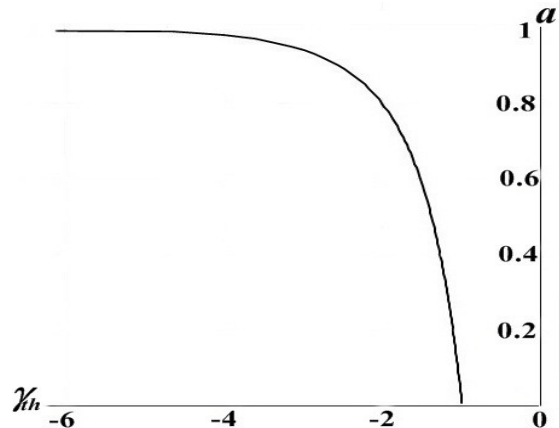


Fig. 7. Constant  $a$  in the function of the threshold of the coupling strength.

Ring oscillators can have an interesting application. For example, two couples ring oscillators whose operation is based on 4TM present a combination which is analogous to an electronic flip-flop circuit [9], [10]. Such a flip-flop oscillator consists of two ring oscillators which are from the outside pumped by the light intensities which may be different. In that, only one oscillator oscillates and the other shuts down and vice versa.

IV. SEMILINEAR MIRROR

Semilinear mirror is, also, an oscillator with one incident light beam and one interaction region. It has one external mirror and does not have the possibility of self-restarting (Figure 8 and Figure 9).

We will repeat the procedures as in the previous case [11]. The incident signal  $P = A_{40}$  generates the beams and on the basis of (4) and (5) we get the beams at the exit:

$$A_{1d} = -A_{40} \sin u, \quad A_{4d} = A_{40} \cos u, \quad (12)$$

and, in that,  $A_{10} = 0$ .

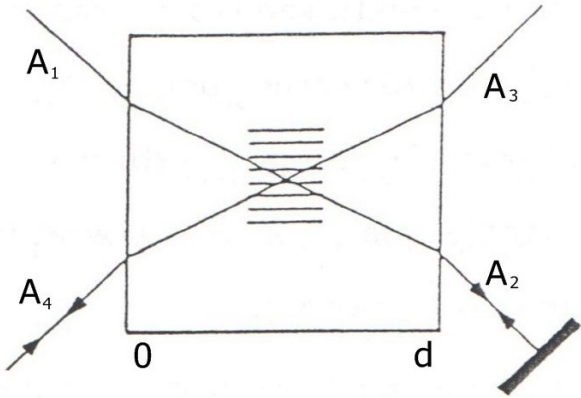


Fig. 8. Photorefractive semilinear mirror.

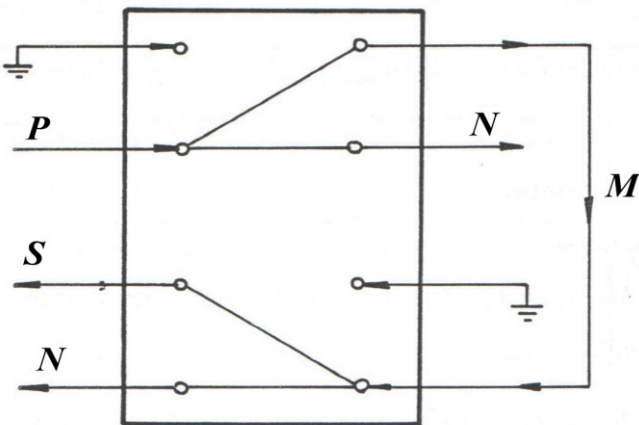


Figure 9. Photorefractive circuits related to the semilinear mirror.

The beam  $A_{1d}$  via the external mirror with reflection coefficient  $M$  presents the entrance  $A_{2d} = \sqrt{M} A_{1d}$ , while  $A_{3d} = 0$ . By applying the relations (4) and (5) it follows:

$$A_{30} = -\sqrt{M} A_{1d} \sin u, \quad A_{20} = -\sqrt{M} A_{1d} \cos u, \quad (13)$$

The constant  $a$  is calculated from the expression  $a = \sqrt{T_d} / I_d$ , where  $T_d = 4I_{1d}I_{4d} + (I_{1d} + I_{2d} - I_{4d})^2$ ,  $I_{1d}$ ,  $I_{2d}$  are  $I_{4d}$  light beam intensities for  $z = d$  and  $I_d$  is their sum. On the basis of the calculation for the constant  $a$ , and also from (12) and (13) for the reflection of this mirror  $R = I_{30} / I_{40}$  it is obtained:

$$R = \left( \frac{\sqrt{M}(1+a^2) + 2[a^2(M+1)-1]^{1/2}}{M(1-a^2)+4} \right)^2. \quad (14)$$

By the arranging from the expression (6) for this case, it follows:

$$\gamma d = \frac{1}{a} \ln \frac{1-a}{1+a}. \quad (15)$$

On the basis of (14) and (15) in Figure 10 the dependence  $R = f(\gamma)$  is presented, where  $M$  is the parameter, and  $d = 1$ .

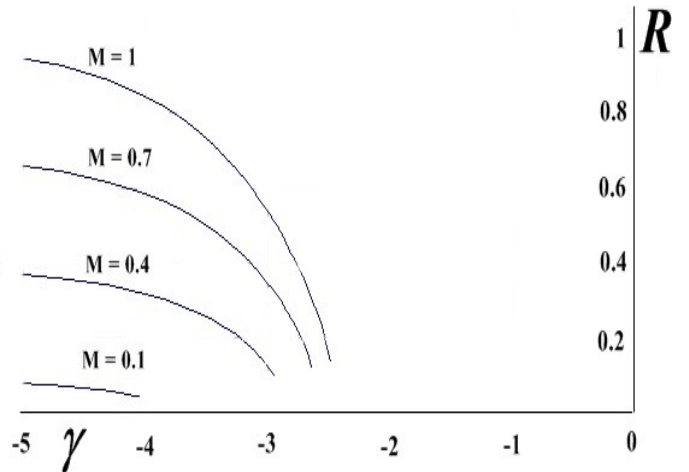


Fig. 10. Oscillator reflection in the function of the coupling constant.

Minimal reflectivity value follows from the equation (14) for the value of the constant  $a$ :

$$a^2 = \frac{1}{M+1}. \quad (16)$$

The threshold of the coupling strength follows from (15) and (16):

$$\gamma_{th}d = \sqrt{1+M} \ln \left( \frac{\sqrt{1+M} - 1}{\sqrt{1+M} + 1} \right). \quad (17)$$

This result is identical to the result from the paper [8] where it has been obtained in a completely different, but a more complicated way. For the case of maximal reflexivity  $M \rightarrow 1$ ,  $\gamma_{th} \rightarrow -2.49$ . (Figure 11)

Also, the solutions given in Figure 12 follow from the expression (15).

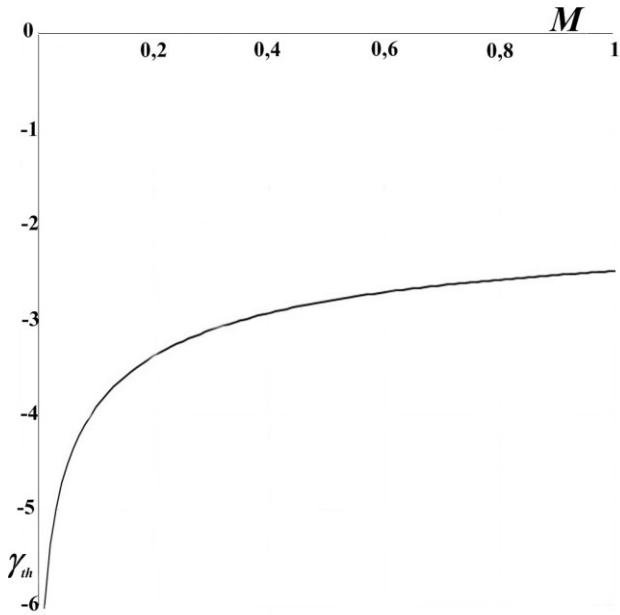


Fig. 11. Threshold of the coupling strength in the function of reflexivity  $M$ .

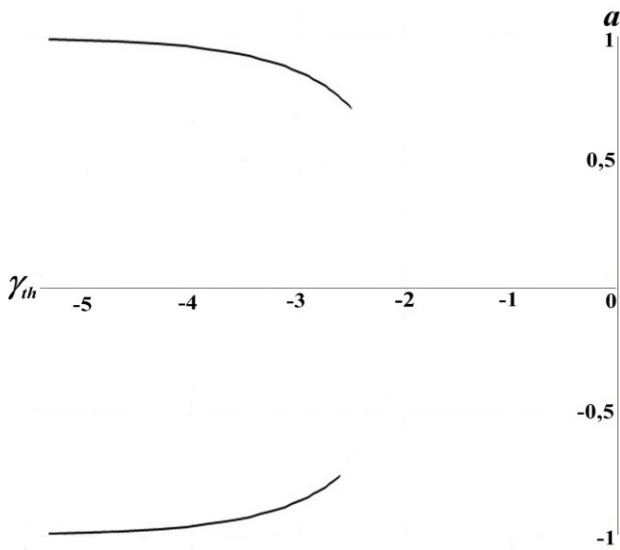


Fig. 12. Constant  $a$  in the function of the threshold of the coupling strength.

V. LINEAR MIRROR

We will mention the linear mirror, too. This oscillator is, also, a mirror with one incident beam, one interaction region and has the possibility of self-starting at the threshold. This mirror also has two ordinary external mirrors (Figure 13).

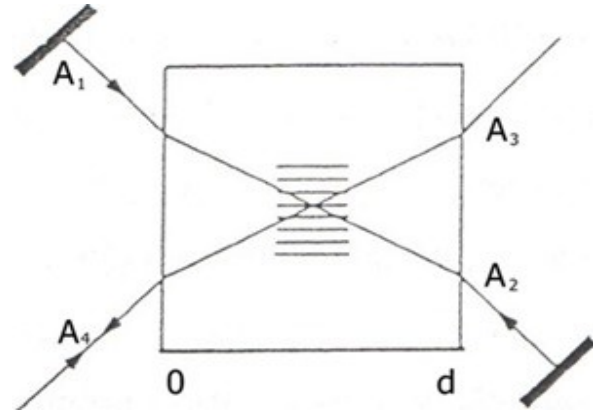


Fig. 13. Photorefractive linear mirror.

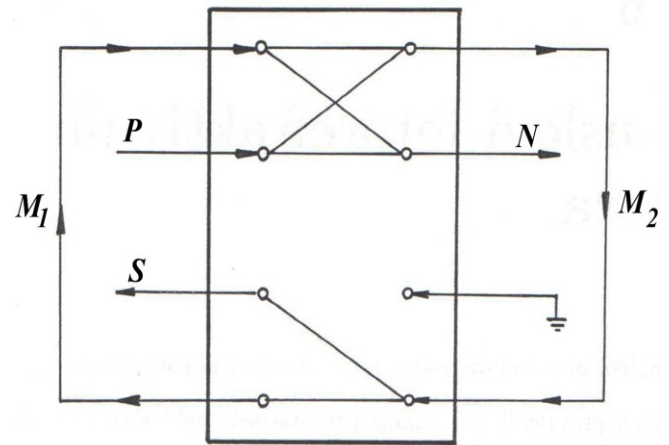


Fig. 14. Photorefractive circuits in relation to the linear mirror.

We will repeat the same procedures as for the previous examples. The incident signal  $P = A_{40}$  and beam  $A_{10}$  generate the beams at the exit. The beam  $A_{1d}$  via the external reflection coefficient  $M_2$  presents the entrance  $A_{2d} = \sqrt{M_2} A_{1d}$ , while  $A_{3d} = 0$ . From (4) and (5) among the other, it follows:

$$A_{30} = -\sqrt{M_2} A_{1d} \sin u, \quad A_{20} = \sqrt{M_2} A_{1d} \cos u \quad (18)$$

The beam  $A_{20}$  returns via the external mirror of reflection  $M_1$ , i.e.  $A_{10} = \sqrt{M_1} A_{20}$  and thus the process is repeated.

It follows from the calculation that the minimal value of the threshold of coupling is:

$$\gamma_{th}d = \ln \sqrt{M_1 M_2} \quad (19)$$

It is obvious that the threshold of the coupling strength tends to zero  $\gamma_{th}d \rightarrow 0$ , when  $M_1 M_2 \rightarrow 1$ .

For the case when the reflectivities  $M_1 = M_2$  it follows from (19) that

$$\gamma_{th}d = \ln M, \quad (20)$$

and that is presented in Figure 15.

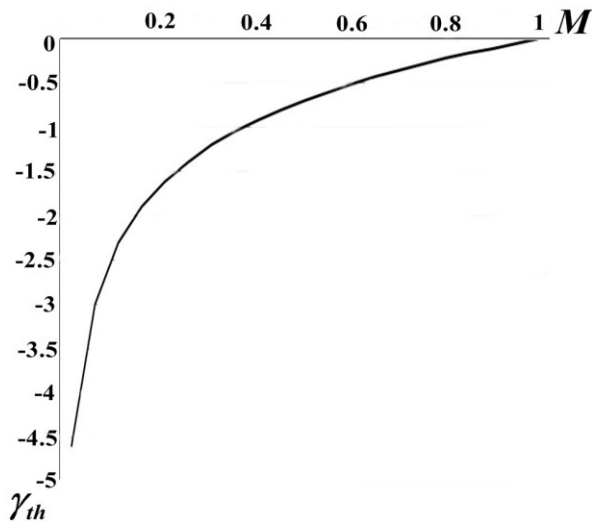


Fig.15. Threshold of coupling strength in the function of reflectivity  $M$ .

## VI. CONCLUSION

The paper analyses the examples of photorefractive oscillators with one incident beam. The operation of this oscillators is based on the photorefractive effect, and in that a phase-conjugated light beam also appears, so they are also called phase conjugated mirrors. So-called grating-action method has been applied, by means of which are efficiently explained the reflectivity of oscillator, then the so-called oscillation threshold and the threshold of coupling strength. This is analysed on a ring oscillator, semilinear and linear mirror. Analytical calculations have been performed and characteristic units, such as reflectivity and characteristic units at the oscillation threshold have been presented graphically.

## REFERENCES

- [1] Z. Ljuboje "Fotorefraktivni oscilatori sa jednim upadnim zrakom", INFOTEH-JAHORINA, Vol. 14, March 2015.
- [2] P. Gunter and J.P. Huignard (eds), *Photorefractive Materials and Their Applications*, I and II (Springer, Berlin, 1988, 1989)
- [3] W. Krolikowski, K. D. Shaw, M. Cronin-Golomb and A. Bledowski, *J. Opt.Soc.Am.B* 6 (1989); W. Krolikowski, M.R. Belić, M. Cronin-Golomb and A. Bledowski, *J. Opt.Soc.Am.B* 7 (1990).
- [4] N. V. Kukhtarev, V. Markov and S. Odulov, "Transient energy transfer during hologram formation in LiNbO3 in external electric field", *Opt. Commun.* 23 338 (1977).
- [5] M. Belić and Z. Ljuboje, "Chaos in phase conjugation: physical vs numerical instabilities", *Opt. Quant. Electron.* 24 745 (1992)
- [6] Z. Ljuboje, O. Bjelica "Numeričke nestabilnosti pri rješavanju nekih problema u fizici", INFOTEH-JAHORINA, Vol. 13, March 2014.
- [7] M. S. Petrović, M. R. Belić, and F. Kaiser, "Photorefractive circuitry and optical transistors", *Opt. Commun.* 121 (1995).
- [8] M. C. Golomb, B. Fischer, J.O. White and A. Yariv, "Theori and application of four-wave mixing in photorefractive media" *IEEE J. Qant. Electron.* QE-20, 12 (1984).
- [9] M. Petrovic, M.R. Belic, M.V. Jaric and F. Kaiser, "Optical photorefractive flip-flop oscilator", *Opt. Commun.* 138, 349 (1997)
- [10] Z. Ljuboje, M. Petrović, "Optički fotorefraktivni flip-flop oscilator" INFOTEH-JAHORINA, Vol. 3, March 2003.
- [11] Z. Ljuboje, "Numerički haos u fotorefraktivnoj optici". neobjavljeno.

# Instruction for Authors

## *Editorial objectives*

In the journal "Electronics", the scientific papers from different fields of electronics and electrical engineering in the broadest sense are published. Main topics are electronics, automatics, telecommunications, computer techniques, power engineering, nuclear and medical electronics, analysis and synthesis of electronic circuits and systems, new technologies and materials in electronics etc. The main emphasis of papers should be on methods and new techniques, or the application of existing techniques in a novel way.

## *The reviewing process*

Each manuscript submitted is subjected to the following review procedures:

- It is reviewed by the editor for general suitability for this publication;
- If it is judged suitable, two reviewers are selected and a double-blind review process takes place;
- Based on the recommendations of the reviewers, the editor then decides whether the particular paper should be accepted as it is, revised or rejected.

## *Submissions Process*

The manuscripts are to be delivered to the editor by e-mail: [electronics@etfbl.net](mailto:electronics@etfbl.net).

Manuscripts have to be prepared in accordance with the instructions given in the template for paper preparation that can be found on the journal's web page ([www.electronics.etfbl.net](http://www.electronics.etfbl.net)).

**Authors should note that proofs are not supplied prior to publication and ensure that the paper submitted is complete and in its final form.**

## *Copyright*

Articles submitted to the journal should be original contributions and should not be under consideration for any other publication at the same time. Authors submitting articles for publication warrant that the work is not an infringement of any existing copyright and will indemnify the publisher against any breach of such warranty. For ease of dissemination and to ensure proper policing of use, papers and contributions become the legal copyright of the publisher unless otherwise agreed.

# ELECTRONICS, VOL. 19, NO. 2, DECEMBER 2015

---

## PAPERS

NONPARABOLIC EFFECTS IN MULTIPLE QUANTUM WELL STRUCTURES AND INFLUENCE OF EXTERNAL MAGNETIC FIELD ON DIPOLE MATRIX ELEMENTS.....	39
Aleksandar Demeć, Jelena Radovanović and Vitomir Milanović	
DESIGN OF A 1 DOF MEMS MOTION STAGE FOR A PARALLEL PLANE GEOMETRY RHEOMETER.....	45
Yong-Sik Kim, Nicholas G. Dagalakis, Chiara Ferraris, and Svetlana Avramov-Zamurovic	
MEMS MIRRORS USING SUB-WAVELENGTH HIGH-CONTRAST-GRATINGS WITH ASYMMETRIC UNIT CELLS.....	52
Milan Maksimović	
JOINT EFFECT OF HETEROGENEOUS INTRINSIC NOISE SOURCES ON INSTABILITY OF MEMS RESONATORS.....	59
Olga Jakšić, Ivana Jokić, Miloš Frantlović, Danijela Randjelović, Dragan Tanasković, Žarko Lazić and Dana Vasiljević-Radović	
PROTOTYPE OF THE MULTICHANNEL ACQUISITION SYSTEM DEVELOPED FOR ICTM PRESSURE TRANSMITTERS.....	66
P. Poljak, B. Vukelić, M. Vorkapić and D.V. Randjelović	
ANALYTICAL MODELLING OF THE TRANSIENT RESPONSE OF THERMOPILE-BASED MEMS SENSORS.....	70
D.V. Randjelović, A.G. Kozlov, O.M. Jakšić, M.M. Smiljanić and P.D. Poljak	
POSITION MEASUREMENT OVER WIDE RANGE BY SIMULTANEOUS USE OF LOW AND HIGH COHERENCE LIGHT SOURCE.....	74
Miloš C. Tomić and Zoran V. Đinović	
IMPROVING THE METHODOLOGY OF MAIN POWER EQUIPMENT CHOICE FOR THE GAS TURBINE PLANTS.....	80
Evgeny Lisin, Wadim Strielkowski, Ivan Komarov, Ivan Garanin	
APPLICATION AND CONTROL METHOD OF ELECTROMAGNETIC SYNCHRONIZER FOR DOUBLE ROTOR MOTOR POWER COUPLING SYSTEM.....	88
Jiang Kejun, He Ren, and Zhang Lanchun	
SINGLE DD-DXCII BASED QUADRATURE OSCILLATOR WITH SIMULTANEOUS CURRENT AND VOLTAGE OUTPUTS.....	94
B. Chaturvedi and J. Mohan	
ELEVATOR SAFETY MONITORING AND EARLY WARNING SYSTEM BASED ON DIRECTIONAL ANTENNA TRANSMISSION TECHNOLOGY.....	101
Ying Huang, Weijia Yu	
SOME EXAMPLES OF PHOTOREFRACTIVE OSCILLATORS.....	105
Zoran Ljuboje	

---

ISSN 1450-5843

UDK 621.38